Surface Passivation for Silicon Heterojunction Solar Cells

Deligiannis, Dimitris

Important note
To cite this publication, please use the final published version (if applicable).
Please check the document version above.

Surface Passivation for Silicon Heterojunction Solar Cells

Dimitrios Deligiannis

Surface Passivation for Silicon Heterojunction Solar Cells

Proefschrift

ter verkrijging van de graad van doctor aan de
Technische Universiteit Delft, op gezag van de
Rector Magnificus prof. ir. K. C. A. M. Luyben,
voorzitter van het College voor Promoties,
in het openbaar te verdedigen op
vrijdag 8 september 2017 om 15:00 uur

door

Dimitrios DELIGIANNIS

Master of Science in Sustainable Energy Technology,
Technische Universiteit Delft, Nederland
geboren te Athene, Griekenland

This dissertation has been approved by the
promotor: Prof. dr. M. Zeman
copromotor: Dr. R. A. C. M. M. van Swaaij

Composition of the doctoral committee:

Rector Magnificus	chairperson
Prof. dr. M. Zeman	Technische Universiteit Delft
Dr. R. A. C. M. M. van Swaaij	Technische Universiteit Delft

Independent members:

Prof. dr. A. W. Weeber	Technische Universiteit Delft and ECN
Prof. dr. I. M. Richardson	Technische Universiteit Delft
Prof. dr. ir. M. C. M. van de Sanden	Technische Universiteit Eindhoven and DIFFER
Dr. M. Creatore	Technische Universiteit Eindhoven
Dr. K. Ding	Forschungszentrum Jülich

A digital copy of this thesis is available at https://repository.tudelft.nl

To my grandparents and parents

Contents

1
Introduction

One of the most promising solar-cell technologies for photovoltaic energy conversion is based on silicon heterojunctions (SHJ), combining the advantages of crystalline and thin-film silicon technologies, and leading to high efficiencies at a reduced cost. This thesis discusses certain aspects of SHJ solar cells and has a main focus on the surface passivation of the crystalline silicon wafer. In the introduction, first a historical background and the motivation behind the development of solar cell technologies is presented. This is followed by a detailed discussion of the solar cell operation. Afterwards the SHJ solar cell is introduced and the key points in the device performance are analyzed. Finally, the outline of this thesis and the contribution to the field of SHJ solar cells are described.

1.1 Historical background

Silicon is the eighth most abundant chemical element in the solar system [1] and the second most abundant in the earth's upper continental crust after oxygen [2]. In the form of silicon dioxide (SiO_2) it was already used in ancient times to make sharp flints, which were some of the first tools used by humans. Although it existed for many years in chemical compounds, it was only in 1824 that pure silicon was obtained by Jöns Jakob Berzelius. After this discovery, surprisingly it took more than one hundred years for the scientific community to focus on silicon. Figure 1.1 shows the documents published per year that include the word silicon, as obtained from the Scopus database. It clearly shows that silicon started to draw a lot of attention after the 1949, a year that signifies the beginning of the semiconductor era with the invention of transistor [3]. Since 1949 there was a rapid increase in the documents published per year, with only a slight decrease over the last five years. Among other applications, silicon is now mainly used in electronics and especially in photovoltaic devices.
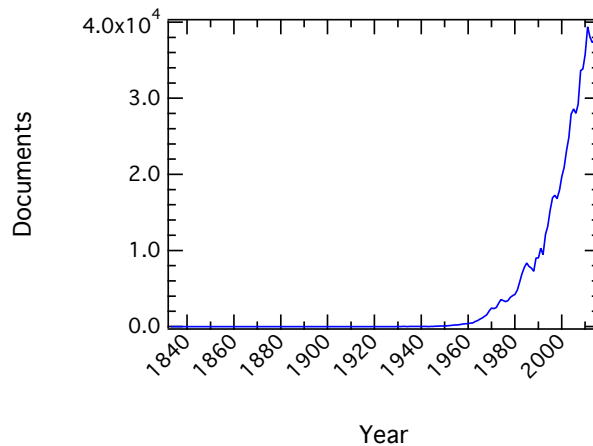
Figure 1.1: Number of documents published per year that contain the keyword "silicon" as obtained from Scopus database.

The photovoltaic effect was observed for the first time in 1839 by Becquerel [4], who measured an electric current by exposing silver electrodes placed in an electrolyte to illumination. The effect was further described by Adams and Day [5] in 1877, who illuminated selenium electrodes and managed to obtain a photogenerated electric current. The first "thin film"

photovoltaic devices came a few years later with the work of Fritts [6]. These devices consisted of compressed selenium between a metal (e.g. brass) and a gold leaf and had an area of $30\,cm^2$. In the next years there was some efficiency improvement in the selenium devices [7], while copper-cuprous oxide photovoltaic cells [8] and thallous-sulphide cells were developed [9]. The next big step came after the invention of transistors [3] and the description of the p-n junction [10] in the years 1947–1949 by Bardeen, Brattain, and Shockley.

In 1954 the first crystalline silicon (c-Si) based solar cell was developed at Bell Laboratories in the USA by Chapin et al. [11]. This solar cell had an efficiency of 6 %, which was significant at the time. In those years research on photovoltaics was focused on c-Si. Although amorphous silicon was known, it was prepared by evaporation or sputtering and was characterized by a high density of states in the band gap. Moreover, it was not known that doping is possible and therefore it was considered not to be suitable for electronic applications. The breakthrough came in 1969, when Chittick et al. [12] used the radio-frequency glow discharge technique to deposit hydrogenated amorphous silicon films (a-Si:H) from silane gas (SiH_4). The doping of a-Si:H was investigated by Spear and LeComber [13], who demonstrated that a-Si:H could be doped both n- and p-type by adding phosphine (PH_3) and diborane (B_2H_6) to the SiH_4 pre-cursor gas, respectively. After it became known that a-Si:H could be doped, the first a-Si:H solar cell was fabricated in 1976 by Carlson and Wronski with an efficiency of 2.4 % [14].

Interestingly, the combination of a-Si:H and c-Si for photovoltaic application was already studied by Fuhs et al. in 1974 [15], before the fabrication of the first a-Si:H solar cell. The first silicon heterojunction (SHJ) device was reported in 1983 by Okuda et al. [16] with a conversion efficiency of 12.3 %. In 1992, Sanyo went one step further with the ACJ-HIT (Artificially Constructed Junction-Heterojunction with Intrinsic Thin-Layer) solar cells, demonstrating a solar cell with a conversion efficiency of 18.1 % [17]. At the moment of writing this thesis, the most efficient silicon based single junction solar cell is an interdigitated back contact (IBC) SHJ device with 26.6 % efficiency, fabricated by Kaneka Corporation with an area of $180\,cm^2$ [18, 19]. Over the past years, the field of photovoltaic energy conversion has attracted considerable attention resulting in rapid development in the field at both laboratory and industrial level. The focus is on reducing the cost and increasing the conversion efficiency of solar energy to electricity. This is further discussed in Section 1.2.

1.2 The importance of solar cells

It is not a coincidence that many prehistoric and ancient civilizations around the world worshiped the sun and constructed monuments over the years. They already understood the importance of the sun. The sun provides the energy that regulates the climate and the ecosystem on earth. This energy is abundant and free of carbon dioxide (CO_2) emissions. CO_2 is one of the primary greenhouse gases, to a large extent emitted from human activities in the recent years and is significantly contributing to global warming.

The power delivered by the sun to the earths upper atmosphere is about 174 PW and results in an average power density of about $1366\,\mathrm{W\,m^{-2}}$ [20, 21]. Atmospheric absorption and scattering reduce this value to about $1000\,\mathrm{W\,m^{-2}}$ on the surface of the earth. Moreover, there is a further reduction due to latitude-dependent oblique incidence, seasonal variations, diurnal variations, and weather conditions, which results in the global-average solar irradiance over land of about $183\,\mathrm{W\,m^{-2}}$ [21]. The available solar power globally (land plus ocean surface) is about 6500 TW, however, if only the land in locations where photovoltaics could be developed is considered the deliverable solar power drops to about 340 TW [22]. In a year this power corresponds to 2 978 400 TW h, which is significantly higher than the world energy demand. The International Energy Agency (IEA) estimates that the world energy consumption for the year 2014 was 109 613 TW h [23]. By comparing this world energy consumption to the deliverable solar power it becomes clear that the energy produced from solar cells is an alternative that can solve the energy demands of the planet. This is why solar cell technology can become important. However, further progress is needed in utilizing the energy delivered by the sun.

The evolution of the installed photovoltaic capacity in the world can be seen in Figure 1.2 [24]. In 2016 the photovoltaic capacity was at least 320 GW and the installed capacity is growing fast over the last few years. According to the BLUE Map scenario [25], the IEA estimates that in 2050 the photovoltaic installed capacity can be be 3000 GW generating 4500 TW h per year, which is estimated to be 11 % of global electricity supply [26].

In 2016 about 94 % of the total solar cell production was based on wafers of c-Si (both mono-crystalline and multi-crystalline silicon), while thin-film technologies covered only about 6 % of the market [24]. Out of the various materials that can be used in photovoltaics, silicon meets all the criteria to be the material of choice i.e. in terms of abundance of raw material, cost, safety issues, and efficiency of the solar cell device [27]. In 2016
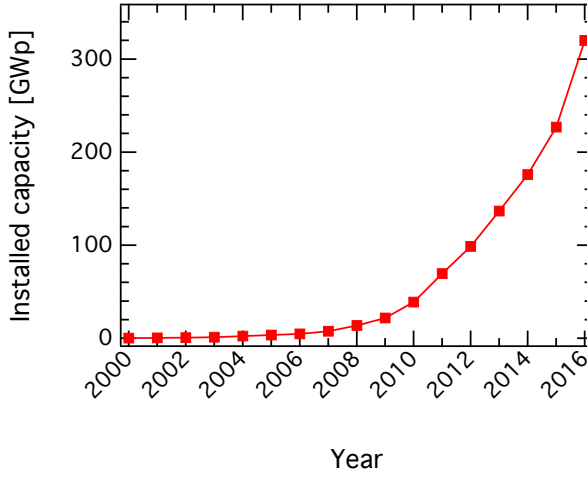
Figure 1.2: Evolution of photovoltaic installed capacity in the world [24].

silicon-wafer based photovoltaics was among the most efficient technologies [28], with the highest efficiency demonstrated by Kaneka Corporation with a 26.6 % SHJ device [18, 19].

1.3 Solar-cell operation and characteristics

Solar cells are based on semiconductor materials, which are materials that have an electrical conductivity (σ) in between that of metals and insulators ($10^{-8}\,\mathrm{S\,cm^{-1}} < \sigma < 10^3\,\mathrm{S\,cm^{-1}}$). The variation in conductivity of these materials is due to differences in the electronic band structure. At $T = 0\,\mathrm{K}$ the electrons of the outermost electron shell are in the lowest possible energy states, tightly bound to the atoms filling the so-called valence band. When $T > 0\,\mathrm{K}$ some electrons can gain enough energy and be excited to higher energy states, the conduction band, becoming delocalized i.e. able to conduct electric current. The highest energy level of the valence band (E_v) and the lowest energy level of the conduction band (E_c) are separated by a gap without available states for the electrons to occupy, the band gap (E_g). The electric properties of a semiconductor can be tuned with doping. When an impurity is added to substitute an atom, this impurity can donate an electron to the conduction band (in case the impurity is a donor) or accept an electron from the valence band (in case the impurity

is an acceptor), thus forming n-type and p-type material, respectively.

Figure 1.3: Simplified illustration of an ideal solar cell band structure. The processes of charge carrier generation, separation and collection are indicated with the numbers 1, 2 and 3, respectively.

In solar cells, illumination of a semiconductor material can result in an optical excitation, a process in which a photon with energy E_{ph} is absorbed by a covalently bonded electron allowing this electron to participate in current conduction. In terms of the electron energy state this process is described as an excitation of an electron from the valence band into the conduction band, leaving a hole in the valence band. Subsequently, the electrons and the holes diffuse in the absorber material of the solar cell, in the absence of an electric field until they recombine. For the solar cell operation separation of charge carriers should be realized before recombination. To separate the two opposite types of charge carriers materials are used that serve as semi-permeable membranes for either electrons or holes [29]. The charge carrier separation is followed by carrier collection at the contacts of the solar cell, when an external load is connected. During this process, the population of electrons and holes in the conduction and the valence bands is described by quasi-Fermi levels for electrons and holes, respectively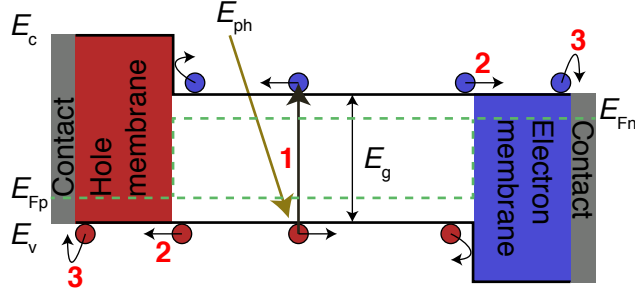. A simplified illustration of an ideal solar cell band structure and the process of carrier generation, separation and collection is shown in Figure 1.3.

Typically, a p-n junction is used in solar cells resulting in a rectifying behavior. For an ideal diode the dark current density varies according to [30]

$$J_{\text{dark}}(V) = J_{\text{o}}(e^{(qV/k_{\text{B}}T)} - 1), \tag{1.1}$$

where J_o is the saturation current density k_B is the Boltzmann's constant, q is the elementary charge, and T is the temperature. J_{dark} is the current density generated in a solar cell by applying an external voltage, when the solar cell is not under illumination. In an illuminated solar cell the overall current-voltage response will be given as

$$J(V) = J_{dark}(V) - J_L, \tag{1.2}$$

where J_L is the current density generated due to illumination. For an ideal diode Equation (1.2) becomes

$$J(V) = J_o(e^{(qV/k_BT)} - 1) - J_L. \tag{1.3}$$

In open-circuit condition (i.e., when the contacts of the solar cell are not connected to each other and no external current is flowing) the potential difference between the two contacts reaches the maximum value, known as the open circuit voltage (V_{OC}). When the potential difference between the two contacts reaches the maximum value, J_L and $J_{dark}(V_{OC})$ will exactly cancel out and V_{OC} is equal to

$$V_{OC} = \frac{k_BT}{q}\ln(\frac{J_L}{J_o} + 1). \tag{1.4}$$

When the solar cell is short circuited J_L can be approximated by the short circuit current density (J_{SC}), then

$$J_{SC} \approx J_L. \tag{1.5}$$

Figure 1.4 shows a typical J-V characteristic in the dark (blue) and under illumination (red). The solar cell delivers power in the voltage in the range $0 < V < V_{OC}$. The power delivered is shown in Figure 1.4 with the green curve and it reaches the maximum point at the voltage V_{mpp} and current density J_{mpp}. This maximum point is being determined by the value of the external parameters of the solar cell. These are V_{OC}, J_{SC} and the so-called fill factor (FF), which is defined as

$$FF = \frac{J_{mpp}V_{mpp}}{J_{SC}V_{OC}}. \tag{1.6}$$

Graphically, FF is a measure of the 'squareness' of the J-V characteristics. The more the J-V deviates from a perfect square, indicated with the pink rectangle in Figure 1.4, the smaller is the FF.
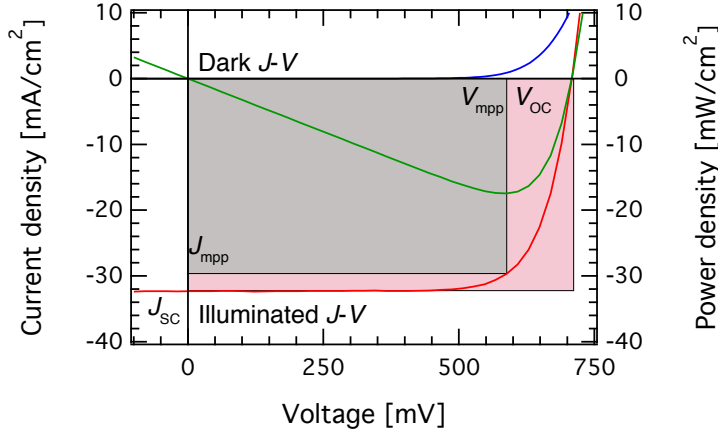
Figure 1.4: Typical current voltage characteristics in the dark (blue), under illumination (red) and the power voltage characteristics under illumination (green). J_{SC}, V_{OC}, J_{mpp} and V_{mpp} are indicated in the graph. The maximum power density is given by the area of the inner rectangle (gray). The outer rectangle (pink) indicates the power density for fill factor equal to 1.

The conversion efficiency of a solar cell (η) is given as the fraction of the maximum power delivered from the solar cell to the incident power, P_i,

$$\eta = \frac{J_{mpp}V_{mpp}}{P_i} \tag{1.7}$$

or using Equation (1.6), η is given as

$$\eta = \frac{J_{SC}V_{OC}FF}{P_i}. \tag{1.8}$$

Under AM 1.5 spectrum P_i is taken equal to $1000\,\mathrm{W\,m^{-2}}$. η, is the parameter that needs to be increased in solar cells, while keeping the fabrication cost low. A solar cell technology that is able to demonstrate high efficiency at relatively low cost is potentially the SHJ solar cell, which is discussed in the next section.

1.4 The silicon heterojunction solar cell

One of the main challenges in solar cell research is increasing η. For this purpose continuously more sophisticated solar cell structures are fabri-

cated. In many cases these structures require the use of complex and costly fabrication processes, not compatible with the industrial standards. SHJ solar cells are able to comply with the industrial standards, while at the same time yielding good performance.

A schematic of a standard SHJ solar cell structure can be seen in Figure 1.5. This schematic is based on the devices with record η of 24.7 % and 25.1 %, fabricated by Panasonic Corporation and Kaneka Corporation, respectively [31, 32]. Since then η has been further increased by using the IBC configuration, an approach in which both contacts are placed at the back of the solar cell. Although the IBC SHJ is a more complex structure in terms of fabrication, the basic characteristics of the solar cell remain similar. In a standard SHJ solar cell, thin intrinsic a-Si:H layers with 5–10 nm thickness are deposited on both sides of an n-type c-Si wafer having a thickness of 100–160 µm [31, 32]. An n-type wafer is used instead of a p-type wafer since it has been shown to be beneficial for the solar cell efficiency [33–35]. Especially SHJ solar cells, appear to perform better when using n-type wafers due to an asymmetry in the interface defect capture cross sections for electrons and holes and due to the band structure seen by the minority carriers [34]. After the deposition of the intrinsic a-Si:H layers, a p-type and an n-type a-Si:H layer is deposited in the illuminated and the non-illuminated side of the wafer, respectively, with a thickness in the range 5–10 nm for both layers. Afterwards, a transparent conductive oxide (TCO) layer is deposited on top of both the p- and n-type a-Si:H layers. Typically, the front and the back TCO layers have a thickness of 70 nm and 150–200 nm, respectively. The thickness of the TCO layer is chosen so that the layer can provide efficient carrier transport but also function as an anti-reflecting coating. The solar cell is finalized by the deposition of a metal grid at the front and full metal coverage or also a metal grid at the back. All layers for the SHJ fabrication can be deposited at temperature less than 250 °C. The main advantages of SHJ solar cells as compared to other technologies are the high efficiency potential and the cost reduction potential [36].

The low temperature processing used helps reducing the fabrication cost in two ways, firstly in the process itself by using a low thermal budget and secondly by allowing for the use of thinner wafers. Increased temperature processing can result in the breakage of thin wafers. Although SHJ solar cells do present these advantages, the fabrication of a complete device involves the deposition of multiple layers that serve various purposes in the device operation. These layers can affect one or more of the exter-

nal parameters and therefore also η, as described in Equation (1.8). The effect of the various layers in the device operation will be discussed in Section 1.5.
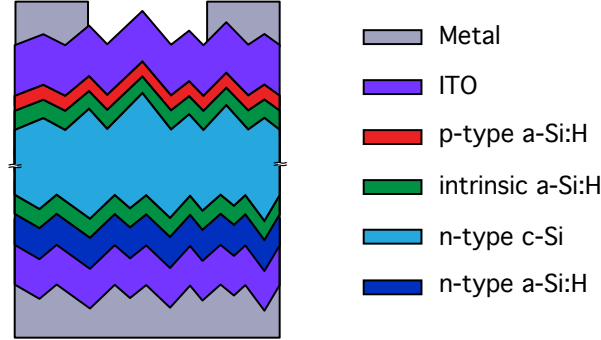
Figure 1.5: Sketch of a standard silicon heterojunction solar cell. The thickness of the layers indicated with the different colors is not drawn to scale.

1.5 Key points in silicon heterojunction solar cell performance

As already discussed in Section 1.4, SHJ solar cells present many advantages among solar cell technologies and are able to demonstrate a very good performance. To guarantee this performance the impact of the different layers in the SHJ device should be taken into account. It is not only the properties of the various layers that can influence the external parameters (V_{OC}, J_{SC} and FF) of the device and therefore η, but also the properties of the interfaces formed between the layers. The qualitative impact of the various layers and interfaces in the SHJ device is summarized in Table 1.1 [36]. In the rest of this section each of the external parameters will be discussed separately. The discussion will be focused on the layers that impact the external parameters the most, according to Table 1.1.

One of the most important parameters in SHJ devices that enables the high efficiency is the V_{OC}. The V_{OC} defines the separation of the quasi Fermi levels for electrons and holes, at which the recombination of electrons and holes is in equilibrium with generation throughout the entire cell

[29]. The presence of the abrupt heterojunction between c-Si and a-Si:H results in an increased built-in voltage, which allows for the increased value of V_{OC} as compared to homojunction devices [36]. The built-in voltage is the voltage drop across the depletion region at thermal equilibrium. Qualitatively, the maximum V_{OC} that can be achieved by a solar cell is equal to the built-in voltage [37]. Table 1.1 clearly shows that the regions strongly affecting the V_{OC} are the c-Si wafer, the c-Si/a-Si:H interfaces and the a-Si:H layers. Increased recombination in any of these regions will limit the device performance. This recombination can be evaluated since it is directly related with a quantity called the effective lifetime (τ_{eff}), which is discussed further in Section 2.2.1. This lifetime is determined by several recombination processes in the device, a.o. the defect density in different regions of the device, and directly controls the V_{OC}. Typically, the bulk defect density in the wafers used for the fabrication of SHJ devices is relatively small leading to a long bulk lifetime. The lifetime of the carriers (and therefore also the V_{OC}) is then determined primarily by the defect density at the interfaces between the c-Si wafer and the intrinsic a-Si:H layer through surface recombination. The surface is often characterized by an increased defect density. The influence of the surfaces is further enhanced by two fabrication processes that take place. The texturing of the c-Si wafer, commonly used to enhance light trapping and to increase J_{SC} (J_{SC} will be discussed further in the next paragraph), and the subsequent cleaning. These two fabrication processes can significantly alter the c-Si surface defect density and increase recombination rate. Furthermore, for the SHJ device fabrication a very thin a-Si:H layer is deposited on the c-Si surface to form the interface between c-Si and a-Si:H. The properties of the a-Si:H layer are influenced by the deposition conditions and these properties will also have an effect on the V_{OC}. Finally, there will be an impact of the doped layer properties. The highest V_{OC} is obtained when the Fermi level in the thin a-Si:H layers is as close as possible to the conduction or valence band [36]. This is achieved by increasing the doping density of the doped layers. However, increasing the doping density increases also the defect density, which will in turn increase the recombination rate in some parts of the device.

The J_{SC} in the standard SHJ solar cell structure is strongly affected by the front layers, where light enters the device. Essentially, to increase J_{SC}, the absorption in the absorber layer (i.e. the c-Si wafer) should be enhanced. For this purpose, the area covered by the front metal grid should be minimized as much as possible, while the absorption in the TCO and the a-Si:H

layers should be decreased. In the TCO a decrease in the absorption can be achieved by reducing the carrier concentration in the layer, while increasing at the same time the carrier mobility. In the a-Si:H layers the absorption is reduced by alloying a-Si:H with carbon or oxygen, increasing the band gap of the layer. Although, it is necessary to decrease absorption of these layers in order to improve J_{SC}, it is at the same time essential to maintain or improve their conductivity. The conductivity will have an impact on the FF of the device.

The FF is a rather complex parameter to analyze in a solar cell because it depends on all layers and interfaces. This is shown in Table 1.1. The FF in SHJ solar cells is mainly influenced by the series resistance of the various layers. Therefore, increased conductivity is desired. However, as was already discussed, increased conductivity of the front layers will increase parasitic absorption and decrease J_{SC}. This discussion makes clear that there is an interplay of the external parameters.

Table 1.1: Qualitative impact of the various layers and interfaces of a silicon heterojunction solar cell on the external parameters, used to evaluate the efficiency of the solar cell [36].

Layer	V_{OC}	J_{SC}	FF
Front metal grid	-	●●●	●●●
Metal/TCO interface	-	●	●●
Front TCO	●	●●●	●●●
TCO/a-Si:H interface	●	●	●●
Front a-Si:H	●●	●●●	●●
a-Si:H/c-Si interface	●●●	-	●●
c-Si	●●	●●●	●
c-Si/a-Si:H interface	●●●	-	●
Back a-Si:H	●●	-	●
a-Si:H/TCO interface	●	●	●
Back TCO	●	●	●
TCO/metal interface	-	●	●●
Back metal	-	●	●●

1.6 Outline of this thesis and contribution to the research field

It has been more than 40 years since the first study of the a-Si:H/c-Si heterojunction for photovoltaic application by Fuhs et al. [15]. During these 40 years the SHJ solar cell technology has been investigated extensively. Currently the best laboratory device has reached η of 26.6 % [18, 19], approaching the theoretical efficiency limit of 29.4 % [38, 39] for a single junction silicon solar cell. Although SHJ solar cell technology has been extensively studied and has demonstrated such a good performance, there are still aspects of the device operation not well understood. Especially when η is reaching the limit even minor improvements can be of importance. This thesis discusses certain aspects of SHJ solar cells and has a main focus on the surface passivation of the c-Si wafer. In this way it aims to contribute to the understanding of SHJ solar cell fabrication and operation, helping to improve the SHJ solar cell performance. The rest of this thesis is organized as follows.

In Chapter 2 the general processes used for SHJ sample fabrication and characterization in this work are discussed. Firstly, the processes used for the fabrication of the samples and devices are described. These processes include the wafer texturing and cleaning, the deposition of the a-Si:H layers, the deposition of the TCO and finally the deposition of the metal contacts. Secondly, the various techniques used to characterize the samples and devices fabricated in this work are explained. Although the experimental methodology is given in Chapter 2, the specific details relevant for the results presented in Chapters 3 to 6 are given in each chapter separately.

In Chapter 3 some of the cleaning procedures commonly used to clean the c-Si wafer before the SHJ device fabrication are investigated. The c-Si wafer serves as the absorber layer and can be considered the core of the SHJ device. As is shown in Table 1.1, the properties of the c-Si wafer and the optical confinement achieved can have a major impact in J_{SC} [36, 40]. In order to achieve increased absorption of light in the c-Si wafer and ensure maximum possible J_{SC}, random texturing of the wafer is applied. The process of texturing will have a great impact on the surface of the wafer, on which the a-Si:H layers will be deposited and form the a-Si:H/c-Si interfaces. In this way a damaged surface with increased micro roughness will result in poor passivation of the c-Si wafer i.e. an a-Si:H/c-Si interface

characterized by increased recombination rate. This increased recombination rate results in a solar cell with a decreased V_{OC}. By applying an appropriate cleaning procedure the roughness on the facets of the pyramidal surface of the c-Si wafer can be reduced, yielding interfaces that do not limit the V_{OC}, after the solar cell fabrication. In Chapter 3, besides investigating commonly used cleaning treatments such as cleaning with nitric acid (HNO_3), RCA, and Piranha, we apply an approach that consists of multiple steps of wet-chemical oxidation using HNO_3 and subsequent oxide removal. Using this approach we obtain similar passivation on textured and polished substrates. The best η achieved on a SHJ solar cell fabricated using a textured substrate is 20.8 %. We suggest that the effects observed on passivation are directly related to the efficient removal of nano-scale roughness from the surface of the c-Si wafer.

Besides the surface of the c-Si wafer, the deposition conditions and the properties of the resulting a-Si:H layer can significantly impact V_{OC}. The effect of the deposition conditions and the a-Si:H properties on the c-Si passivation are investigated in Chapter 4. As a result excellent surface passivation is demonstrated by depositing the a-Si:H passivation layers in a high-pressure and high hydrogen dilution regime. The results show a weak dependence of τ_{eff} on hydrogen dilution of the a-Si:H layer, and a strong dependence on the substrate temperature, with τ_{eff} in the order of 10 ms obtained for different nanostructures. The increase in τ_{eff} when using these hydrogen-diluted plasma conditions is explained by extra hydrogenation of the interface during deposition, while simultaneously etching the deposited layer. The etching of the layer prevents void formation during a-Si:H growth thus resulting in a layer with increased density.

The passivation of c-Si is often studied using wafers passivated with thicker intrinsic a-Si:H layers than what is commonly used in SHJ devices. It has been observed that thicker passivation layers can result in higher τ_{eff}, yet the dependence of τ_{eff} on the thickness of the a-Si:H layer has not been investigated in detail so far. In Chapter 5 the a-Si:H thickness dependency of τ_{eff} on c-Si substrates passivated with intrinsic a-Si:H is studied. For this purpose c-Si wafers are passivated with a-Si:H layers thicker than the layers used in SHJ solar cells and a wet-etching method is used to accurately reduce the thickness of the passivation layers and study τ_{eff}. Results show that there is indeed a strong thickness dependency of the τ_{eff}. During the growth of the layer the deposition conditions can alter the properties of the passivation layer, affecting τ_{eff}. By using the wet-etching method to reduce the thickness of an initially thicker a-Si:H layer

it is shown that the increased τ_{eff} with the thickness of the passivation layer is a direct effect of the increased thickness of the layer rather than an effect of the deposition conditions. For thin a-Si:H passivation layers τ_{eff} appears to be mainly influenced by the recombination at the external a-Si:H surface, i.e. the air/a-Si:H interface, while for thick a-Si:H layers τ_{eff} is predominantly determined by the bulk a-Si:H defect density and/or the bulk c-Si wafer defect density. Furthermore, the etching method is used to reduce the thickness of initially thicker passivation layers to about 7 nm and fabricate SHJ devices. Using this approach V_{OC}s above 715 mV are obtained for $280 \pm 20 \, \mu$m wafer thickness.

In addition, the wet-etching approach is used to study the passivation properties of hydrogenated amorphous silicon oxide layers (a-SiO$_x$:H), passivating c-Si wafers. In Chapter 6 a-SiO$_x$:H with varying oxygen content (c_O) and similar hydrogen content are used to passivate c-Si wafers. Using our deposition conditions an τ_{eff} above 5 ms is obtained for $c_O \leqslant$ 6 at. %, for passivation layers with thickness of 36 ± 2 nm. The thickness of the layers is subsequanlty reduced to 7 nm and p- and n-type doped layers are deposited fabricating a device structure. The deposition of the doped layers gives an insight on the passivation mechanism, which appears to be determined by the field-effect rather than by chemical passivation. After the deposition of the doped layers, τ_{eff} appears to be predominantly determined by the doped layers themselves and is less dependent on the c_O of the a-SiO$_x$:H layers.

Finally, the main conclusions of this thesis and some recommendations to further expand this work can be found in Chapter 7. The contributions of this thesis to the research field can be summarized as follows:

- The influence of commonly used cleaning procedures on the passivation of textured c-Si wafers is demonstrated. Moreover, by using a cleaning approach with HNO$_3$, similar passivation results are obtained for polished and textured c-Si wafers. Using this cleaning approach with HNO$_3$, a SHJ solar cell with η of 20.8 % has been fabricated.

- Excellent surface passivation of c-Si is demonstrated by depositing intrinsic a-Si:H in a high-pressure and high hydrogen dilution regime. Using these deposition conditions τ_{eff}s larger than 10 ms are achieved.

- The thickness-dependent passivation of c-Si with a-Si:H is explained in terms of the bulk c-Si and a-Si:H defect density and recombina-

tion at the external a-Si:H surface, i.e. the air/a-Si:H interface. For this explanation a nanometer accurate wet-etching method is established. This method is also used in the fabrication of SHJ solar cells and V_{OC}s above 715 mV for wafer thickness of $280 \pm 20\,\mu m$ are obtained.

- The passivation mechanism of SHJ solar cells with intrinsic a-SiO$_x$:H passivation layers is understood in terms of field-effect passivation rather than chemical passivation. Moreover, deposition conditions are demonstrated that result in τ_{eff}s above 5 ms for c-Si wafers passivated with intrinsic a-SiO$_x$:H of $c_O \leqslant 6$ at. %.

2

Instrumentation for silicon heterojunction sample fabrication and characterization

In this chapter the experimental techniques used in this thesis are presented. The chapter is separated in two sections. In Section 2.1 the texturing and cleaning of the wafers, and the tools used for the fabrication of silicon heterojunction samples and devices are described. Then in Section 2.2 the various techniques used for the characterization of the samples and devices presented in this work are explained. Additional experimental details specific to the work presented in Chapters 3 to 6 are given in the Experimental detail subsection of each chapter.

2.1 Fabrication processes

In Section 2.1 the main steps used in the fabrication of silicon heterojunction (SHJ) samples and devices are discussed. For a complete process flowchart see Appendix A. The fabrication of a SHJ device starts with wafer texturing and cleaning. Subsequently, the intrinsic and doped amorphous silicon (a-Si:H) layers are deposited, using the radio-frequency plasma-enhanced chemical vapor deposition (RF-PECVD) technique. The deposition of the a-Si:H layers is followed by the deposition of the transparent conductive oxide (TCO) using magnetron sputtering. Finally, the front and back metal contacts are deposited, using screen printing and/or evaporation (thermal and e-beam), respectively.

2.1.1 Wafer texturing and cleaning

For the experimental results presented in this work (except the results obtained using Fourier-transform infrared spectroscopy (FTIR)) float-zone (FZ) phosphorus-doped double-side polished crystalline silicon (c-Si) wafers from TopSil were used with <111> or <100> orientation, 1–5 Ω cm resistivity and 280 ± 20 µm thickness. For the results obtained with FTIR one side polished phosphorus-doped c-Si Czochralski wafers were used with a thickness of 525 ± 25 µm and resistivity of 10–20 Ω cm.

In order to reduce reflection loses, textured wafers are typically used for the fabrication of SHJ devices. In this work textured wafers are used in Chapter 3. For the texturing, c-Si wafers with orientation <100> were anisotropically etched using an aqueous alkaline mixture constisting of 5 % tetramethyl ammonium hydroxide (TMAH) and 7.4 % isopropyl alcohol (IPA). During the texturing the solution was continuously stirred at 100 rpm and kept at 80 °C.

Before the deposition of the a-Si:H silicon layers the c-Si wafers were cleaned in order to remove surface chemical contaminants and particulate impurities. For this purpose, two different cleaning methods can be used [41]: dry and wet cleaning methods. The advantage of the wet over the dry cleaning methods is the absence of the plasma process usually involved in dry methods. The plasma process results in ion bombardment of the c-Si wafer surface, which in turn can result in a subsequent increase in surface defect density. In this work a wet cleaning method is used, which consists of three subsequent steps:

- Firstly, the wafer is immersed for 10 min in 99 % nitric acid (HNO_3) at room temperature.

- Subsequently, the wafer is immersed for 10 min in 69.5 % HNO_3 at 105 ± 5 °C.

- Finally, the wafer is immersed in a 0.55 % hydrofluoric acid(HF) solution at room temperature. For wafers with orientation <111> and for textured wafers an immersion time of 75 s was used, whereas for <100> wafers this was 20 s.

In between the cleaning steps the wafers were rinsed in high purity deionized water (18 MΩ cm). The immersion of the samples in HNO_3 aims in removing organic and metal contaminants from the surface of the wafer. However, the efficiency of the reaction of HNO_3 with different metals depends on the temperature and dilution of the HNO_3 solution. For this reason two HNO_3 cleaning steps are used. The native oxide or any further silicon oxide layer formed during the immersion of the wafer in HNO_3 was removed in the final HF step. The aforementioned immersion time for the final HF step was chosen after optimization experiments performed by Zhang [42]. During the HF step it is essential to make sure that the immersion time is sufficiently long to remove the silicon oxide layer. Prolonged HF wafer exposure has been associated with an increase in wafer surface roughness [43]. A possible explanation of the increase in surface roughness during the HF step is the slow oxidation of the H-passivated surface, [44, 45] followed by a fast removal of the surface oxide by HF [46]. The effectiveness of the cleaning method used in this work is investigated and compared with other commonly used wet-chemical cleaning methods in Chapter 3. In Chapter 3 the investigation will focus on textured wafers. Texturing is an additional step that the wafers go through and in this case the effect of cleaning is expected to be more profound. After the texturing and/or the cleaning of the wafers, the amorphous silicon (a-Si:H) layers were deposited.

2.1.2 Plasma-enhanced chemical vapor deposition

The a-Si:H layers were deposited by means of plasma-enhanced chemical vapor deposition (PECVD). The excitation frequency applied between the two electrodes was 13.6 MHz. For this process, the cleaned wafer is placed in the cluster tool and transfered into a high vacuum chamber. In

the chamber the wafer is mounted on a sample holder that serves as the ground electrode. The temperature of the chamber is controlled by heating elements. The precursor gases are admitted into the chamber and the pressure of the gases in the chamber is controlled. An AC voltage is then applied across the two electrodes and the plasma is ignited. After the ignition, gas dissociation takes place, followed by complex chemical reactions in the plasma and the substrate surface, resulting in the deposition of the layer. A schematic representation of the PECVD chamber with a loaded sample can be seen in Figure 2.1 (a).
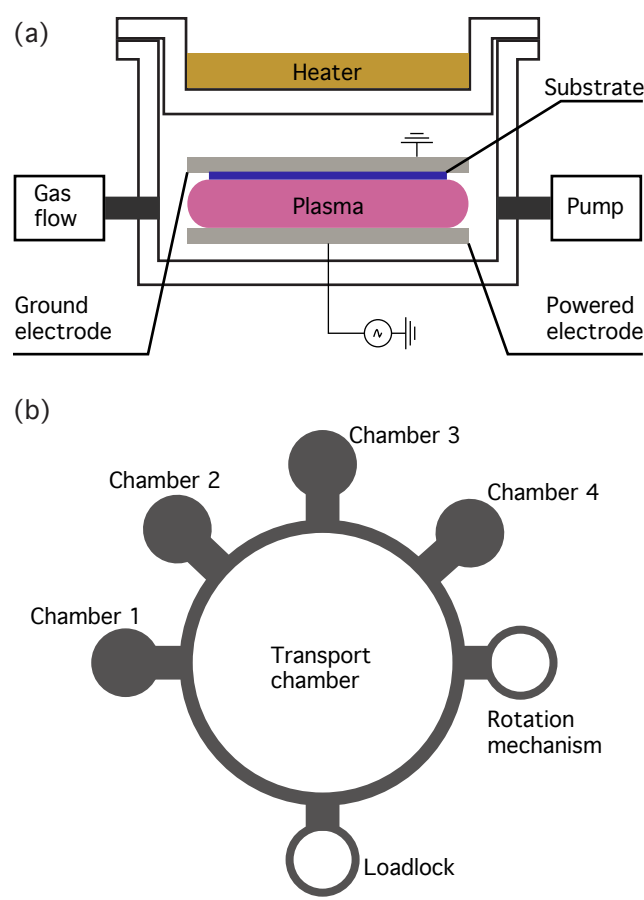

Figure 2.1: Schematic of (a) the PECVD reaction chamber and (b) the PECVD cluster tool with the multiple deposition chambers

The sketch of the cluster tool layout can be seen in Figure 2.1 (b). It can

be seen that the system consists of multiple chambers, which are used for the deposition of different layers, i.e. boron-doped, phosphorus-doped and intrinsic layers. The purpose for using different chambers is to avoid cross-contamination. Moreover, the cluster tool has a mechanism in which the sample can be placed and rotated. In order to fabricate SHJ devices the a-Si:H layers must be deposited on both sides of the wafer. This mechanism allows the wafer to be rotated in the vacuum system, without a vacuum break. Besides silane SiH_4, which was always used as a source for silicon, diborane (B_2H_6) was used as a source for boron (thus depositing boron-doped a-Si:H) and phosphine (PH_3) as a source for phosphorus (thus depositing phosphorus-doped a-Si:H). For some experiments, the gases were diluted with additional hydrogen (H_2). For the hydrogenated amorphous silicon oxide (a-SiO$_x$:H) layers discussed in Chapter 6 CO_2 gas is used additionally.

During the PECVD deposition, parameters such as the gas flow rate, the pressure, the power density and the temperature of the chamber will significantly alter the properties of the layers deposited. The cluster tool used in this work was built by Elettrorava S.p.A. under license from MVSystems. After the intrinsic and doped layers are deposited, a transparent conductive oxide (TCO) is needed. The TCO is deposited by means of radio-frequency magnetron sputtering.

2.1.3 Radio-frequency magnetron sputtering

Radio-frequency magnetron sputtering is a physical vapor deposition method i.e. a method in which no chemical interactions take place between the source gas and the target material. An inert gas, argon is used and a plasma is ignited. Then ions and/or highly energetic atoms are bombarding a target. In this way, atoms are released from the target and diffuse towards the substrate. In this work indium tin oxide (ITO) is used as TCO.

For the ITO sputtering, a Kurt J. Lesker Company radio-frequency magnetron system was used with a target composition In_2O_3:SnO_2 = 90:10 wt.%. The deposition substrate temperature and pressure were set at $110\,°C$ and $10\,\mu bar$, respectively. In order to reduce the damage induced on the sample during the sputtering a two step deposition approach was used [47]. In this way, approximately the first $30\,nm$ were deposited using a power density of $0.05\,W\,cm^{-2}$ and the rest of the layer at $0.1\,W\,cm^{-2}$. In order to fabricate a SHJ device the ITO deposition must be followed by metal contact deposition.

2.1.4 Metal evaporation and screen printing

For the metal contact deposition two different methods are used: evaporation and screen printing.

Evaporation is mainly used for the back contact of the device, which consists of a 100 nm silver (Ag), 30 nm chromium (Cr) and 1900 nm aluminum (Al) metal stack fully covering the back side of the device. The reason for using Al as the main metal for the contact is the lower material cost compared to Ag and its resistance to oxidation. However, a thin layer of Ag is still used since the contact resistance between Ag and ITO is lower than that between Al and ITO. Moreover, in case of annealing Al can form an oxide by reacting with oxygen atoms in the ITO [48, 49] increasing in this way the contact resistance between the ITO and the metal. Cr is used in between Al and Ag to prevent the two metals from mixing. Ag is deposited by means of thermal evaporation while Cr and Al are deposited using electron-beam evaporation. For thermal evaporation the material is placed inside a tungsten boat and a high voltage is applied. The tungsten boat serves as a resistor, heating up and melting the material. Ag has a melting point of about 960 °C. Cr has much higher melting point of about 3400 °C and in this case electron-beam evaporation is used. For electron-beam evaporation, electrons are generated, accelerated and directed on a crucible that contains the material. The electrons are generated by thermal emission and by the moment they hit the crucible, they attain enough kinetic energy to melt the material. Although Al has a lower melting point than Ag, it is also deposited by electron-beam evaporation. This is because melted Al can alloy with the tungsten boat, which is used as a sample holder fo Ag.

The front contact is on the illuminated side of the device and it is deposited by screen printing in the shape of H pattern. The reason for using screen printing is the requirement to minimize the shadow fraction, while keeping the grid line resistance as low as possible. This is achieved by keeping the height to width ratio of the grid line as high as possible. In a screen printer three of the most crucial parts are the frame, the screen and the squeegee. The metal is placed on the screen in the form of viscous paste. The paste used for this work is DuPont Solamet PV416, which is a silver based polymer composition. The screen consists of an interwoven thin wire mesh with openings in the shape of the H pattern and is affixed under high tension at the frame. The screens used in this work are made by KOENEN GmbH and have a mesh with the following specifi-

cations: stainless steel fabric with 300 mesh and 0.020 µm wire diameter, high tension calendared type with 22.5° mesh angle. The mesh is coated with micro-coating emulsion layer with thickness over mesh of 16 ± 2 µm. During the printing process the squeegee comes in contact with the screen, pushing the screen onto the surface of the sample. The squeegee moves across the surface of the screen, while at the same time it coerces the metal paste to pass through the screen openings and be deposited on the sample. A schematic representation of the screen printing process is shown in Figure 2.2.
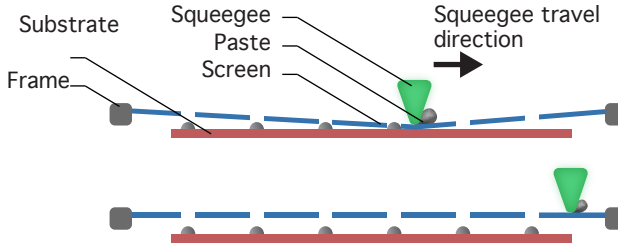
Figure 2.2: A schematic representation of the screen printing process [50]. The squeegee is pressing down the screen, bringing it into contact with the sample. As the squeegee moves across the sample, the metal paste is pushed though the openings of the screen and is deposited on the sample.

2.2 Characterization techniques

In this section the main characterization techniques and the setups used in this thesis are described. These techniques were used to determine the properties of various layers or characterize SHJ devices. Specifically, the photoconductance decay technique was used to measure the wafer minority carrier effective lifetime (τ_{eff}). The optical properties and thickness of the deposited layers were determined by means of spectroscopic ellipsometry (SE), while information on the composition and structure of the layers was mainly obtained by means of Fourier-transform infrared (FTIR) spectroscopy and Raman spectroscopy. Illuminated current-voltage and external quantum efficiency (EQE) measurements were used to determine the performance of the fabricated SHJ devices.

2.2.1 Photoconductance decay

Photoconductance decay measurements are used extensively in Chapters 3 to 6 of this thesis to determine the wafer minority carrier τ_{eff}. τ_{eff} as a quantity expresses the characteristic time needed for the excess minority carriers in the wafer to recombine after a photoexcitation.

The following explanation is based on the book of Rein [51]. Generation refers to the process in which an electron in the valence band (E_{v}) gains enough energy and is excited to the conduction band (E_{c}). Recombination on the other hand refers to the process in which an electron in E_{c} loses energy and recombines with an unoccupied state in E_{v}. In thermal equilibrium the generation rate equals the recombination rate. Upon photoexcitation excess electrons and holes are generated and a new equilibrium is reached, characterized by increased recombination and generation. If the source of photoexcitation is then switched off, the excess carrier density will drop until thermal equilibrium is reached. However, this process does not occur instantaneously. Assuming charge neutrality and the absence of trapping states the decay of excess charge carriers is given as

$$\frac{\partial \Delta n}{\partial t} = -U(\Delta n, n_0, p_0), \tag{2.1}$$

where Δn the excess carrier density, n_0 the thermal equilibrium electron concentration and p_0 the thermal equilibrium hole concentration. U is the net recombination rate ($U = R - G_0$, with R the recombination rate and G_0 the thermal equilibrium generation rate) and depends on the various recombination mechanisms. These recombination mechanisms are radiative, Auger, Shockley-Read-Hall in the bulk of the wafer, and surface recombination. In the simple case of one recombination mechanism, the solution to Equation (2.1) is an exponential decay of the initial photoexcited excess carrier population. The carrier lifetime refers to the time constant of this exponential decay, defined as

$$\tau(\Delta n, n_0, p_0) := \frac{\Delta n}{U(\Delta n, n_0, p_0)}. \tag{2.2}$$

Considering the different physical recombination mechanisms that contribute to the net recombination, an effective recombination rate can be defined, as the sum of the individual recombination rates. τ_{eff} will then be given as the sum of the reciprocal carrier lifetime related to the contribut-
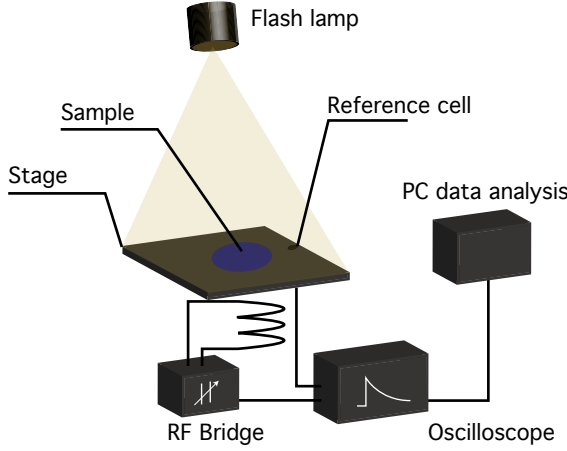
Figure 2.3: Schematic representation of the photoconductance decay measurement setup.

ing recombination processes

$$\frac{1}{\tau_{\text{eff}}} = \frac{1}{\tau_{\text{rad}}} + \frac{1}{\tau_{\text{Auger}}} + \frac{1}{\tau_{\text{SRH}}} + \frac{1}{\tau_{\text{surf}}}, \qquad (2.3)$$

where τ_{rad}, τ_{Auger}, τ_{SRH} and τ_{surf} are the lifetimes related to the radiative, Auger, Shockley-Read-Hall and surface recombination processes, respectively. In Equation (2.3) τ_{rad}, τ_{Auger} and τ_{SRH} are related to processes that take place in the bulk of the wafer. Therefore these three processes can be expressed by the bulk lifetime (τ_{bulk}) and Equation (2.3) becomes

$$\frac{1}{\tau_{\text{eff}}} = \frac{1}{\tau_{\text{bulk}}} + \frac{1}{\tau_{\text{surf}}}. \qquad (2.4)$$

The lifetime in this work is measured using a Sinton WCT-120 instrument. The sample is placed on a stage, underneath which a coil couples the sample inductively to an RF bridge. The sample is then illuminated by a flash and changes in the photoconductance of the sample are used to determine τ_{eff} [52]. A schematic representation of the photoconductance decay set up is shown in Figure 2.3 The Sinton WCT-120 can be used in steady-state and transient mode depending on the measured τ_{eff}. In this work the transient mode is used mostly. Typically, steady-state mode is

used for $\tau_{\text{eff}} < 100\,\mu s$. The lifetime in the general case is expressed as [53]

$$\tau_{\text{eff}} = \frac{\Delta n}{G - \dfrac{\partial \Delta n}{\partial t}}.$$ (2.5)

In Equation (2.5) τ_{eff} is given in steady-state and transient mode for $\partial \Delta n / \partial t \equiv 0$ and for $G \equiv 0$, respectively. The requirement for the two modes to be valid is to have an illumination source with decay much larger than τ_{eff} of the sample in the steady-state mode and much larger than τ_{eff} of the sample in transient mode.

2.2.2 Spectroscopic ellipsometry

For the fabrication of SHJ devices thin (i.e. in the nm range) a-Si:H and ITO layers are deposited. SE is used in Chapters 3 to 6 to analyze these layers and determine their thickness and optical properties.
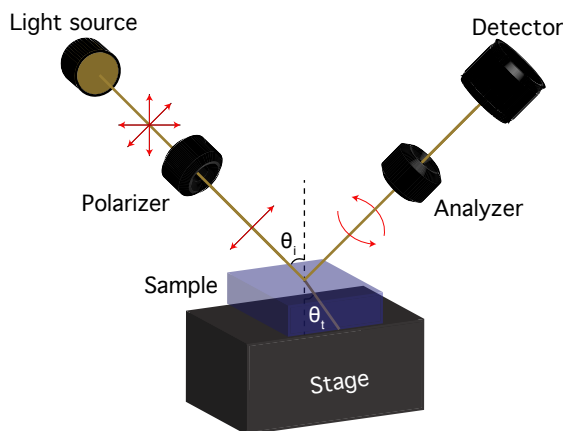

Figure 2.4: Schematic representation of the spectroscopic ellipsometry measurement setup.

The layers were deposited on wafer or glass substrates and placed on the SE setup as shown in Figure 2.4. A beam of light with known polarization interacts with the sample and the output polarization is detected. The complex amplitude reflection coefficients for p and s polarization are

given by the Fresnel equations [54]

$$r_\text{p} = \frac{N_\text{s} \cos\theta_\text{i} - n_\text{a} \cos\theta_\text{t}}{N_\text{s} \cos\theta_\text{i} + n_\text{a} \cos\theta_\text{t}} \quad \text{and} \quad r_\text{s} = \frac{n_\text{a} \cos\theta_\text{i} - N_\text{s} \cos\theta_\text{t}}{n_\text{a} \cos\theta_\text{i} + N_\text{s} \cos\theta_\text{t}}, \quad (2.6)$$

where n_a is the real index of refraction of the ambient, $N_\text{s} = n_\text{s} - ik_\text{s}$ where n_s is the real index of refraction of the sample and k_s is its extinction coefficient, θ_i is the angle of incidence, and θ_t is the complex angle of transmission. The measured wavelength dependent parameters Ψ and Δ are related with r_p and r_s through

$$\tan\Psi e^{\text{i}\Delta} = \frac{r_\text{p}}{r_\text{s}} = \rho. \quad (2.7)$$

After the measurement a mathematical model that describes the properties of the measured layer is used to fit Ψ and Δ. The model used throughout this thesis to fit the data obtained for a-Si:H is the Cody-Lorentz model [55], which was found to give better fittings than the commonly used Tauc-Lorentz model [56]. With the fitting the thickness of the layer and the optical properties of the layer are determined. The SE ellipsometer used in this thesis is from J.A. Woollam Co.

2.2.3 Reflectance measurements

Reflectance measurements are used in Chapter 3 to determine the optical properties of the c-Si wafer after texturing. For the reflectance measurements a PerkinElmer Lamda 950 UV/VIS spectrometer is used with an integrating sphere. The inside wall of the integrating sphere is covered with spectralon, a polytetrafluoroethylene-based material that makes the covered surface highly scattering and reflective for a broad range of wavelengths.Two detectors are placed inside the sphere that measure the total intensity of the reflected light in the sphere. A photomultiplier tube that measures the light intensity for wavelengths below 860.6 nm and a lead sulfide detector that measures the light intensity for wavelengths above 860.6 nm. The reflectance is calculated according to:

$$R = \frac{(R_\text{meas} - R_\text{dark})R_\text{ref}}{R_\text{ref} - R_\text{dark}}, \quad (2.8)$$

where R_meas is the reflectance measured from the sample, R_dark is the reflectance measured when a spectralon material is place in the position of

the sample and the sampling beam is off and R_{ref} is the reflectance measured when the spectralon material is place in the position of the sample and the sampling beam is on.

2.2.4 Fourier-transform infrared spectroscopy

The properties of the intrinsic a-Si:H layers in SHJ solar cells are important in determining the passivation quality and the solar cell V_{OC}. FTIR spectroscopy is a method that provides information on the structure and chemical composition of materials. FTIR spectroscopy is used in Chapter 6 to determine the hydrogen and oxygen content of a-Si(O_x):H layers grown with different deposition conditions.

In FTIR spectroscopy, photons with energy in the mid-infrared range are emitted from a source and incident on the sample. Depending on the structure and chemical composition of the sample, various rotational and vibrational transition are excited, resulting in absorption of photons at different energies. Typically, the absorption or transmission peak is plotted as a function of wavenumber and the absorption bands in the spectrum are associated with specific chemical boding configurations. In table Table 2.1 the absorption peak positions and the corresponding excitation modes relevant to the a-Si(O_x):H layers shown in Chapter 6 are given.

Table 2.1: Absorption peak position and corresponding vibrational mode for a-Si(O_x):H layers.

Wavenumber (cm^{-1})	Vibrational mode
640	Si-H wagging mode [57]
780	Si-O-Si-H [58]
840-890	SiH_2 and $(SiH_2)_n$ bending mode, SiH_3 symmetric deformation [59]
980-1080	Si-O-Si stretching mode [58]
1106	O-Si-Si-O stretching mode [60, 61]
2000	SiH stretching mode [59]
2090	SiH_2 stretching mode [59] or HSi-Si_2O [62]
2200	HSi-SiO_2 [62]
2260	HSi-O_3 [62]
3650	Si-OH stretching mode [63]

For the determination of the hydrogen content (c_H), an a-Si(O_x):H layer

is deposited on a wafer substrate and the FTIR spectrum is measured in transmittance mode. The measured spectrum is corrected for the substrate absorption by using a separate measurement, performed on a bare wafer. Moreover, interference fringes can be present in the measured spectrum. The interference is removed by using a linear fitting in the range 550–750 cm^{-1}. The absorption coefficient is then determined from the transmittance spectrum using

$$T = e^{-ad}, \tag{2.9}$$

where T is the transmittance, a is the absorption coefficient and d is the thickness of the layer. The integrated absorption (I) can then be calculated from the absorption coefficient according to [64]

$$I = \int \left(\frac{a}{\omega} \right) d\omega, \tag{2.10}$$

where ω is the frequency in cm^{-1}. The hydrogen concentration is then related to I with a proportionality constant A_H

$$N_H = A_H I. \tag{2.11}$$

In Equation (2.11) the proportionality constant is equal to $A_H = 2.1 \pm 0.2$ cm^{-1} [64]. The hydrogen content is then calculated by dividing with the c-Si number density (N_{Si}). This is expressed as

$$c_H = \frac{N_H}{N_{Si}} 100\%. \tag{2.12}$$

The oxygen content (c_O) is determined using the method by Lucovsky et al. [65]. For this purpose, the background is removed by using a linear fitting in the range 750–1200 cm^{-1} and the FTIR data is fitted by two Gaussian functions positioned at 980 cm^{-1} and at 1106 cm^{-1}. The integrated absorption is calculated in units of eV cm^{-1}. c_O is then directly given by

$$c_O = A_O I, \tag{2.13}$$

where A_O is the proportionality constant equal to 0.156 at. eV^{-1} cm.

In this work a Thermo Scientific Nicolet 5700 with an infrared lamp spectrometer is used. The measurements are carrier out in the spectral range of 400–4000 cm^{-1}.

2.2.5 Raman spectroscopy

Similar to FTIR spectroscopy, Raman spectroscopy is used to obtain structural information and the relative hydrogen content of intrinsic a-Si:H layers grown with different deposition conditions. This is further discussed in Chapter 4.

Raman spectroscopy is a nondestructive optical technique, based on the inelastic scattering of photons emitted from a light source with the lattice of the material under investigation. The interaction of light with the sample, results in the symmetrical shift of the photon frequencies with respect to the excitation frequency. The shift to lower and higher frequencies is known as the Stokes and the anti-Stokes shift, respectively. The absolute value of this shift is known as Raman shift. Typically, in a Raman spectrum the intensity of the scattered light is plotted as a function of the Raman shift expressed in cm^{-1}. For analysis purposes the Stokes shift is used, since it has a higher intensity than the anti-Stoke shift [66]. The measured Raman spectrum provides information about the structure, the bonding configuration and the chemical composition of the layer. In c-Si, the Raman spectrum is dominated by a transverse-optical peak at $520\,cm^{-1}$. In a-Si:H the spectrum is characterized by four peaks at $180\,cm^{-1}$, $330\,cm^{-1}$, $440\,cm^{-1}$ and $480\,cm^{-1}$, associated with the transverse acoustical, the longitudinal acoustical, the longitudinal optical and the transverse optical phonon modes, respectively, and two peaks at $2000\,cm^{-1}$ and $2100\,cm^{-1}$ associated with silicon-hydrogen stretching modes [67–69]. The stretching mode at $2000\,cm^{-1}$ is commonly known as the low stretching mode (LSM), while the one at $2100\,cm^{-1}$ is known as the high stretching mode (HSM).

Raman spectroscopy was performed on thin a-Si:H layers deposited on c-Si substrates. A typical measured Raman spectrum with the position of the various phonon and silicon-hydrogen stretching modes is shown in Figure 2.5 (a). The sample spectrum was deconvoluted by separately measuring a bare wafer and subtracting the sample spectrum from the spectrum of the bare wafer. Afterwards, Gaussian functions were used to fit the various modes. The Raman spectrum after the c-Si wafer subtraction, as well as the Gaussian functions and the end fitting result are shown in Figure 2.5 (b). The relative hydrogen content was obtained by comparing the ratio of the area of the transverse-optical peak at $480\,cm^{-1}$ to the area of the peaks associated with the silicon-hydrogen stretching modes, among the samples. This is further discussed in Chapter 4. Moreover,
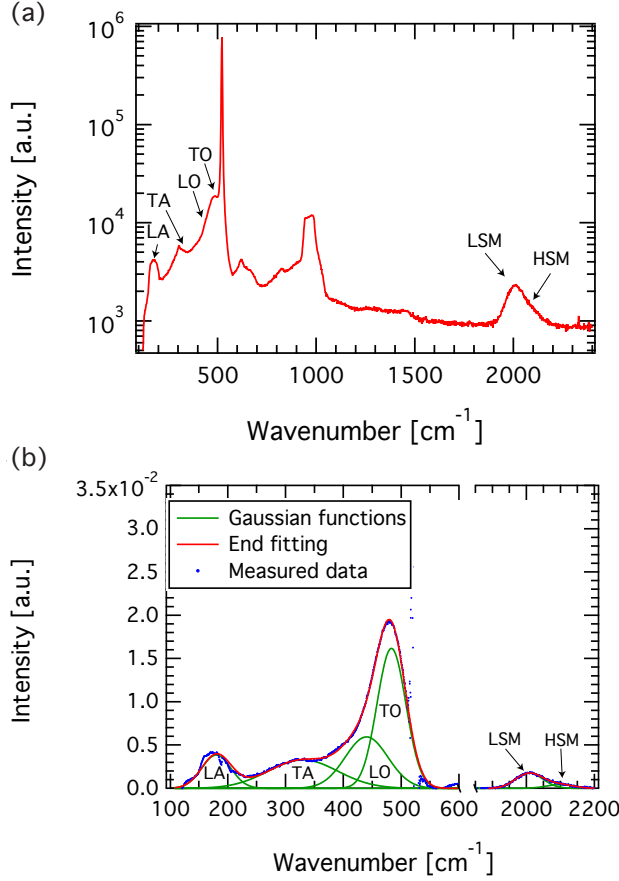
Figure 2.5: (a) Measured Raman spectrum of a thin hydrogenated amorphous silicon (a-Si:H) layer deposited on a crystalline silicon (c-Si) wafer. The positions of the relative phonon and stretching modes are indicated in the figure. (b) Measured Raman spectrum of a thin a-Si:H layer after the c-Si wafer subtraction (blue markers). Gaussian functions (shown with green lines) are used to fit the various phonon and stretching modes, which are indicated in the figure. The end fitting result is shown with the red line.

the ratio of the area of HSM to the total area of HSM and LSM was compared, as it can provide insight on the bonding configuration of the layer. The Raman spectrometer used in this thesis is an InVia Rama Microscope by Renishaw. For the excitation green light at 514 nm is produced by an Ar-ion laser.

2.2.6 Illuminated current-voltage measurements

Illuminated current-voltage measurements are performed in Chapters 3 and 5 to determine the external parameters (J_{SC}, V_{OC} and FF) of the SHJ devices. For this purpose the current of the cell is measured as a function of applied voltage when the cell is under illumination. The measurement is carried out at standard test conditions, which correspond to AM 1.5 solar spectrum ($1000\,\mathrm{W\,cm^{-2}}$) and $25\,^{\circ}\mathrm{C}$. To represent the AM 1.5 solar spectrum a halogen and a xenon lamp are combined. To control the temperature, a temperature controlled stage is used on which the solar cell is placed. The parasitic resistances introduced by the probes and contacts are eliminated by using a four-probe technique. A schematic of the current-voltage measurement setup is shown in Figure 2.6 In this work a AAA class Wacom WXS-156S-L2 solar simulator is used.
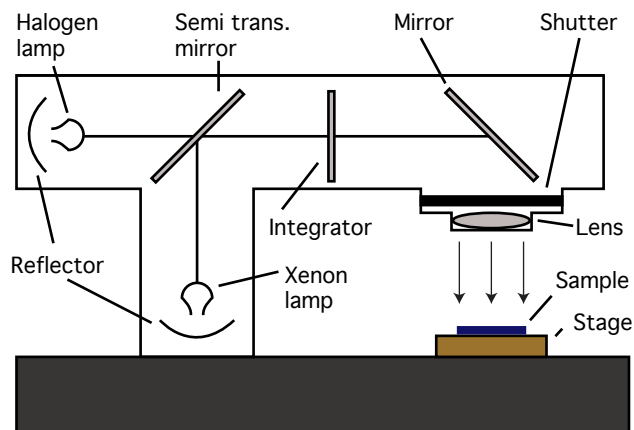
Figure 2.6: Illustration of the current-voltage measurement setup (based on [70]).

2.2.7 External quantum efficiency

Ideally, in a solar cell every photon with energy larger than the band gap of the absorber layer is absorbed and results in an electron-hole pair that is collected at the two terminals of the solar cell. In reality this is not the case and parasitic absorption, reflection and recombination losses reduce the ratio of the number of charge carriers collected successfully to the number of photons incident on the solar cell i.e. EQE of the solar cell. The EQE is

measured as a function of wavelength (λ) and gives an indication of the various optical and electrical losses in the solar cell as a function of λ. The EQE measurements are used in Chapters 3 and 5.

The EQE setup consists of a halogen lamp that emits a spectrum with a broad range of wavelengths, an optical chopper, a monochromator, a lock-in amplifier, a current meter, and a sample holder. Prior to the measurement the intensity at different wavelengths is calibrated with a silicon and a germanium diode for the short and long λ, respectively. Light emitted from the lamp is then chopped and enters the monochromator from where it is focused on the solar cell. A chopper is needed to obtain a periodic signal for the lock-in amplifier. Then the current is measured and converted to a voltage that serves as input for the lock-in amplifier. The amplified signal of the lock-in amplifier is finally read and displayed by a computer. A detailed description of the EQE principles can be found in [70].

From the EQE measurement, J_{SC} is determined using

$$J_{sc} = q \int_{\lambda_{min}}^{\lambda_{max}} EQE(\lambda)\Phi(\lambda)d\lambda, \tag{2.14}$$

where q is the elementary charge and $\Phi(\lambda)$ is the photon flux equal to

$$\Phi(\lambda) = P(\lambda)\frac{\lambda}{hc}. \tag{2.15}$$

In Equation (2.15) $P(\lambda)$ is the AM1.5 spectral power density, h is Planck's constant and c is the speed of light. The EQE measurements in this work are obtained by an in-house custom made setup.

3

Wet-chemical treatment for improved passivation of textured silicon heterojunction solar cells

Abstract

In this chapter a chemical treatment is demonstrated, which leads to an improved surface passivation when textured wafers are used in the fabrication of silicon heterojunction (SHJ) solar cells. SHJ solar cells constantly gain more attention due to their low cost and relatively high efficiency. An important aspect of these solar cells is the incorporation of intrinsic hydrogenated amorphous silicon (a-Si:H) layers at each side of the c-Si wafer, which has increased the efficiency potential due to the excellent surface passivation. By applying a randomly textured instead of a double-side polished wafer, optical enhancement is achieved resulting in significant reflection reduction and high short-circuit current densities (J_{SC}). However, texturing-induced defects lead to an a-Si:H/c-Si interface with increased recombination, which limits the open circuit voltage (V_{OC}) of the SHJ device after using the same cleaning treatment as for the flat wafer. Thus, a one-to-one transfer of process parameters from flat to textured c-Si substrate is not necessarily appropriate and a different wet-chemical treatment is needed.

3.1 Introduction

Silicon heterojunction (SHJ) solar cell technology is very promising for the future compared to other photovoltaic technologies, due to the high conversion efficiencies achieved and the low processing thermal budget [71]. For both conventional SHJ solar cells and interdigitated back contact (IBC) solar cells the use of textured wafer substrates is a requirement in order to enhance light trapping and achieve high J_{SC} after device fabrication. At the moment of writing this thesis, the SHJ solar cell reached an efficiency of 26.6 % on a practical area of 180 cm^2 [18, 19]. To achieve such high efficiencies, a textured substrate is typically used. At the same time the use of textured substrates can lead to devices with poor interface quality of the amorphous/crystalline silicon (a-Si:H/c-Si) junction. The high surface defect densities at this interface can significantly increase the recombination losses and therefore limit the V_{OC}.

In order to reduce the interface defect density an efficient pre-deposition treatment is required to remove any possible contamination and nano-roughness from the c-Si substrate [72–74]. The term nano-roughness refers to structural irregularities on the c-Si surface induced from texturing. It has been shown that any possible contamination can be completely removed after applying a wet-chemical oxidation step and a subsequent dip in hydrofluoric acid (HF) [75]. In this case the surface defect density will strongly depend on the nano-roughness of the surface [75, 76]. Therefore, a non-aggressive pre-treatment that can remove any possible contamination and minimize surface roughness becomes necessary.

In this work, widely used wet-chemical cleaning procedures have been applied on textured c-Si substrates. In addition, an approach of subsequent oxidation and removal steps of the oxide has been tested. The oxidation has been realized by immersion of the c-Si substrate in nitric acid (HNO$_3$) solutions. In this way an approach similar to the nitric acid oxidation of silicon (NAOS) method [77] has been used, followed by stripping of the silicon oxide layer using an HF solution. In this work we will refer to this treatment as nitric acid oxidation cycle (NAOC). Repeating NAOC, i.e. oxidation and stripping of the oxide, is expected to help remove any surface structural irregularities in a controlled way. After the treatment the samples were subsequently passivated with intrinsic a-Si:H with a thickness of approximately 40 nm and the effectiveness of the pre-treatment in removing textured-induced defects has been evaluated using photoconductance decay measurements [52]. The NAOC treatment has been sub-

sequently applied to fabricate a device structure. Finally, SHJ solar cells were fabricated.

3.2 Experimental details

For the investigation of the pre-deposition cleaning procedures n-type FZ c-Si <100> wafers, with resistivity 1–5 Ω cm and thickness of $280 \pm 20\,\mu m$ were textured in an etching mixture consisting of high purity deionized water (DIW) and commercial solutions of 25 % tetramethyl ammonium hydroxide (TMAH) and 99.9 % isopropyl alcohol (IPA). The RCA, Piranha, and Nitric Acid Oxidation Cycle (NAOC) cleaning treatments, as well as combinations of those, were applied to the samples. RCA consists of two standard cleaning (SC) steps, SC-1 and SC-2. SC-1 and SC-2 steps were performed with a 1:1:5 solution of ammonium hydroxide (NH_4OH), hydrogen peroxide (H_2O_2), DIW, and a 1:1:6 solution of hydrochloric acid (HCl), H_2O_2, DIW, respectively at 80 °C for 10 min each. As an intermediate step between SC-1 and SC-2, wafers were dipped in 0.55 % HF at room temperature (RT) in order to remove the oxide layer grown previously in SC-1. SC-1 and SC-2 were prepared by mixing commercial solutions of 35 % NH_4OH, 30 % H_2O_2 and 37 % HCl. Piranha treatment was realized in a 1:3 solution of concentrated sulfuric acid (H_2SO_4) and 30 % H_2O_2 at approximately 120 °C for 20 min. Finally, NAOC consists of a 10 min step in concentrated HNO_3 at RT, a second 10 min step in 69.5 % HNO_3 at 105 ± 5 °C and stripping of silicon oxide layer in HF. Using spectroscopic ellipsometry, on a <100> polished substrate, the silicon oxide layer due to the immersion in HNO_3 was found to be 1–2 nm. Every treatment step was followed by rinsing the textured substrate in DIW. Last step of every process before a-Si:H deposition was the H-termination of the Si surface in 0.55 % HF at RT.

The treatment of the wafers was followed by the growth of intrinsic a-Si:H layers using radio-frequency plasma-enhanced chemical vapor deposition (RF-PECVD). The excitation frequency was 13.6 MHz. The a-Si:H layer were grown on both sides of the wafer and the thickness was chosen to be approximately 40 nm. The reason for using thicker layers than what is commonly used in SHJ devices (5–10 nm), is to avoid effects in the measured effective lifetime (τ_{eff}) due to insufficient thickness of the passivation layer. Ultrathin intrinsic a-Si:H layers, unprotected by the doped (p- and n-type) a-Si:H layer could be unstable when exposed to air and

therefore are less favorable to use in investigating the effect of the cleaning procedure. For the device structures approximately 5 nm thick intrinsic a-Si:H layers were used. The p- and n-type doped layers have a thickness of approximately 5 nm and 9 nm, respectively. Finally, in the solar cell devices the thickness of the intrinsic and p-type doped layers is approximately 6 nm, while the n-type dope layers have a thickness of approximately 9 nm. The effect of the cleaning treatments was investigated by measuring τ_{eff} of the stacks using a Sinton Consulting WTC-120 lifetime tester in transient mode [52].

3.3 Results and discussion

3.3.1 Texturing process using tetramethyl ammonium hydroxide

The textured surfaces were obtained by anisotropic etching of the c-Si wafers in a low concentration TMAH and IPA solution. Typically, for etching of c-Si KOH and NaOH are used as etchants, as they are more mature and cost-efficient technologies [78–83]. However, in this work TMAH was preferred due to the main advantage it has, which is the absence of ionic contaminants i.e. K^+ and Na^+ [80, 84]. According to Iencinella et al. [85] the main drawback of using TMAH is the high cost involved but as far as it is used in low concentrations and the same solution can be re-used to texture multiple wafers, etching with TMAH can remain cost-competitive.

Texturing aims to obtain a fully covered c-Si pyramidal surface with atomically smooth facets and to achieve at the same time low reflectance. Iencinella et al. [85] used TMAH solution for texturing and obtained light trapping with reflectance lower than 15 % (in the wavelength range (500–1100 nm)) and uniform texture on the whole wafer surface. Rosa et al. [86] also used TMAH for texturing and obtained c-Si wafers that showed approximately 10 % reflectance at 600 nm.

In this work the c-Si wafer were textured in low concentration TMAH and IPA solution. The addition of IPA in the solution is essential for obtaining satisfactory smoothness on the pyramidal surface of the c-Si wafer [81, 87]. When low concentration TMAH is used IPA reduces the etching rate of the solution. In turn lower etching rates have been associated with better morphologies [81]. This can be understood by some of the basic processes that take place in the aqueous TMAH solution. It is assumed that hydroxide ions (OH^-), water (H_2O), tetramethylammonium ions (TMA^+)

and the IPA particles coexist in the solution and interact with the c-Si surface by adsorption or desorption. According to Zubel and Kramkowska [81] TMA$^+$ ions and IPA particles have an important effect in the etching behavior. Although the polar OH$^-$ ions are the most likely to absorb to the silicon surface, adsorption of TMA$^+$ ions and IPA particles also takes place. The adsoption of big and massive ions and particles (i.e. TMA$^+$ and IPA) restricts the access of OH$^-$, which is responsible for the silicon oxidation process. Therefore increasing the TMAH or IPA concentration effectively will limit the rate of the etching process by reducing the silicon oxidation rate. Theoretically, the best morphology can be achieved when an equilibrium is reached between the oxidation rate and the desorption of the reaction products. According to Palik et al. [88] the primary reaction product is $SiO_2(OH)_2^{2-}$. For example, if the desorption process runs slower than the silicon oxidation, the remaining species on the silicon surface will disturb the OH$^-$ from reaching the surface and in effect the surface will become roughened.

The surface morphology and the corresponding reflectance of the textured c-Si wafers for different etching times, can be seen in Figure 3.1 (a)-(g). It is shown that after 45 min of texturing there are still some flat regions on the surface of the c-Si wafer (Figure 3.1 (d)) while full coverage with pyramids is achieved after 60 min. Further texturing does not result in distinguishable changes in the surface morphology. After 60 min the c-Si surface is fully covered with pyramids that have facets with <111> orientation. It is known that such etching solutions have a significantly lower etching rate of the plane with <111> crystal orientation [78, 84, 89, 90]. The reflectance of these samples can be seen in Figure 3.1 (h). Figure 3.1 (h) shows that the reflectance in the range 500–1100 nm significantly decreases in the first 45 min from an average reflectance of approximately 35 % to approximately 10 %. All the samples presented in this work were textured for 60 min in order to achieve full coverage of the c-Si surface with pyramids and reflectance of about 10 %.

3.3.2 Evaluation of the pre-deposition treatment in wafers passivated with intrinsic a-Si:H

The cleaning treatments investigated in this work are the RCA, the piranha and the oxidation of c-Si with HNO_3 followed by oxide removal (i.e. NAOC). These treatments, as well as a combination of them were applied on the wafer textured in the TMAH and IPA solution. Subsequently
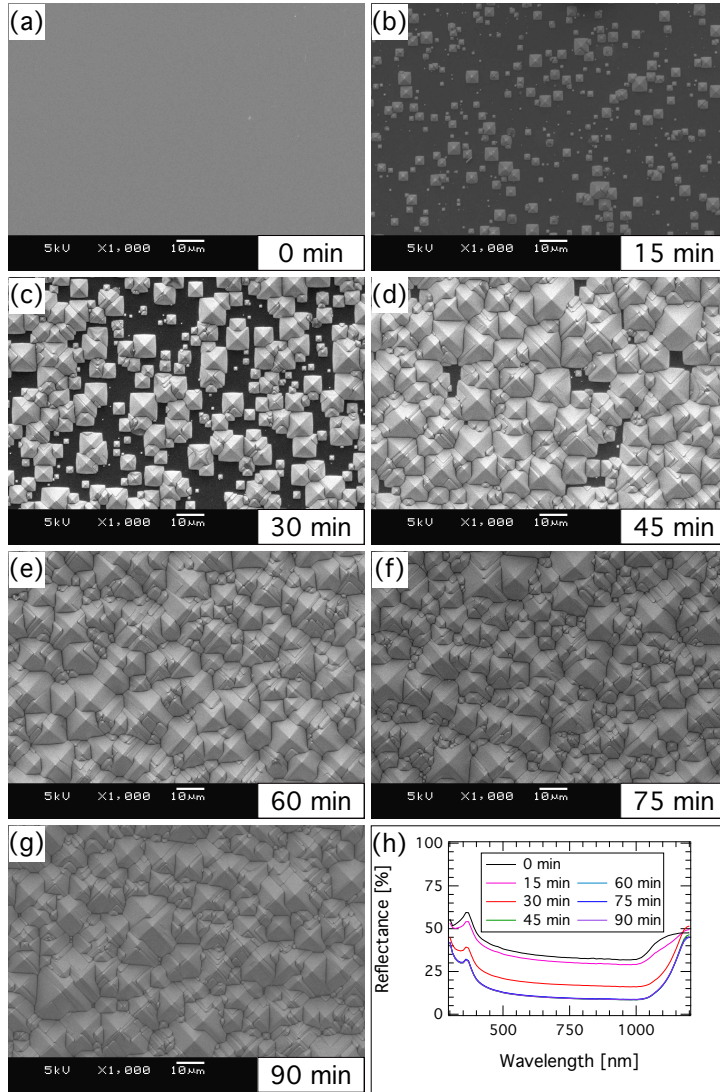
Figure 3.1: Scanning electron microscopy images of the crystalline silicon (c-Si) wafer surface (a) before texturing (0 min) and after texturing in a tetramethyl ammonium hydroxide and isopropyl alcohol solution for (b) 15 min, (c) 30 min, (d) 45 min, (e) 60 min, (f) 75 min and (g) 90 min. (h) Measured reflectance as a function of wavelength for different texturing times of the c-Si wafer.

the wafers were symmetrically passivated with intrinsic a-Si:H in an RF-PECVD reactor and τ_{eff} was measured.

Figure 3.2: Effective lifetime (τ_{eff}) of crystalline silicon (c-Si) wafers passivated with a thin layer of hydrogenated amorphous silicon, for different cleaning treatments applied on the c-Si wafer. The measured τ_{eff} is at injection level 1×10^{15} cm^{-3}. Green markers are used for polished c-Si substrates, while blue and red markers are used for textured substrates. NAOC treatment is indicated with 'x'(number of repeated cycles).

The resulting τ_{eff} for the various treatments applied in this work is shown in Figure 3.2 (shown with blue markers). It can be seen that the lowest τ_{eff} is obtained when the c-Si wafer is cleaned with the piranha solution. Although sulfur contamination during the cleaning cannot be excluded, the low τ_{eff} observed can be attributed to nano-roughness on the surface of the wafer caused by the decomposition of H_2O_2 [91]. For this reason, we see that when the NAOC cleaning is applied after the piranha treatment (Pir.+x(1) in Figure 3.2), τ_{eff} increases. It is possible that the NAOC cleaning is able to remove some of the damage on the surface of the c-Si wafer, caused by the piranha cleaning. In a similar way, although the RCA results in a higher τ_{eff}, as compared to the piranha, an improvement is observed when the RCA is followed by the NAOC treatment. The high contamination removal efficiency of RCA is mainly associated with the continuous oxidation and oxide removal by H_2O_2 and NH_4OH agents respectively in

SC-1. Therefore, also in this case a limitation of τ_{eff} can be associated with nano-roughness on the surface of the c-Si wafer, originating from H_2O_2 decomposition. When the NAOC treatment is used for cleaning, one cycle seems to be able to yield similar τ_{eff} with the RCA. However, repeating the experiment for two and three NAOC cycles (x(2) and x(3) shown with blue markers in Figure 3.2) shows the best τ_{eff}.

The fact that all treatments should be able to remove any possible contamination indicates that the differences observed in τ_{eff} are due to the change in nano-roughness on the facets of the pyramidal surface of the wafer. Interestingly, more than three NAOC cycles resulted in a decrease of τ_{eff}. It was expected that after reaching an optimum, every step of oxidation and removal of the oxide would result in similar roughness and therefore similar τ_{eff}. A second series of samples in which the NAOC treatment has been applied can be seen in Figure 3.2 (shown with red markers) and is compared with τ_{eff} obtained for the polished samples (shown with green markers). In this case, τ_{eff} for a polished substrate cleaned with one NAOC cycle serves a reference. It is shown in Figure 3.2 that τ_{eff} obtained with three NAOC cleaning on a textured c-Si wafer is comparable to τ_{eff} obtained on flat double side polished substrate. The effect of the subsequent NAOC cleaning has been also tested by applying two NAOC cycles on a polished substrate. In this case only a slight decrease is observed in τ_{eff}. In both series, an improvement is observed when repeating the NAOC treatment cycles, reaching an optimum at three cycles and slightly decreasing for more cycles.

After the cleaning procedure and the intrinsic a-Si:H deposition all samples were annealed at 170 °C for 1 h in ambient air. It has been shown that post-deposition low temperature annealing can reveal information regarding the quality of the interface [92]. Annealing is expected to improve passivation by film relaxation when the transition from c-Si substrate to the a-Si:H layer is abrupt. In case an epitaxial layer is grown, annealing can even be detrimental for the passivation [92].

The relative change in τ_{eff} for all the samples is shown in Figure 3.3. Interestingly, only samples cleaned by the NAOC treatment exhibit a significant increase in τ_{eff} compared to the other treatments, similarly to the polished samples. We argue that this is related to the efficient removal of the nano-roughness through the subsequent steps of oxidation and oxide removal. Initial roughness on the surface of the c-Si substrate might effectively result in similar interface properties as in the case of an epitaxial grown layer. However, this is expected to be strongly dependent on the

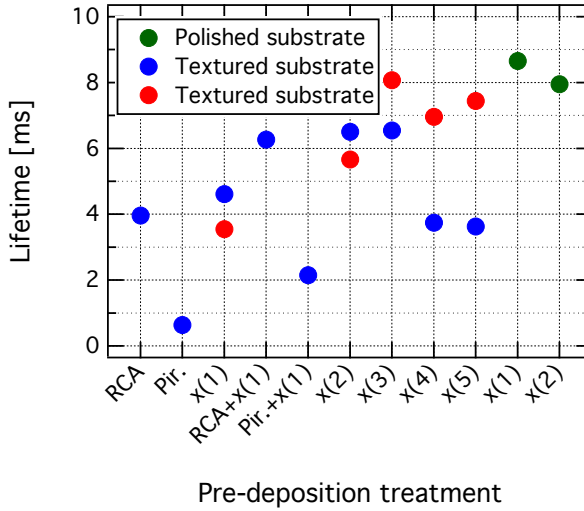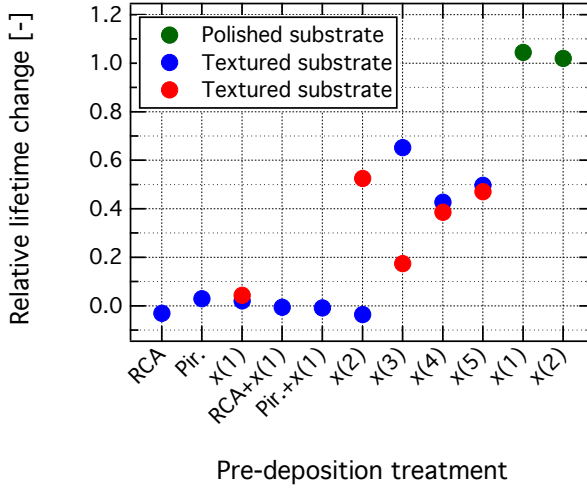**Figure 3.3:** Relative change in the effective lifetime (τ_{eff}) of crystalline silicon (c-Si) wafers passivated with a thin layer of hydrogenated amorphous silicon, for different cleaning treatments applied on the c-Si wafer. The measured τ_{eff} is at injection level $1 \times 10^{15}\,\text{cm}^{-3}$. Green markers are used for polished c-Si, while blue and red markers are used for textured substrates. NAOC treatment is indicated with 'x'(number of repeated cycles).

initial morphology of the substrate after the texturing, as well as the deposition conditions for the a-Si:H layers. For the sample clean with the two NAOC cycles, from the first series, we observed no change during annealing, however, τ_{eff} measured after deposition had already a value comparable to τ_{eff} obtained for the polished substrates.

3.3.3 Evaluation of the pre-treatments in device structure

The cleaning treatment that yielded the best results, i.e. NAOC, was also applied to fabricate devices and measure τ_{eff}. The devices have the following structure: p a-Si:H/i a-Si:H/c-Si/i a-Si:H/n a-Si:H. In Figure 3.4 (a), τ_{eff} is shown for different number of NAOC cleaning cycles on textured substrate (red markers) and compared to τ_{eff} obtained using one NAOC cycle on a polished substrate (green marker). Also in this case an optimum in τ_{eff} is observed when 3 NAOC cycles are used, while τ_{eff} decreases for more cycles. The optimum τ_{eff} for 3 NAOC cycles is very similar to τ_{eff} obtained for a device fabricated on a polished substrate. This shows that by
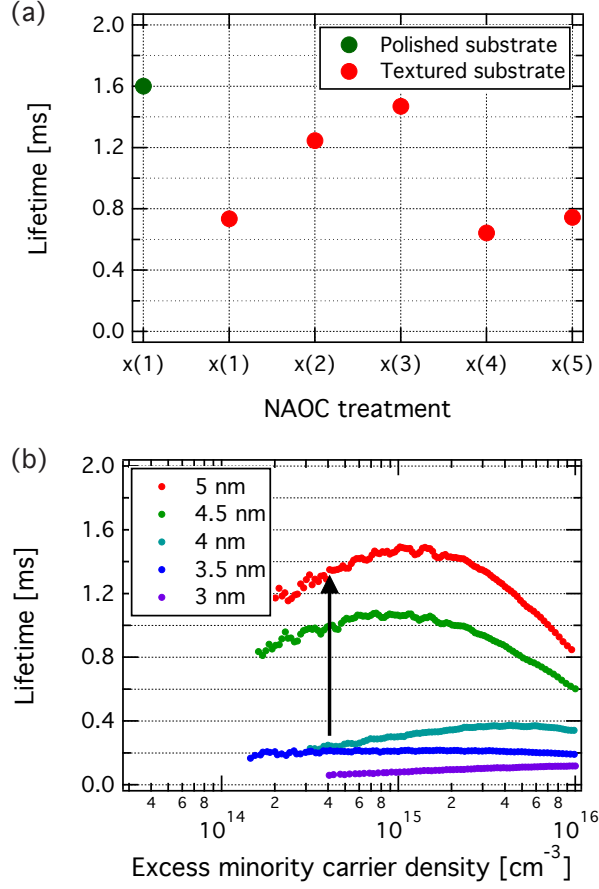
Figure 3.4: (a) The effective lifetime (τ_{eff}) measured for device structure deposited on polished (green marker) and textured substrates (red markers) at injection level $1 \times 10^{15}\,\mathrm{cm}^{-3}$. (b) τ_{eff} as a function of the minority carrier injection level for different estimated thicknesses of the intrinsic hydrogenated amorphous silicon passivation layer.

applying subsequent NAOC cycles the damage induced by the texturing can be efficiently removed. However, in this case much shorter τ_{eff}s are measured for all samples as compared to Figure 3.2, limited by the presence of the p-type doped layer and the thickness of the intrinsic a-Si:H passivation layers.

The thickness of the intrinsic a-Si:H passivation layer is another important parameter that can influence τ_{eff}. Especially, when passivation layers

(a)

(b)
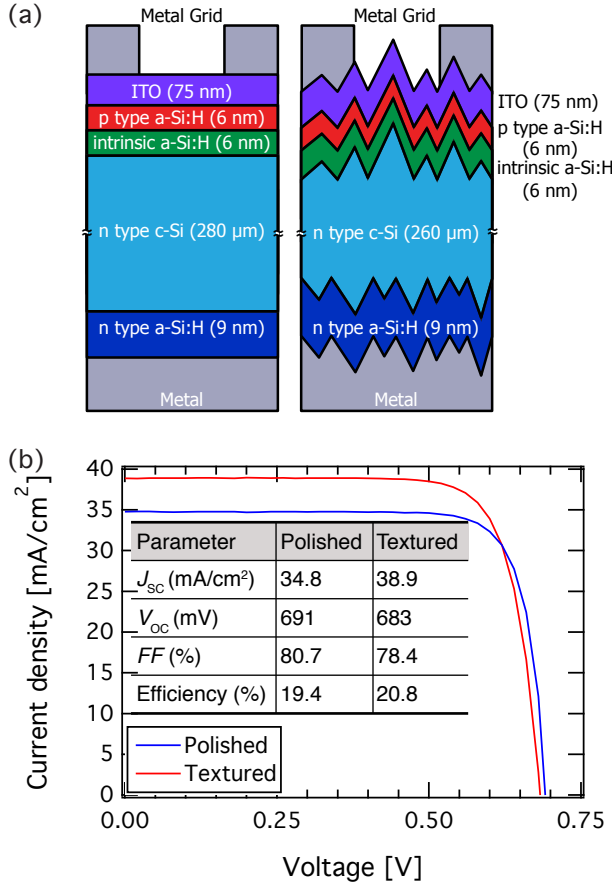
Figure 3.5: (a) Schematic of the silicon heterojunction (SHJ) device structure on polished and textured substrate. (b) Illuminated current density as a function of voltage for SHJ solar cells on polished and textured substrate. The values for the short circuit current density (J_{SC}), the open circuit voltage (V_{OC}), the fill factor (FF) and the efficiency, are given in the inset table. The values of J_{SC} presented here refer to the active area of the solar cell. The pre-treatment used is one and three NAOC cycles for the polished and the textured substrate, respectively.

of a few nm are used, as in the device structure. The effect of the passivation layer thickness in τ_{eff} for the device structure on texture substrates is shown in Figure 3.4 (b). In Figure 3.4 (b) to estimate the passivation layer thicknesses, the a-Si:H deposition rate was estimated on a polished

substrate and was divided by a factor of 1.73 to account for the pyramidal surface [93]. For passivation layer thinner than 4 nm, significantly lower τ_{eff} are observed. We think that these extremely low values of τ_{eff} are related with the insufficient coverage of the substrate surface. This can be enhanced by any roughness on the facet of the pyramidal structures that will shade the substrate during the deposition and result in non-conformal passivation layers.

3.3.4 Performance of silicon heterojunction solar cells

Finally, complete SHJ solar cell devices with an area of $4\,\mathrm{cm}^2$ were fabricated independently on a polished and textured substrate. The structure of the devices and the thickness the each layer is shown in Figure 3.5 (a). The performance of the devices is summarized together with the illuminated current-voltage characteristics in Figure 3.5 (b). For these SHJ solar cells the intrinsic layer at the back has been omitted. The reason for this omitting is that τ_{eff} is mainly limited by the front interface and at the same time an improvement in the *FF* is observed [94]. For the polished and textured devices one and three NAOC are used, respectively, as these treatments proved to result in the best passivation for each case. Although, the device on a polished substrate has slightly higher Voc and *FF* the textured device has much higher current density due to the effective light trapping resulting in an active-area efficiency of 20.8 %. To obtain the active-area efficiency, the short circuit current density was used, as calculated from external quantum efficiency measurements.

3.4 Conclusion

In this chapter, the effectiveness of commonly used cleaning procedures for the conditioning of textured c-Si substrates has been investigated. Moreover, an approach of wet-chemical oxidation using HNO_3 and subsequent removal has been applied. The cleaning procedure after the texturing is an important step to achieve high open circuit voltage and therefore high efficiency SHJ solar cells. However, the cleaning can also introduce roughness depending on the chemical solution used. For our textured samples, repeated cycles of nitric acid oxidation and oxide removal are able to improve the passivation quality significantly. It is expected that this improvement is directly related to the efficient removal of contamination

and nano-scaled roughness, induced from the texturing, on the facets of the pyramidal structures. By varying the thickness of the intrinsic a-Si:H passivation layer it is observed that τ_{eff} significantly decreases when the passivation layer becomes thinner than 4 nm. This is attributed to inhomogeneous coverage of the c-Si surface during growth and suggests that the morphology is an important parameter that can affect τ_{eff} when such thin passivation layers are used.

4

Surface passivation of crystalline silicon for silicon heterojunction solar cells using high-pressure hydrogen diluted plasmas

Abstract

In this chapter we demonstrate excellent crystalline silicon surface passivation by depositing hydrogenated amorphous silicon in the high-pressure and high hydrogen dilution regime. By using high hydrogen dilution of the precursor gases during deposition the hydrogen content of the layers is sufficiently increased, while the void fraction is reduced, resulting in dense material. Results show a strong dependence of the effective lifetime on the substrate temperature and a weaker dependence on the hydrogen dilution. After applying a post-deposition annealing step on the samples equilibration of the effective lifetime occurs independent of the initial nanostructure.

4.1 Introduction

Improving surface passivation is an important aspect for so-called silicon heterojunction (SHJ) solar cells. This solar-cell technology, has been able to achieve a V_{OC}, as high as 750 mV and efficiency of up to 26.6 %, when it is used in a back contacted configuration [18, 19, 31, 95–97]. One of the key points in the device performance is the incorporation of thin intrinsic hydrogenated amorphous silicon (a-Si:H) layers on both sides of the crystalline silicon (c-Si) substrate. It has been shown that the quality of these layers affects the external parameters of the device [98–100], therefore, the fabrication process and the properties of the a-Si:H layers have a great impact on the efficiency of the SHJ solar cell.

Passivation of c-Si with intrinsic a-Si:H is predominantly associated with reduction of the density of unsaturated bonds or defects, which act as recombination centers. These defects can be found in the bulk of the a-Si:H layer, at the a-Si:H/c-Si interface, and/or in the sub-surface region of the c-Si substrate. Typically passivating a-Si:H layers are deposited using radio-frequency plasma-enhanced chemical vapor deposition (RF-PECVD) [101, 102]. The pre-deposition processes, i.e. texturing and cleaning, can affect defect creation in the c-Si sub-surface region. However, the deposition conditions for the a-Si:H layer will determine the defect creation in all three regions and therefore the final passivation quality. The defects at the a-Si:H/c-Si interface [103] and in the c-Si sub-surface region can be induced by the plasma or by initial epitaxial growth of the layer [104, 105], whereas defects in the bulk of the a-Si:H are grown naturally. At the same time the deposition conditions determine the hydrogen content of the layer [106].

A simplified illustration of a-Si:H grown on c-Si is shown in Figure 4.1. In Figure 4.1 the various regions are indicated and the formation of defects in these regions is illustrated. It has been shown that hydrogen is essential for the passivation, [107] as is reflected in the V_{OC} of SHJ devices [108]. For this purpose hydrogen plasma treatments during [109] and post-deposition [110, 111] have been proposed, achieving state-of-the-art passivation. In both cases hydrogen incorporation led to a significant improvement in passivation, while attempts to apply pre-deposition hydrogen treatment on the substrate resulted in the creation of defects on the c-Si surface and proved detrimental for the passivation [112]. At the same time it has been shown that such attempts to increase the hydrogen content and improve the passivation quality can significantly alter the
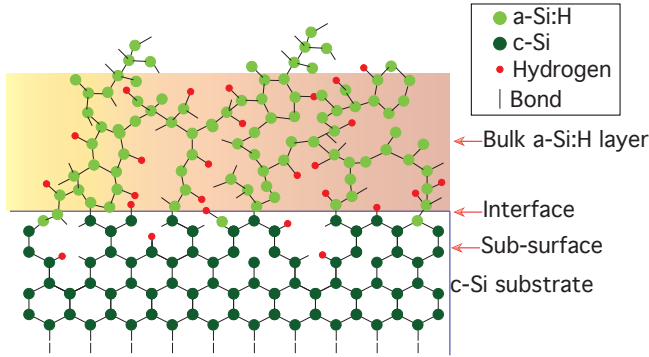
Figure 4.1: Illustration of hydrogenated amorphous silicon (a-Si:H) layer grown on crystalline silicon (c-Si) wafer. The bulk a-Si:H region, the interface between a-Si:H and c-Si and the sub-surface region of the c-Si wafer are indicated.

nanostructure of a-Si:H leading to void-rich material and in some cases cause irreversible damage at the interface [113].

In this work we demonstrate PECVD conditions using high hydrogen dilution (200 sccm H_2 compared to 2.5–10 sccm SiH_4), low power density (0.05 W cm^{-2}), and relatively high deposition pressure (8 mbar) [114] that result in material close to the a-Si:H-to-c-Si:H transition regime, passivating c-Si and achieving τ_{eff} >10 ms. As a result of the low power density and high deposition pressure the ion bombardment energy is decreased, [115] thereby minimizing possible damage on and just below the surface of the c-Si substrate while shifting the a-Si:H-to-c-Si:H transition to higher dilutions and allowing to deposit amorphous silicon at extremely high dilution conditions. We show how the τ_{eff} correlates to changes in the nanostructure of the material, which in turn is varied by changing the hydrogen dilution and substrate temperature. In this way we shed light on the nature of the defect reduction and passivation mechanism. Information on the hydrogen content and bonding configuration in our samples we obtain by an analyses approach using Raman spectroscopy measurements. In this work we study the nature of the defect reduction passivation mechanism using a-Si:H passivating layers processed at high-pressure and high hydrogen dilution ratios.

4.2 Experimental details

For the experiments, stacks consisting of a wafer passivated on both sides with intrinsic a-Si:H were fabricated, using <111> n-type Si float zone wafers with a thickness of $280 \pm 20\,\mu m$ and resistivity of $3 \pm 2\,\Omega\,cm$. The wafers were cleaned in HNO_3 99 %, subsequently dipped in HNO_3 69.5 % at $105 \pm 5\,°C$ and followed by an HF 0.55 % step in order to strip the silicon oxide layer. In between the steps and after the H termination the substrates were immersed in deionized water. The a-Si:H layers were deposited using a RF-PECVD reactor with an excitation frequency of 13.56 MHz. During deposition the power density, for all the layers, was $0.05\,W\,cm^{-2}$ and the pressure was set to 8 mbar. After deposition samples were annealed in ambient conditions. For the characterization of the stacks the τ_{eff} was measured using a Sinton Consulting WTC-120 lifetime tester in transient mode [52]. The optical bandgap (E_{04}) and the thickness of the layers were determined by means of Spectroscopic Ellipsometry (SE), using the Cody - Lorentz model [55], which was found to give more accurate fittings than the commonly used Tauc-Lorentz model [56]. For all the layers the thickness of the a-Si:H layers was determined to be $31 \pm 3\,nm$. The effect of H_2 dilution and substrate temperature on the τ_{eff} was investigated by means of SE and Raman spectroscopy.

4.3 Results and discussion

We analyzed Raman spectra in an innovative way to compare both the hydrogen content and the nanostructure of $31 \pm 3\,nm$ a-Si:H layers deposited on c-Si wafers using different conditions. Raman spectroscopy has been used before to determine the hydrogen content in an absolute way by comparing with infrared spectra and experimentally estimating the scattering cross sections [69], but in this work we determine the hydrogen content in a relative way. For this analysis the a-Si:H contribution to the Raman intensity signal is de-convoluted from the crystalline silicon absorption peak by subtracting the background signal of a bare wafer. For all samples a frequency shift of $0.4 \pm 0.4\,cm^{-1}$ of the background signal is necessary before the subtraction to match the signal of the c-Si wafer. This frequency shift is associated with stress differences in the samples [116]. The a-Si:H residue is then fitted with four Gaussian peaks at 180, 330, 440 and 480 cm^{-1} representing the acoustic and optical phonon modes that

contribute to the a-Si:H Raman signal [57, 67].

Figure 4.2 (a) and (b) show an example of a Raman measurement after subtraction of the background signal, including the different Gaussian peaks used in the fitting process, and the end-fitting result. It can be seen that, although some noise is present around $510\,\mathrm{cm}^{-1}$ after the background subtraction, a good matching is obtained between the experimental data and the fitting. This measurement allows us to have a relative estimation of the hydrogen content in the different samples using

$$\frac{A_{\text{Si-H}}}{A_{\text{Si-Si}}} = \frac{\sigma_{\text{Si-H}}}{\sigma_{\text{Si-Si}}}\frac{[\text{H}]}{[\text{Si}]}, \tag{4.1}$$

with [H] as the hydrogen content and [Si] as the silicon content.

In Equation (4.1), $A_{\text{Si-H}}$ is the total peak area of the low stretching mode (LSM) at approximately $2000\,\mathrm{cm}^{-1}$ and the high stretching mode (HSM) at $2100\,\mathrm{cm}^{-1}$ (i.e., $A_{\text{Si-H}} = A_{\text{HSM}} + A_{\text{LSM}}$), $A_{\text{Si-Si}}$ is the area of the transverse optical (TO) mode located at approximately $480\,\mathrm{cm}^{-1}$. In Equation Equation (4.1) $\sigma_{\text{Si-H}}$ and $\sigma_{\text{Si-Si}}$ are the Raman scattering cross sections related to Si-H and Si-Si bonds, respectively. In addition it is assumed that $\sigma_{\text{Si-H}}$ and $\sigma_{\text{Si-Si}}$ are similar between the different samples. It is therefore expected that comparing the peak area ratio at the frequency position associated with Si-H and Si-Si bonds [57] will provide information about the hydrogen content of the thin a-Si:H layers. Moreover, the $A_{\text{HSM}}/(A_{\text{HSM}} + A_{\text{LSM}})$ ratio of the different samples is calculated. This ratio provides information about the hydrogen bonding environment, i.e. A_{LSM} related to monohydrides and A_{HSM} related to clustered monohydrides in nano-sized voids or dihydrides [117]. Essentially, this ratio is similar, but not necessarily equal to the microstructure parameter R* typically obtained from Fourier-transform infrared spectroscopy measurements. For all samples the peak position for HSM is fixed at $2100\,\mathrm{cm}^{-1}$ and the peak position for the transverse acoustic, longitudinal acoustic and transverse optical phonon modes is fixed at $180, 330, 440\,\mathrm{cm}^{-1}$, respectively, during the fitting procedure.

This Raman analysis is used to study the differences in the nanostructure of the thin a-Si:H films deposited on top of the c-Si wafers. Figure 4.3 (a) shows the deposition rate and the optical bandgap as a function of the H_2-to-SiH_4 ($[H_2]/[SiH_4]$) flow ratio. The deposition rate decreases with $[H_2]/[SiH_4]$ flow ratio as expected. The variation of the flow ratio is achieved by changing the SiH_4 flow, whilst keeping the H_2 flow constant at 200 sccm. Because of the strong H_2 dilution in the plasma these variations cause negligible changes in the total flow. These changes are
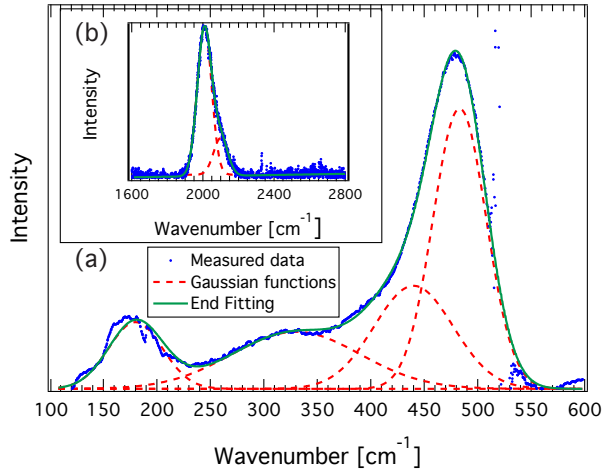
Figure 4.2: A fitting example of Raman data. (a) The experimental data (blue markers) is fitted with 4 Gaussian peaks (red dashed line) in the range 100–570 cm^{-1} and (b) the experimental data (blue markers) is fitted with 2 Gaussian peaks (red dashed line) in the range 1600–2800 cm^{-1}. The end result is shown with the green solid line.

sufficient to decrease the active species associated with the growth of the layer and reduce the deposition rate. At the same time the optical bandgap increases with the $[H_2]/[SiH_4]$ flow ratio. It has been reported before that the optical bandgap of a-Si:H materials increases with H content in the bulk [118, 119]. However, Figure 4.3 (b) shows that the H concentration as obtained from Raman spectroscopy does not increase significantly with $[H_2]/[SiH_4]$ flow ratio, while at the same time an increase is observed in the HSM associated with nano-sized voids. Therefore, the increase of the bandgap with $[H_2]/[SiH_4]$ is expected to be due to nanostructural changes in the anisotropic silicon matrix [120]. The error bars in Figure 4.3 (b) represent the standard deviation, determined from the Raman data fitting shown in Figure 4.2 (a) and (b). The τ_{eff} for all the stacks can be seen in Figure 4.3 (c). This figure shows that the variation in τ_{eff} is limited as a function of hydrogen dilution, with the τ_{eff} being slightly lower for $[H_2]/[SiH_4]$ = 20.

After deposition the stacks were annealed at 240 °C for 240 min. It has been shown that post-deposition annealing can provide information about the abruptness of the interface [92, 121]. When epitaxial growth has oc-

curred at the a-Si:H/c-Si interface annealing at this temperature reduces the τ_{eff}, while in presence of an abrupt transition at the a-Si:H/c-Si interface annealing increases the τ_{eff} [92]. On the other hand, this temperature is well below the hydrogen effusion temperature which is expected to be at ∼300 °C [122]. For all samples an increase in τ_{eff} is observed upon annealing, pointing towards an epitaxy-free interface.

The nanostructure and the hydrogen content in a-Si:H can also be altered significantly by changing the substrate temperature during growth [123–125]. Figure 4.4 (a) shows the deposition rate and optical bandgap for different substrate temperatures at a dilution of $[H_2]/[SiH_4]$ = 50. Although some authors have shown that for T < 240 °C the deposition rate should be almost independent of temperature [126, 127], we find that this is not the case. We think that this is associated to the temperature dependence of the etching effect when high H_2 diluted plasmas are used during the growth [128]. The effective deposition rate is a competition between the growth due to radicals and ions sticking to the surface, and the hydrogen induced etching of the material. At higher temperatures the etching is quenched, resulting in higher effective deposition rate.

In Figure 4.4 (a) it can also be seen that the optical bandgap is decreasing with temperature. The refractive index, as determined from SE at 2 eV (not shown here), increases from 4.11 (at 100 °C) to 4.31 (at 280 °C) indicating an increase in material density with deposition temperature. At the same time, the hydrogen content of the layers is decreasing, as is concluded from the decreasing $A_{\text{Si-H}}/A_{\text{Si-Si}}$ ratio shown in Figure 4.4 (b). The decrease in hydrogen content is accompanied by a decreased contribution of the HSM, associated to a void-rich a-Si:H matrix. In Figure 4.4 (b) the error bars represent the standard deviation, determined from the Raman data fitting shown in Figure 4.2 (a) and (b).

The as-deposited and post-annealed τ_{eff} can be seen in Figure 4.4 (c). This τ_{eff} first increases with a factor of 1000 with increasing T_{dep}, showing a maximum, and then decreases for high T_{dep}. Interestingly, the as-deposited τ_{eff} follows a similar trend reported previously for the bulk a-Si:H defect density determined using Electron Spin Resonance measurements [127]. However, the trend for the defect density reported by Matsuda et al. is reversed compared to that of the τ_{eff} shown here, as the τ_{eff} and defect density are correlated via an inverse relationship. The high defect density or low τ_{eff} at T_{dep} < 180 °C is attributed to the slow diffusion of the species on the growing surface and therefore not efficient annihilation of dangling bonds at the interface during deposition. At the same
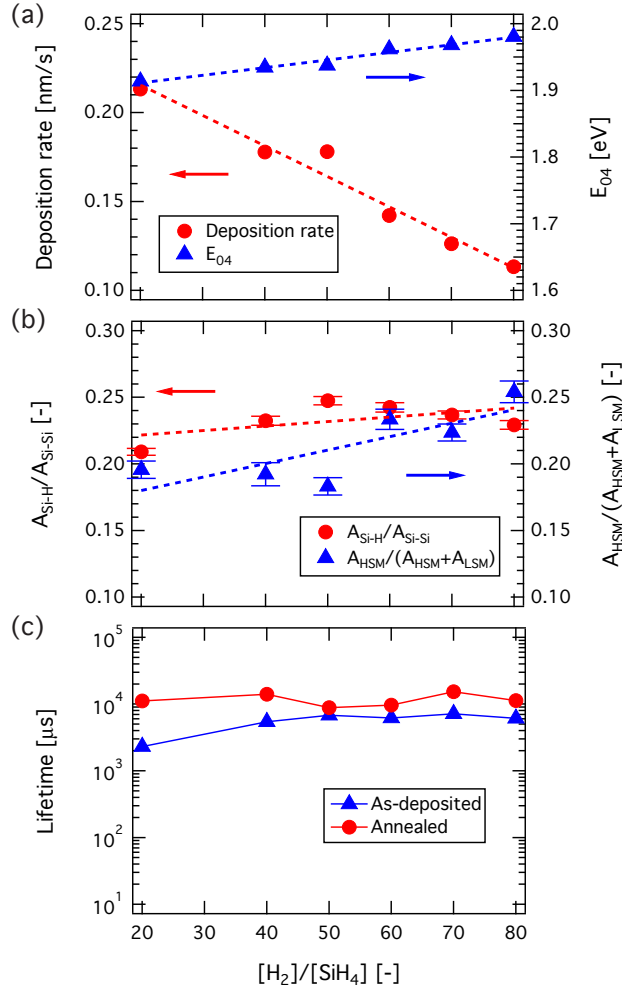
Figure 4.3: (a) Deposition rate and the optical gap as a function of hydrogen-to-silane flow ratio ($[H_2]/[SiH_4]$) with red circles and blue triangles, respectively. (b) Ratio of the peak area ($A_{Si\text{-}H}/A_{Si\text{-}Si}$) and ($A_{HSM}/(A_{HSM} + A_{LSM})$) as a function of $[H_2]/[SiH_4]$ with red circles and blue triangles, respectively. A linear fit is shown with the dashed lines. (c) As-deposited and after annealing effective lifetime at an injection level of $1 \times 10^{15}\,\mathrm{cm}^{-3}$ as a function of $[H_2]/[SiH_4]$. The deposition temperature is set at $180\,°\mathrm{C}$ and the annealing temperature is $240\,°\mathrm{C}$. The annealing time is $240\,\mathrm{min}$.
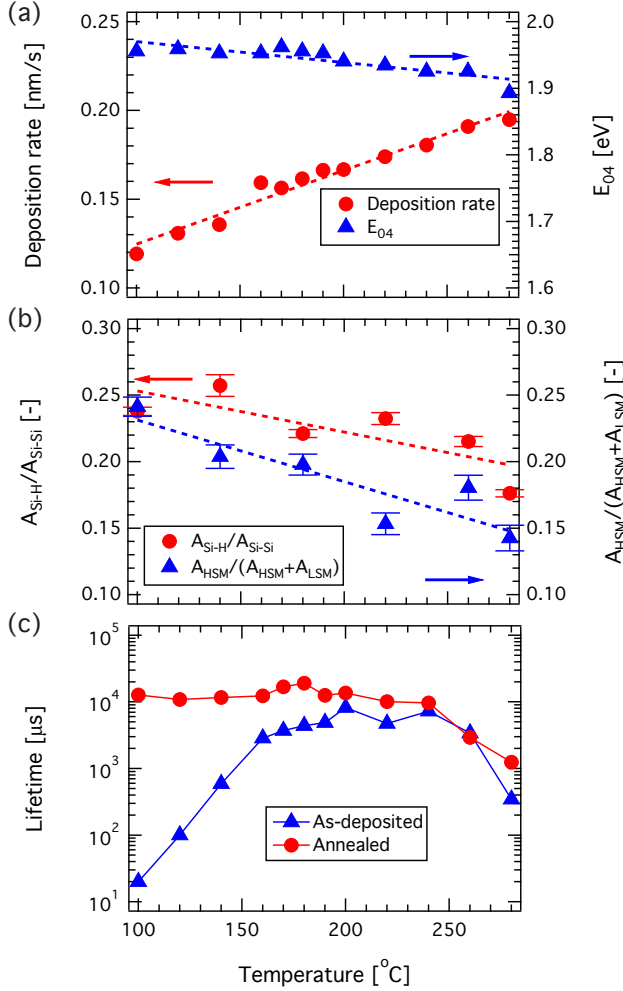
Figure 4.4: (a) Deposition rate and the optical gap as a function of substrate deposition temperature (T_{dep}) with red circles and blue triangles, respectively. (b) Ratio of the peak area (A_{Si-H}/A_{Si-Si}) and ($A_{HSM}/(A_{HSM} + A_{LSM})$) as a function of T_{dep} with red circles and blue triangles, respectively. A linear fit is shown with the dashed lines. (c) As-deposited and after annealing effective lifetime at an injection level of $1 \times 10^{15}\,cm^{-3}$ as a function of T_{dep}. The hydrogen-to-silane flow ratio is set at 50 and the annealing temperature is 240 °C. The annealing time is 120 min.

time the void density is higher at lower T_{dep} as evidenced by the increased HSM contribution [129]. For increased T_{dep} the HSM is reduced and the hydrogen concentration decreases. With annealing an increase in τ_{eff} is observed for almost all samples. The highest τ_{eff} had a value of 19 ms and was measured for the sample deposited at 180 °C. Annealing is a well-known procedure to reduce the defect density in the a-Si:H matrix and/or the interface through hydrogen equilibration [107]. De Wolf et al. [121] obtained similar results in the past, although with shorter τ_{eff}, for deposition temperatures < 200 °C. We think that the increase in τ_{eff} for our samples is due to an increase in density of our films and reduction of nano-sized voids related to the deposition conditions.

For the sample deposited at 100 °C the τ_{eff} significantly increases from 20 µs to approximately 10 ms upon annealing. It has been suggested that Si dangling bonds can convert into strained Si-Si bonds [107] or vacancy agglomeration can occur upon annealing [122]. In Figure 4.5 (a) the τ_{eff} is plotted as a function of annealing temperature for the sample deposited at 100 °C. Although the τ_{eff} increases orders of magnitude, the $A_{HSM}/(A_{HSM} + A_{LSM})$ ratio does not change within experimental error, implying that there is not a significant change in H bonding configuration. In Figure 4.5 (a) the error bars represent the standard deviation, determined from the Raman data fitting shown in Figure 4.2 (a) and (b).

The wavelength dependent refractive index and extinction coefficient are depicted in Figure 4.5 (b) and compared to the properties of a sample deposited at 220 °C. It can be seen that the extinction coefficient for the two samples is similar and the refractive index increases with T_{dep}, indicating an increase in the density of the material during deposition. However, this increase in refractive index is not observed after deposition at lower T_{dep} and subsequent annealing at 220 °C. Evidently, annealing does increase the τ_{eff} significantly, while not affecting the bulk macroscopic properties of the layer as determined from SE and Raman spectroscopy. This implies that the increase in τ_{eff} upon annealing is due to local reconstruction and defect reduction at the a-Si:H/c-Si interface, presumably by changes in the H bonding configuration near the interface that cannot be detected. Moreover, this increase in τ_{eff} is also unlikely to be related to sub-surface damage, since it is expected that much higher temperatures than 240 °C are required to be able to anneal out damage related with the c-Si substrate [130].

In agreement with previous studies the passivation quality seems not to be affected by the hydrogen bonding configuration of the layer [131, 132].
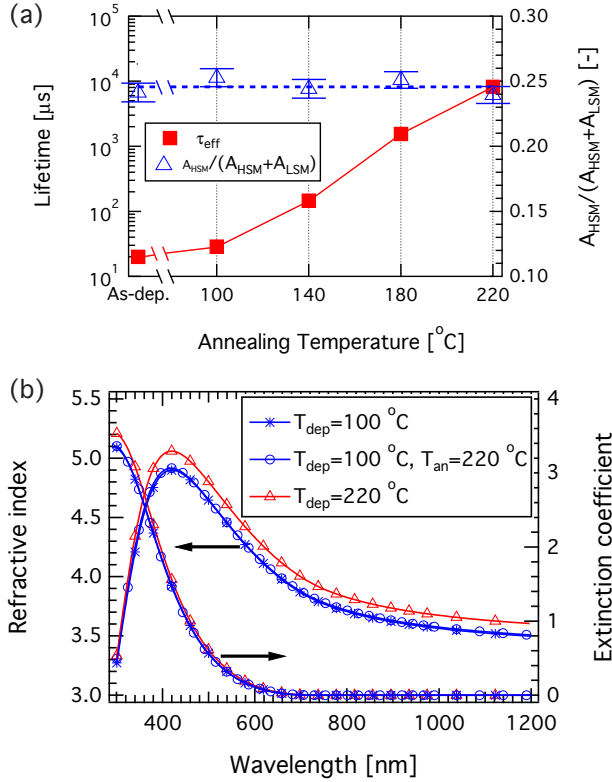
Figure 4.5: (a) Effective lifetime and ratio of the peak area of the high stretching mode to the total peak area of the high and low stretching mode ($A_{\mathrm{HSM}}/(A_{\mathrm{HSM}} + A_{\mathrm{LSM}})$) as a function of annealing temperature. The deposition temperature is 100 °C. (b) Optical constants as determined from spectroscopic ellipsometry measurements for a sample deposited at 100 °C and annealed at 220 °C, and for a sample deposited at 220 °C.

It is rather the increased density of the layers in combination with the high H content achieved that determines the τ_{eff}. The increased density of the layers with hydrogen dilution is in line with observations by Tsai et al. [133]. Such layers, i.e. with reduced nano-sized void formation during the initial stage of the growth, are beneficial from an electronic passivation perspective [121]. At the same time the high hydrogen content is reducing the defect density in the layers and the stacks approach a similar τ_{eff} after post-deposition annealing.

4.4 Conclusion

In conclusion, the high hydrogen dilution and high-pressure regime is proposed for the passivation of c-Si with a-Si:H. The results show a weak dependence of τ_{eff} on H_2 dilution, and a strong dependence on the substrate temperature, with τ_{eff} in the order of 10 ms obtained for different nanostructures. To explain the increase in τ_{eff} when using these hydrogenated plasma conditions we speculate that the extra H hydrogenates the a-Si:H/c-Si interface during deposition, while etching the layer and avoiding void formation during a-Si:H growth thus resulting in a layer with increased density. Post-deposition annealing of a sample with the a-Si:H layer deposited at 100 °C increases the τ_{eff} from 20 μs to 10 ms, while no significant changes are observed in Raman spectroscopy and SE measurements of the bulk a-Si:H, pointing towards a local redistribution of the a-Si:H network and/or the interface.

5

Thickness-dependent effective lifetime of crystalline silicon passivated with intrinsic hydrogenated amorphous silicon

This chapter is based on the publication:

Abstract

In this chapter the dependency of the effective lifetime (τ_{eff}) on the hydrogenated amorphous silicon (a-Si:H) layer thickness of crystalline silicon (c-Si) substrates passivated with intrinsic a-Si:H is studied. This is experimentally investigated by using a soft wet-etching method that enables accurate control of the a-Si:H layer thickness. In this way, variations in τ_{eff} down to thicknesses of a few nanometers are studied, while excluding effects originating from the deposition conditions of a-Si:H when samples of different thicknesses are fabricated. For thin passivation layers, results show a strong thickness dependency of τ_{eff}, which is mainly influenced by the recombination at the external a-Si:H surfaces. For thicker passivation layers, τ_{eff} is predominantly determined by the bulk a-Si:H and/or c-Si defect density. During the etching of the a-Si:H passivation layers, a gradient in the Cody gap for our samples is observed. This gradient is accompanied by a stronger decrease in τ_{eff} and is attributed to a decrease in the a-Si:H band gap and valence band offset. The observed changes in

τ_{eff} with a-Si:H layer thickness are supported with AFORS-HET simulations. When a gradient in the a-Si:H passivation layer band gap is used, simulations can reproduce the experimental results. Finally, silicon heterojunction solar cells were fabricated by first depositing a-Si:H passivation layers in the thickness range $\sim$ 7–34 nm, subsequently reducing the a-Si:H layer thickness to about 7 nm and depositing the doped layers, the transparent conductive oxide and the metal contacts. In these devices, the prolonged plasma exposure was expected to mainly influence the open circuit voltage, however results show that this is not the case.

5.1 Introduction

Silicon heterojunction (SHJ) solar cell technology has demonstrated a conversion efficiency of 25.1 % [32] and 24.7 % [31], with a state of the art V_{OC} of 738 mV and 750 mV, respectively. Furthermore, an efficiency of 26.6 % has been achieved with the SHJ solar cell fabricated in an interdigitated back contacted configuration (IBC-SHJ) [18, 19]. A key factor in achieving these high efficiencies, is the increased V_{OC} that stems from the insertions of a thin intrinsic hydrogenated amorphous silicon (a-Si:H) passivation layer in-between the p/n a-Si:H/crystalline silicon (c-Si) heterojunction [17]. This layer improves the solar cell V_{OC} by reducing the defect density and therefore the recombination rate at the c-Si surface. In the past years, numerous studies have been published on c-Si symmetrically passivated with intrinsic a-Si:H, most of which use the effective lifetime (τ_{eff}) of the stack as a measure for the passivation quality [101, 109, 110, 113, 125, 134].

τ_{eff} of the stack depends on the properties of the c-Si wafer, the a-Si:H/c-Si interface, and the properties of the intrinsic a-Si:H layers. Many studies focus on the a-Si:H/c-Si interface, the properties of the a-Si:H layers (e.g. defect density, hydrogen content, band gap and density of the layers), and the deposition conditions used [102, 107, 109, 131, 134]. In some of these literature reports, thicker layers than what is commonly used for passivation in SHJ solar cells (< 10 nm) are used. It has been observed, that thicker layers can ensure excellent passivation quality, resulting in an increased τ_{eff} and V_{OC} [98, 113, 135]. However, the origin of this increase has not been demonstrated. When a c-Si substrate is passivated with thicker a-Si:H layers the exposure of the sample to the plasma and the deposition temperature is also extended. This exposure may alter the properties of the layer, either through ion bombardment and UV illumination or through annealing, and therefore also change τ_{eff}. This implies that an increase in τ_{eff} could originate from the deposition itself, which results in an a-Si:H layer and/or a-Si:H/c-Si interface with different properties, rather than a difference in the thickness of the passivation layer.

In Figure 5.1 the average τ_{eff} can be seen for as-deposited samples symmetrically passivated with a-Si:H layers of different thickness. This is the average τ_{eff} of measurements taken daily over a period of a week. For the sample passivated with an a-Si:H layer of approximately 280 nm thickness, τ_{eff} as high as 21.5 ms has been measured. According to Richter et al. [136] the intrinsic lifetime at injection level 1×10^{15} cm^{-3} will be approximately 28 ms for the doping of the wafers used (i.e. 1.52×10^{15} cm^{-3}) due

to Auger and radiative recombination. The standard deviation is shown with the error bars and it can be seen that the samples remained fairly stable over the period of a week with the largest variation observed for the samples passivated with a-Si:H layers with thicknesses of 23 and 29 nm. This variation shows that these intermediate thicknesses are the most susceptible to changes in τ_{eff}. For thinner layers (< 23 nm) τ_{eff} is substantially shorter and therefore already limited by the thickness of the passivation layer while for thicker layers (> 29 nm) it appears that the passivation layer is thick enough so that τ_{eff} is not affected by the ambient conditions. In Figure 5.1 it can be seen that indeed τ_{eff} increases with the thickness used for the a-Si:H passivation layer. Neitzert et al. [103] have shown that during growth of a-Si:H on a c-Si substrate the a-Si:H/c-Si interface can be affected by plasma-induced species even when the a-Si:H film has a thickness of 30 nm. In their work, they measured the time-resolved microwave conductivity signal, which reflects the change in the surface recombination of the substrate. They observed a change in the surface recombination and they attributed this change to structural relaxation at the a-Si:H/c-Si interface. For the data shown in Figure 5.1, the a-Si:H/c-Si interface has been subjected to different plasma exposure times used to achieve a-Si:H passivation layers of different thicknesses. Therefore, the a-Si:H passivation layer and/or interface may have structural differences among the samples and at this point the origin of the increase in τ_{eff} observed is not clear.

In this work we deposit a thick a-Si:H passivation layer and we accurately reduce its thickness by using a wet-etching method. In this way we study the influence of the a-Si:H passivation layer thickness on the experimentally measured τ_{eff}, without changing the a-Si:H passivation layer and the a-Si:H/c-Si interface properties. At the same time we are able to exclude any influence from the deposition conditions on τ_{eff} and study the passivation in the thickness range that is used for SHJ solar cells. Using simulations we gain a better understanding of the main factors that can limit τ_{eff}. In the following sections, the experimental details are given and the etching method used in this work is explained. Then the impact of the etching method in the optical properties of a-Si:H layers is investigated. This method is applied on samples passivated with a-Si:H layers of different thicknesses and the results are discussed. To understand the experimentally observed trends, simulations are carrier out with AFORS-HET [137]. Finally, c-Si wafers are passivated with a-Si:H of various thicknesses, thicker than device standards, then the etching method is used to reduce the a-Si:H thickness and fabricate SHJ devices.
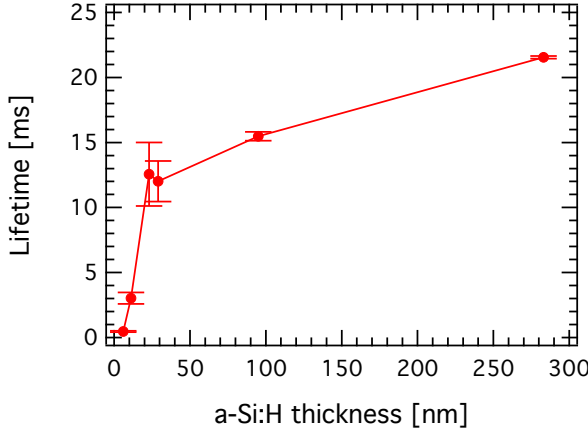
Figure 5.1: Average effective lifetime (τ_{eff}) at an injection level of $1 \times 10^{15}\,\text{cm}^{-3}$ for samples symmetrically passivated with hydrogenated amorphous silicon layers of different thickness. The as-deposited τ_{eff} shown is averaged over a period of a week. The standard deviation is shown with the error bars. The properties of the wafers and the deposition conditions used for these depositions can be found in Section 5.2.

5.2 Experimental details

For the experiments, double side polished c-Si float-zone (FZ) wafers with a thickness of $280 \pm 20\,\mu\text{m}$ were used. The wafers were n-type, with <111> orientation and resistivity of $3 \pm 2\,\Omega$ cm. Based on suppliers specifications the bulk lifetime (τ_{bulk}) of the wafers is $> 7\,\text{ms}$. This value is based on ingot lifetime measurements. Before deposition the wafers were cleaned in HNO_3 99 % at room temperature, subsequently dipped in HNO_3 69.5 % at $105 \pm 5\,°\text{C}$ and followed by a HF 0.55 % step in order to remove the silicon oxide layer. In between the steps and after the H termination with HF the substrates were rinsed in deionized (DI) water. The a-Si:H passivation layers were deposited using a radio-frequency plasma-enhanced chemical vapor deposition (RF-PECVD) reactor at excitation frequency of 13.56 MHz. For the deposition of the layers a high H_2 and high pressure deposition regime was chosen, which has been demonstrated to give good passivation quality [134]. The SiH_4 and H_2 gas flow was set at 4 sccm and 200 sccm, respectively. The substrate temperature was $180\,°\text{C}$ and the process pressure was set at 8 mbar. The power density was set at

$50\,\mathrm{mW\,cm^{-2}}$ (for the samples depicted in Figure 5.1 the power density was set at $60\,\mathrm{mW\,cm^{-2}}$).

In order to study the thickness dependence of the a-Si:H passivation layer on τ_{eff} a wet-etching approach was used consisting of a 5 min oxidation step in 69.5 % HNO_3 at $105 \pm 5\,^{\circ}\mathrm{C}$ and an oxide removal step for 2 min in 0.55 % HF at room temperature. The samples were rinsed in between the steps and after the cycle in DI water. There are two main benefits in etching the passivation layers by using such a method. Firstly, it is a soft method as compared to plasma etching, and therefore it does not damage the passivation layer with ion bombardment [113]. Secondly, it allows for an accurate control of the thickness, especially in the range that is used for SHJ passivation layers. The thickness of the oxide layers formed is self-limited and is approximately 1 nm, which is also the thickness removed with every cycle. This step approach will give better control over the thickness investigated than what is typically achieved using an etching mixture [138]. After the etching step and before τ_{eff} measurements the samples were annealed at $240\,^{\circ}\mathrm{C}$ in ambient conditions for 16 min. De Wolf et al. [139] have shown that post-deposition annealing can improve τ_{eff} of a c-Si substrate passivated with a-Si:H. At the same time this temperature is well below $300\,^{\circ}\mathrm{C}$, at which structural changes in a-Si:H start to occur [122].

τ_{eff} of the passivated wafers was measured using a Sinton Consulting WTC-120 lifetime tester in transient mode [52]. In between the measurements the samples were stored in ambient conditions. The thickness and the optical constants of the layers were determined by means of Spectroscopic Ellipsometry (SE). For the fitting of the experimental data the Cody-Lorentz model [55] was used, which was found to give more accurate fittings than the commonly used Tauc-Lorentz model [56]. For the simulations the spectrum of the Sinton flash was used as measured with an AVANTES Dual AvaSpec 2048. Finally, the etching method was used in the fabrication of SHJ devices. Intrinsic a-Si:H passivation layers with various thickness were deposited on c-Si wafers and the thickness was reduced to 5–10 nm. Subsequently, the p and n-type doped layers were deposited, with about 5 and 9 nm thickness, respectively. At the front an indium tin oxide (ITO) layer was used as a transparent conductive oxide, with 75 nm thickness. At the front a screen-printed metal grid was used and at the back an evaporated stack consisting of silver, chromium and aluminum was used.

5.3 Results and discussion

5.3.1 Determination of the a-Si:H layer etching rate

The etching method described in the experimental section, is used on a thick intrinsic a-Si:H layer (about 50 nm) deposited on a c-Si substrate in order to determine the etching rate accurately and investigate if there are any changes in the optical properties of the layer during the etching. The thickness of the intrinsic a-Si:H layer as a function of the number of etching cycles is plotted in Figure 5.2 (a). For the determination of the etching rate, the average thickness of the passivation layer has been determined using SE at three different positions on the sample, after the indicated number of etching cycles. The standard deviation of the measurements at these positions is shown with the error bars. It can be seen that a laterally homogeneous layer is initially deposited and that the layer remains homogeneous throughout the etching process. The etching rate for the intrinsic a-Si:H layers is determined from a linear fitting and is found to be 1.07 ± 0.03 nm per cycle. This etching rate will enable us to control the thickness of the a-Si:H passivation layers accurately down to thicknesses of a couple of nanometers. From the SE fittings the optical constants are determined also, in addition to the thickness of the layer during the etching process. During the etching process there is an interaction of the a-Si:H layer and the etching solution. Therefore the optical constants can provide information in case the etching solution alters the properties of the layer or in case an inhomogeneous layer was initially deposited.

In Figure 5.2 (b), the refractive index and the extinction coefficient for different number of etching cycles performed is shown. It can be seen that both the refractive index and the extinction coefficient for the as-deposited layer, after 10 and after 20 cycles are overlapping within experimental error. The optical constants are intrinsic properties of the layer and are related to its structural properties. Therefore, this shows firstly that the layer remains uniform for these thicknesses throughout the etching process, i.e. the deposition results in homogeneous layers, and secondly that the etching method used in this work does not alter the structure of the a-Si:H layer. It becomes clear from Figure 5.2 (b) that for the thickness range 48–26 nm, the optical properties of the a-Si:H passivation layers do not change with the etching of the layer. This allows us to study the relationship between a-Si:H thickness and passivation quality keeping other relevant parameters fixed.
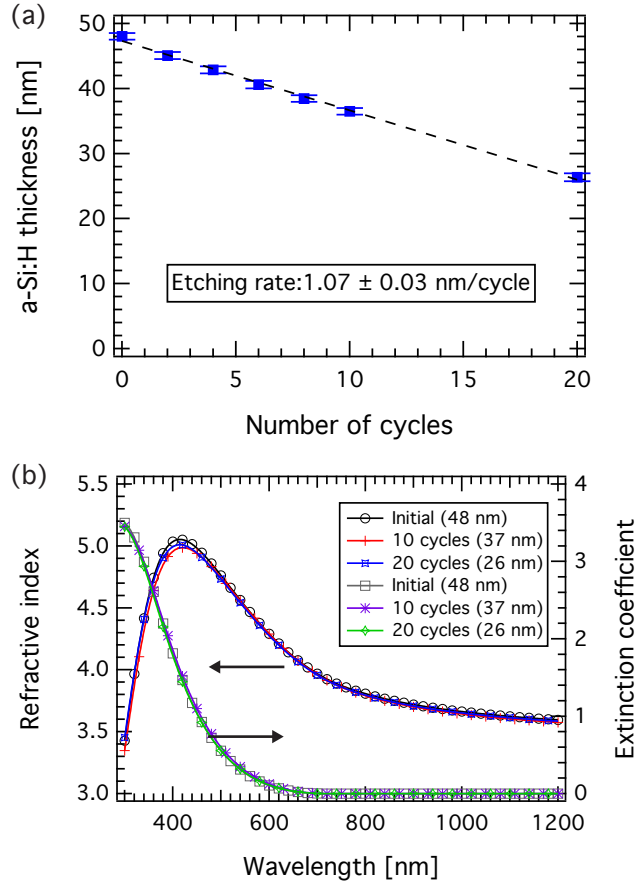
Figure 5.2: (a) The average thickness as a function of etching cycles for intrinsic hydrogenated amorphous silicon (a-Si:H) deposited on crystalline silicon substrate as determined from spectroscopic ellipsometry (SE) measurements. The standard deviation is shown with the error bars. The etching rate is 1.07 ± 0.03 nm per cycle. (b) The refractive index and the extinction coefficient, for different thicknesses of the a-Si:H layer, for the same sample, as determined from SE measurements.

5.3.2 Influence of the a-Si:H passivation layer thickness on the effective lifetime

To investigate the influence of the a-Si:H passivation layer thickness on τ_{eff}, c-Si substrates were symmetrically passivated with a-Si:H of differ-

ent initial thickness. The etching method was subsequently used to gradually reduce the thickness of the passivation layers and study the effect of the a-Si:H passivation layer thickness on τ_{eff}. During the etching process the samples were dipped in HNO_3 solution for the oxidation step. In this solution ionic species are present resulting from the self-ionization of HNO_3 followed by further ionization of H_2O in HNO_3 [140]. Adsorption of charged species on the sample surface can induce an electric field, which may lead to generation of defects at the a-Si:H/c-Si interface and therefore decrease τ_{eff} [135]. Moreover, it has been observed that wet-chemical etching can lead into hydrogen diffusion in c-Si [141, 142]. The effect of the etching process on τ_{eff} has been investigated by measuring τ_{eff} after each step, i.e. after deposition, annealing, dipping in HNO_3, dipping in HF and subsequent annealing. It was found that post-deposition annealing improves τ_{eff}. This was followed by a decrease in τ_{eff} during the oxidation step in HNO_3 and a slight increase after the oxide removal step using HF. Subsequent annealing after the HF step neutralizes the effect of etching and recovers τ_{eff}. Annealing temperature and time was separately optimized and no further improvement was observed at 240 °C after 16 min.

Before each measurement the passivated c-Si substrates were annealed for 16 min at 240 °C in order to ensure that there is no influence of the etching method on τ_{eff}. In this way we are able to study the a-Si:H thickness dependence of τ_{eff} for one and the same sample and exclude any effect from the plasma species and the deposition temperature on τ_{eff} i.e. we are not changing the a-Si:H passivation layer and a-Si:H/c-Si interface. The results can be seen in Figure 5.3 (a).

The results in Figure 5.3 (a) show that for the same sample the experimentally measured τ_{eff} is thickness dependent. τ_{eff} is defined as the ratio between the excess hole density, Δp, and the effective recombination rate U_{eff}:

$$\tau_{\text{eff}} := \frac{\Delta p}{U_{\text{eff}}}. \tag{5.1}$$

U_{eff} will be equal to the sum of the recombination rates resulting from the different physical recombination mechanisms in the sample [51]. Typically, the bulk c-Si substrate and the surface recombination rates are considered and Equation (5.1) becomes

$$\frac{1}{\tau_{\text{eff}}} = \frac{1}{\tau_{\text{bulk}}} + \frac{1}{\tau_{\text{surf}}}. \tag{5.2}$$

In Equation (5.2), τ_{bulk} and τ_{surf} are the excess minority carrier lifetimes
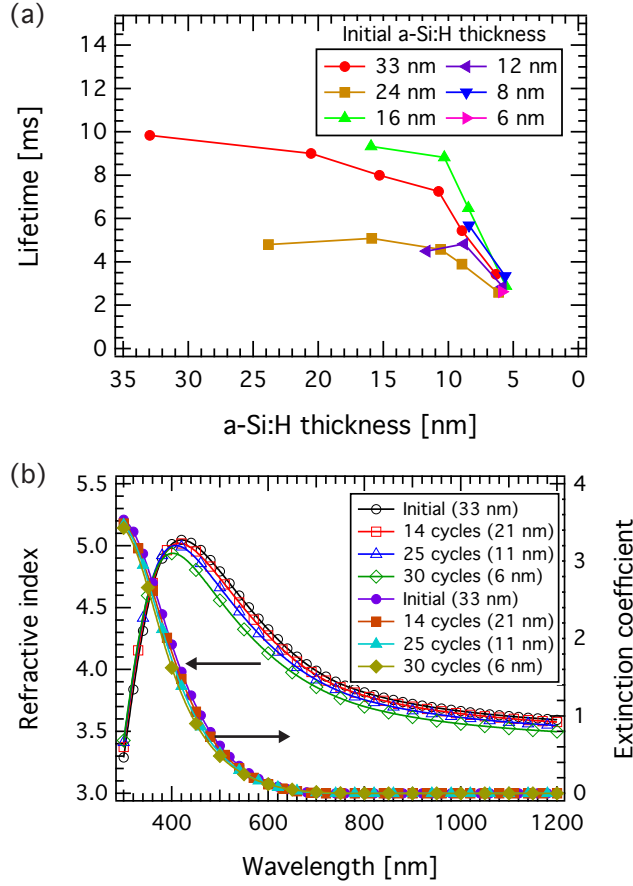
Figure 5.3: (a) Thickness dependence of the effective lifetime at an injection level of $1 \times 10^{15}\,\text{cm}^{-3}$ for samples with passivation layers of different initial thickness. (b) The refractive index and the extinction coefficient, for the sample passivated with 33 nm hydrogenated amorphous silicon, for different thicknesses as determined from spectroscopic ellipsometry measurements.

in the bulk and at the surfaces of the c-Si wafer, respectively. τ_{bulk} is determined by the processes that take place in the bulk of the c-Si substrate, i.e. Auger, radiative and Shockley-Read-Hall recombination, and is expected to be much longer than τ_{surf}. τ_{surf} is determined by the passivation properties of the a-Si:H layer and is usually the limiting term in τ_{eff}. Commonly τ_{surf} is expressed through the surface recombination velocity (S). In case of a non-passivated surface, S can reach values in the order of $10^7\,\text{cm}\,\text{s}^{-1}$, lim-

ited by the thermal velocity of the charge carriers. However, for the range of the measured τ_{eff} in the passivated samples presented in Figure 5.3 (a), S determined through Equation (5.2) using the approximation by Sproul for identical wafer surfaces [143], will be approximately $0.6\,\text{cm}\,\text{s}^{-1}$ (i.e. assuming a minority carrier hole diffusivity $D_{\text{h}} = 11.97\,\text{cm}^2\,\text{s}^{-1}$, wafer thickness $W = 280\,\mu\text{m}$ and $\tau_{\text{bulk}} = 20\,\text{ms}$). This is due to different contributions of chemical and field-effect passivation in the surface region of the c-Si wafer. In this way, the determined τ_{surf} will effectively depend on the recombination rate at the interface, the a-Si:H bulk and the external a-Si:H surface. The charge and defect distribution in these three regions, as well as the band offsets at the a-Si:H/c-Si interface and band bending in the c-Si substrate in the regions close to the surfaces will affect the value of τ_{surf}. At first sight, assuming a conformal and homogeneous a-Si:H layer and ignoring the effect of the external a-Si:H surfaces, the reduction of the layer thickness is expected to reduce the band bending in the c-Si substrate. This can be understood by the following considerations: The built-in voltage of the heterojunction will be given by the work function difference of the two materials and is equal to the voltage drop across the two regions. By solving Poissons equation, the voltage drop across the two regions can be expressed as a function of layer thickness, assuming homogeneous charge distribution in each layer:

$$V_{\text{bi}} = \frac{1}{2\epsilon_i\epsilon_0}\rho_i\chi_i^2 + \frac{1}{2\epsilon_n\epsilon_0}\rho_n\chi_n^2, \tag{5.3}$$

where ϵ_i and ϵ_n is the relative permittivity of the intrinsic a-Si:H layer and c-Si, respectively, ϵ_0 is the permittivity of vacuum, ρ_i is the charge density in the intrinsic a-Si:H layer, χ_i the intrinsic layer depletion region width, ρ_n the charge density in the depletion region of the n-type c-Si wafer, and χ_n is the n-type c-Si wafer depletion region width. The origin of ρ_i is most likely negatively charged acceptor and dangling bond states in the band gap of the a-Si:H. In Equation (5.3) charge neutrality must be satisfied, and V_{bi} is expressed as a function of χ_i as follows:

$$V_{\text{bi}} = \frac{1}{2\epsilon_0}\rho_i\chi_i^2\left(\frac{\epsilon_n\rho_n + \epsilon_i\rho_i}{\epsilon_i\epsilon_n\rho_n}\right). \tag{5.4}$$

From Equation (5.4) it can be seen that if the intrinsic a-Si:H layer is depleted and χ_i is limited by its thickness, the voltage drop across the depletion region in the c-Si substrate needs to decrease. Therefore, in thermal equilibrium the electric field in the c-Si wafer near the a-Si:H/c-Si:H

interface will decrease, reducing the minority carrier hole concentration at the interface. This implies that in terms of band bending an increase in τ_{eff} should be observed with a decrease in thickness. Evidently, the trends observed in Figure 5.3 (a) cannot be explained in terms of band bending and an alternative explanation is needed. When the a-Si:H layer thickness becomes smaller than the thickness of the depletion region, χ_i, recombination at the external a-Si:H surfaces is expected to start playing a significant role. However, this is a simplified approximation and in order to find the exact solution numerical simulation software is needed. Later in this work AFORS-HET17 will be used to explain the experimentally observed trends.

Besides the decrease of τ_{eff} with thickness, also other observations can be made that need further consideration. Firstly, it can be seen in Figure 5.3 (a) that an initially thicker passivation layer does not necessarily imply higher τ_{eff}. The 16 nm sample shows higher τ_{eff} than both the, initially thicker, 33 and 24 nm samples. Moreover, when these samples (16, 24 and 33 nm) have a similar thickness of about 15 nm τ_{eff} is different. When the thickness of the a-Si:H layers becomes similar the effect of the thickness on the voltage drop in the c-Si should also be similar. The different τ_{eff} is clearly due to a difference among the samples and can be understood through Equation (5.2) with either τ_{bulk} or τ_{surf} being the limiting terms. Assuming that τ_{surf} is the limiting term, any difference in τ_{eff}, would indicate a difference among the samples in one of the regions related to τ_{surf}, i.e. the a-Si:H/c-Si interface, the bulk a-Si:H, and the external surface of the a-Si:H layer. However, it is not likely that τ_{surf} is the limiting term since the same cleaning treatment and deposition conditions were used for all samples. Considering that the lowest τ_{eff} value obtained in this work for a-Si:H layer thicknesses larger than 10 nm is as high as approximately 5 ms and the c-Si substrates used typically have τ_{bulk} values larger than 7 ms such differences for these a-Si:H layer thicknesses possibly originate from differences in τ_{bulk}, as will be demonstrated later with simulations. Interestingly, although we find differences in τ_{eff} for the as-deposited samples of different initial thickness, τ_{eff} becomes similar at about 6 nm, also for the as-deposited sample. This observation points towards the same limiting factor when the layers become very thin. Finally, a faster decrease of τ_{eff} with decreasing thickness is observed for all samples when the thickness becomes smaller than 10 nm. This faster decrease of τ_{eff} indicates a secondary effect that needs to be taken into account. This secondary effect is reflected in Figure 5.3 (b), which shows the optical constants for different

thicknesses of the a-Si:H layer, for the same sample. This final observation needs some further discussion.

When reducing the a-Si:H layer thickness below 10 nm the optoelectronic properties of the material can change, resulting in a gradient in the band gap. This gradient is ascribed to structural changes of the material that occur during the initial stages of the growth. Fujiwara et al. [144] have observed the formation of a hydrogen-rich layer at the a-Si:H/c-Si interface during the growth of a-Si:H on c-Si substrate with a native oxide layer. This layer had a thickness of 3.5 nm and an average hydrogen content of ∼17 at. %. A similar interfacial layer, with a thickness smaller than 2 nm was also observed by Wank et al. [145], while there was a strong variation of the band gap for thicknesses less than 50 nm. In their work, this interfacial layer initially showed an increased band gap larger than 2 eV, followed by a decrease to a minimum value of 1.3 eV and a subsequent increase to the bulk band gap value of 1.6 eV. It has been shown that the band gap is correlated to the nanostructure of the a-Si:H layer i.e. the hydrogen content and the hydride configuration [120, 146]. Variations of the band gap due to hydrogen content will not only change the band gap but also the valence band offsets (ΔE_v) of the a-Si:H/c-Si heterojunction [147]. Korte et al. [148] observed a thickness dependent ΔE_v in a-Si:H/c-Si heterojunction, which they attributed to interface dipoles. In their results a decrease in ΔE_v is observed with the increase in thickness of the a-Si:H layer. ΔE_v serves as a barrier that prevents minority carrier holes from reaching the a-Si:H region and the external surface. It can be expected that a-Si:H layer structure will depend on the deposition technique, the substrate temperature, and also the deposition conditions. For our results, we expect the reduction of τ_{eff} with thickness to be accompanied with a decrease in ΔE_v and therefore also the band gap. Schulze et al. [149] have shown that in an a-Si:H/c-Si heterojunction, when the a-Si:H band gap changes the conduction band offset (ΔE_c) remains essentially constant. This implies that when ΔE_v changes, the band gap will also change. This change in band gap will influence the drift-diffusion transport mechanism in the a-Si:H/c-Si heterojunction.

The assumption that a decrease in the band gap and ΔE_v is contributing to the decrease in τ_{eff} with thickness is in line with a decrease observed in the Cody gap as obtained from the SE data. It has been shown that a decrease in the Cody gap of a-Si:H materials is typically accompanied by a decrease in the mobility gap [150]. Figure 5.4 shows the Cody gap decrease as a function of thickness. However, in this case caution is needed
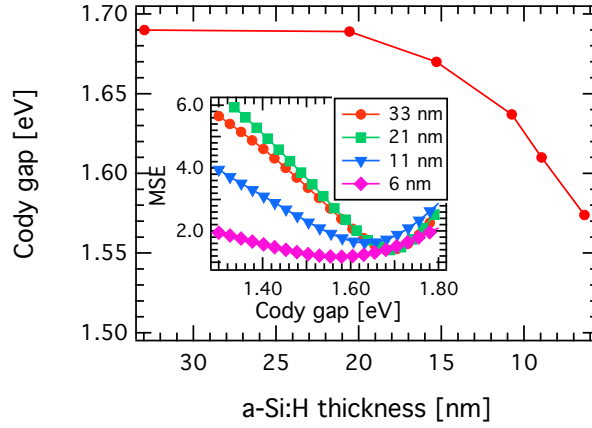
Figure 5.4: Cody gap as a function of thickness, during the etching process, for the sample initially passivated with 33 nm of hydrogenated amorphous silicon (a-Si:H). In the inset, the mean squared error is shown as a function of Cody gap for different thicknesses of a-Si:H passivation layer. For the determination of the mean squared error, the uniqueness of the fitting parameters was tested.

since when the passivation layer becomes very thin the Cody gap may not be uniquely defined anymore. For this reason the uniqueness of the fitting parameters has been tested also. The change of the mean squared error (MSE) as a function of the Cody gap for different thicknesses of the passivation layer can be seen in the inset of Figure 5.4. The decrease in the Cody gap has been determined during the etching of the layer and therefore the changes observed with thickness are not associated with the deposition process itself e.g. when a passivation layer of different thickness is deposited. In the next section simulations with AFORS-HET [137] will be used to gain better understanding of the experimentally observed τ_{eff} thickness dependency.

5.3.3 Simulation results of the thickness-dependent effective lifetime

AFORS-HET v.2.5 [137] is used to simulate the quasi-steady state photo-conductance decay (QSSPC) of a c-Si substrate, symmetrically passivated with a-Si:H. For simplicity the structure has been defined using the default software parameters of the standard intrinsic a-Si:H and c-Si layers.

The Sinton flash spectrum has been measured and used for the excitation illumination in the range 300–1100 nm. At the boundaries, flatband conditions are assumed and the recombination at the external a-Si:H surface is taken into account using a surface recombination velocity (S_{ext}), for the electrons and the holes. For the simulations the diffusion lengths of the default intrinsic a-Si:H layer are estimated by AFORS-HET to be 464 and 928 nm for electrons and holes, respectively. The dominant transport mechanisms are considered to be drift-diffusion. Moreover, no defect density is used for the a-Si:H/c-Si interface. Schulze et al. [107] have shown that the a-Si:H/c-Si interface does not possess any unique electronic properties and is rather governed by the bulk a-Si:H defects. Considering the good passivation quality obtained in this work, supported by τ_{eff} values shown in Figure 5.3 (a), not using an a-Si:H/c-Si interface defect density is reasonable and it essentially implies that the defect density at the interface is similar to the defect density in the bulk a-Si:H. The QSSPC has been simulated for varying layer thickness, band gap and defect density of the a-Si:H layer and for varying defect density of the c-Si substrate. For the Auger recombination the parameterization according to Richter et al. [136] has been used. The main parameters used for the simulation are summarized in Table 5.1.

Table 5.1: Main parameters used in simulations.

Parameters	a-Si:H	c-Si
Thickness (nm)	7–300	280×10^3
Dielectric constant	11.9	11.9
Electron affinity (eV)	3.90	4.05
Band gap (eV)	1.650–1.800	1.124
Effective conduction band density (cm^{-3})	1×10^{20}	2.843×10^{19}
Effective valence band density (cm^{-3})	1×10^{20}	2.682×10^{19}
Electron mobility (cm^2 V^{-1} s^{-1})	20	1336.0
Hole mobility (cm^2 V^{-1} s^{-1})	5	462.9
Total c-Si defect density (cm^{-3})/τ_{SRH} (ms)	-	5.00×10^8/20, 1.428×10^9/7
Dangling bond acceptor/donor density (cm^{-3})	5×10^{15}, 5×10^{18}	-
Acceptor concentration (cm^{-3})	0	0
Donor concentration (cm^{-3})	1.00×10^3	1.52×10^{15}

In Figure 5.5 the simulated band diagram for an a-Si:H passivation layer of 7 and 300 nm at thermal equilibrium can be seen. For the band diagram simulations a $S_{\text{ext}} = 0$ cm s^{-1} is used. It can be seen that a reduction of the a-Si:H layer thickness will decrease the band bending near the a-Si:H/c-Si interface. However, the recombination at the external surfaces, which is

expected to be characterized by an increased defect density, should also be taken into account in order to describe the thickness dependence observed in τ_{eff}.
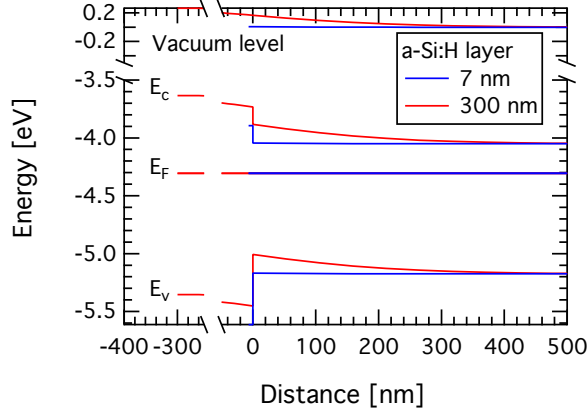

Figure 5.5: Band diagram simulations at thermal equilibrium and with the surface recombination velocity at the external hydrogenated amorphous silicon surface equal to zero ($S_{\text{ext}} = 0\,\text{cm}\,\text{s}^{-1}$) for a-Si:H passivation layer thickness of 7 and 300 nm with blue and red lines, respectively.

In Figure 5.6 (a) the simulated τ_{eff} for different S_{ext} and for different thicknesses at an injection level of $1 \times 10^{15}\,\text{cm}^{-3}$ can be seen. It is shown that when $S_{\text{ext}} = 0\,\text{cm}\,\text{s}^{-1}$, τ_{eff} is independent of the a-Si:H layer thickness. Only when $S_{\text{ext}} > 0$ τ_{eff} becomes thickness dependent. In this case, τ_{eff} reduces for thinner a-Si:H layers with increasing S_{ext}. This can be understood using the following reasoning: the region of the sample with the highest recombination rate will limit τ_{eff}. When an increased defect density describes the a-SiH/c-Si interface, this interface itself will be the limiting region. However, as the defect density at this interface is reduced, recombination will occur at the next limiting region i.e. bulk a-Si:H layer and eventually the external surfaces. When $S_{\text{ext}} = 0\,\text{cm}\,\text{s}^{-1}$ τ_{eff} will be limited only by the recombination rate in the bulk a-Si:H region. It can be seen in Figure 5.6 (a) that for our simulations an increase in S_{ext} will result in a decrease in τ_{eff} even for passivation layers as thick as 100 nm. These simulation results clearly show that when device grade a-Si:H is deposited, the recombination at the external surfaces is essential to describe the thickness dependency of τ_{eff}. Especially, when the layer becomes very thin i.e. much

smaller than the diffusion length of charge carriers in the a-Si:H.

Figure 5.6: (a) Simulation of the thickness-dependent effective surface recombination velocity (S_{eff}) at an injection level of $1 \times 10^{15}\,cm^{-3}$ for samples with different external hydrogenated amorphous silicon (a-Si:H) surface recombination velocity (S_{ext}). The acceptor and donor dangling bond density for a-Si:H layers is $5 \times 10^{15}\,cm^{-3}$. (b) Simulation of the thickness-dependent S_{eff} at an injection level of $1 \times 10^{15}\,cm^{-3}$ and $S_{ext} = 10^5\,cm\,s^{-1}$ for samples with different crystalline silicon (c-Si) defect density (N_{c-Si}) and a-Si:H acceptor and donor dangling bond density ($N_{a-Si:H}$). The defect density used for c-Si wafer corresponds to a c-Si wafer mean hole lifetime of 20 and 7 ms for a total defect density of $5.00 \times 10^{18}\,cm^{-3}$ and $1.428 \times 10^9\,cm^{-3}$, respectively.

For an a-Si:H layer thickness of approximately 300 nm the effect of S_{ext} becomes negligible and τ_{eff} will be limited by either the recombination in the bulk a-Si:H layers or the c-Si bulk. An increase in the bulk a-Si:H defect density or the c-Si defect density is shown in Figure 5.6 (b). In this case an increase is assumed in the defect density from 5.00×10^{18} to $1.428 \times 10^9\,\text{cm}^{-3}$, which results in a decrease of the mean hole lifetime due to Shockley-Read-Hall recombination from 20 to 7 ms. It can be seen that an increase in the bulk a-Si:H or the c-Si defect density will result in a reduction of τ_{eff} for the entire thickness range, especially for the thicker passivation layers. As the passivation layer becomes thinner τ_{eff} becomes limited by S_{ext} and becomes less dependent on the bulk defect density. Moreover, when an a-Si:H passivation layer with a defect density as high as $5.00 \times 10^{18}\,\text{cm}^{-3}$ is assumed, τ_{eff} substantially decreases and the thickness dependence is virtually absent.

Using the simulated trends, the experimental results shown in Figure 5.3 (a) can be explained. For the samples depicted in Figure 5.3 (a) the thickness of the a-Si:H passivation layer is reduced for the same c-Si substrate, the a-Si:H/c-Si interface and the bulk a-Si:H passivation layer. Therefore we attribute the decrease in τ_{eff} with reducing layer thickness to the recombination at the external surfaces. When the a-Si:H passivation layer becomes extremely thin (about 6 nm) all the samples tend to reach a similar τ_{eff} value. This value is imposed by the recombination at the external a-Si:H surfaces. When the a-Si:H passivation layer becomes thicker τ_{eff} appears to be limited by either the bulk a-Si:H or the c-Si substrate defect densities. This limitation can result in variations of τ_{eff} between samples, as observed for the 16, 24 and 33 nm samples of Figure 5.3 (a).

The recombination at the external surfaces can explain the observed thickness dependence of τ_{eff} . However, this recombination on itself is not sufficient to explain the experimentally observed trends. For a better matching to the observed trends the decrease in the Cody gap as shown in Figure 5.4, should be taken into account. Although this decrease in Cody gap is expected to be accompanied by a decrease in the band gap, the Cody gap and the band gap do not necessarily need to have the same value [150]. The decrease in τ_{eff} with the thickness of the a-Si:H passivation layer for different band gaps is shown in Figure 5.7. It can be seen that if the band gap is uniform across the thickness of the a-Si:H passivation layer, the simulations do not match the experimental data (blue circles and red triangles). Only when a lower band gap is used for the first few nanometers of the a-Si:H layer the simulation can reproduce the
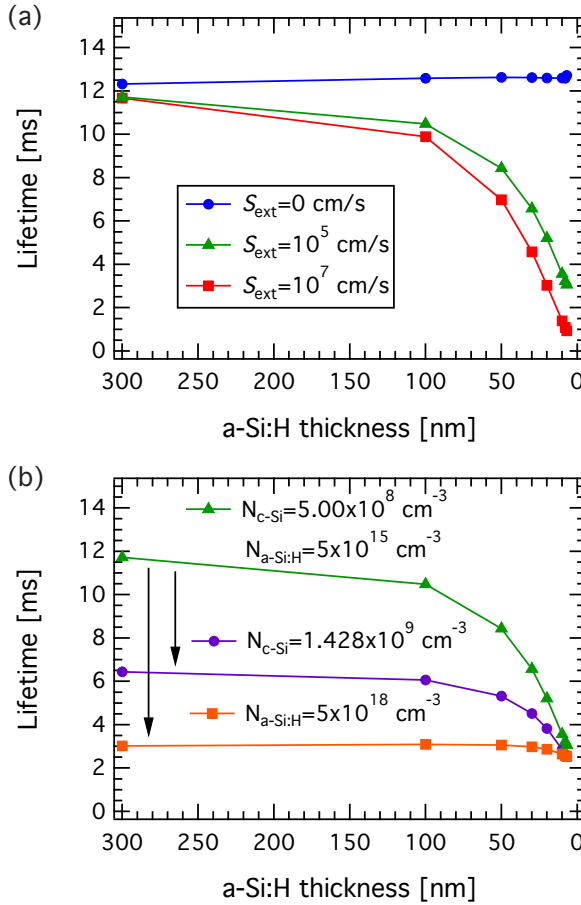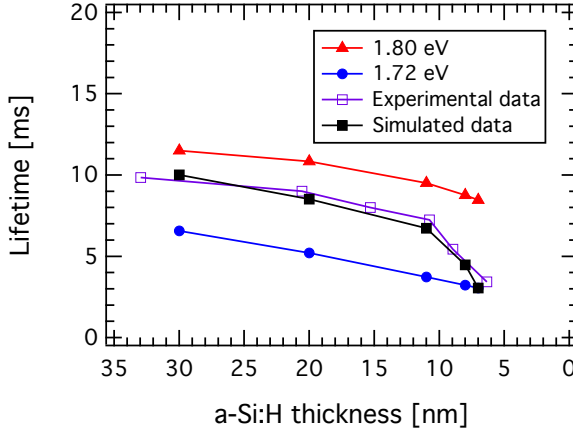
Figure 5.7: Simulation of the thickness-dependent effective surface recombination velocity (S_{eff}) at an injection level of $1 \times 10^{15}\,\mathrm{cm}^{-3}$ and for external hydrogenated amorphous silicon (a-Si:H) surface velocity (S_{ext}) equal to $10^5\,\mathrm{cm\,s}^{-1}$ for different a-Si:H passivation layer band gaps. A uniform band gap of 1.72 and 1.80 eV is shown with blue circles and red triangles, respectively. A non-uniform band gap that has a value of 1.72 eV for the first 7 nm, followed by 1.76 eV for the next 3 nm and 1.80 eV for the rest of the layer, is shown with black closed squares. The experimental data are shown with purple open squares. The acceptor and donor dangling bond density for all a-Si:H layers is $5 \times 10^{15}\,\mathrm{cm}^{-3}$.

experimental data. The effect of the band gap decrease on the thickness-dependent τ_{eff} is simulated by using an initial 7 nm of a-Si:H passivation layer with a band gap of 1.72 eV, a second 3 nm layer on top with a band gap of 1.76 eV, followed by a band gap of 1.80 eV for the rest of the layer. The simulated τ_{eff} for a gradient in the band gap can be seen in Figure 5.7 with closed black squares, while the experimentally measured data are shown with open purple squares. τ_{eff} will be slightly thickness dependent when the a-Si:H passivation layer is larger than 10 nm and a sharp decrease will follow when the layer becomes smaller than 10 nm. Using a band gap gradient for the first few nanometers of the a-Si:H layer can give a good matching with the experimental data. Although in the samples of Figure 5.3 (a) the decrease in the band gap is not as abrupt as in the simulated case, the effect on τ_{eff} will be similar.

5.3.4 Fabrication of silicon heterojunction solar cells

The etching method described in Section 5.2 was also used to fabricate SHJ devices. For this purpose c-Si wafers were passivated with intrinsic a-Si:H with various initial thicknesses. Then the intrinsic a-Si:H layer was reduced to the same thickness and the doped layers were deposited. The SHJ devices were finalized with the deposition of the ITO and the metal contacts. Typically, SHJ devices have intrinsic a-Si:H layers with 5–10 nm thickness. In this work two series of experiments are shown. In the first case the final thickness of the intrinsic a-SI:H is to approximately 5 nm and in the second case the final thickness of the a-Si:H is about 7 nm. The reduction of the intrinsic a-Si:H layer thickness, benefits the fill factor and the short circuit current density of the device by reducing the series resistance and the parasitic absorption losses, respectively.
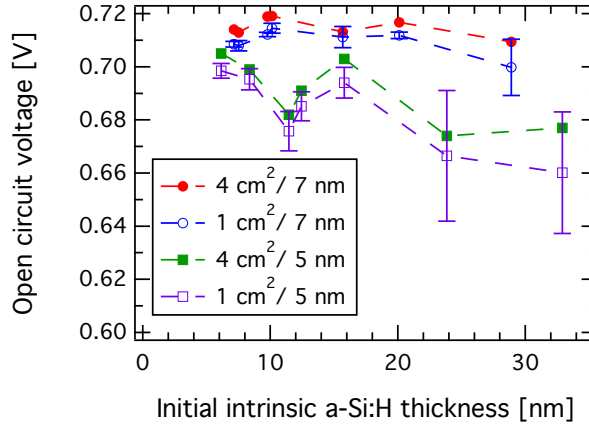
Figure 5.8: Open circuit voltage (V_{OC}) as a function of initial intrinsic hydrogenated amorphous silicon (a-Si:H) layer thickness. The data for about 7 nm final thickness of intrinsic a-Si:H is shown with red and blue markers and for 5 nm final thickness of intrinsic a-Si:H is shown with green and purple markers. Multiple devices are fabricated on each crystalline silicon wafer with an area of $4\,cm^2$ and $1\,cm^2$. V_{OC} of the device with an area of $4\,cm^2$ is shown with red and green markers and the average V_{OC} of six $1\,cm^2$ devices is shown with blue and purple markers. The error bars represent the standard deviation.

The purpose of this experiment is to investigate in which extent the prolonged plasma exposure can influence the external parameters of the de-

vice. In this case, the parameter expected to be mainly influenced is the open circuit voltage (V_{OC}). Figure 5.8 shows the V_{OC} of the devices as a function of the initial intrinsic a-Si:H layer thickness. Since multiple devices were fabricated on each c-Si wafer, Figure 5.8 shows the V_{OC} of a device with an area of $4\,cm^2$ and the average V_{OC} of six devices with an area of $1\,cm^2$. The standard deviation is used for the error bars to represent the variation between the $1\,cm^2$ devices. It is shown in Figure 5.8 that the V_{OC} is independent of the initial a-Si:H thickness and devices with different thickness have similar V_{OC}, e.g. the $4\,cm^2$ devices with initial thickness of about $7\,nm$ and $16\,nm$ (red markers). However, V_{OC} appears to be dependent on the intrinsic a-Si:H layer final thickness, with the $7\,nm$ devices showing significantly higher V_{OC} than the $5\,nm$ devices. Moreover, the $1\,cm^2$ have slightly lower V_{OC} than the $4\,cm^2$ devices. Finally, significantly larger variation in V_{OC} is observed for the two initially thicker $1\,cm^2$ devices with $5\,nm$ final intrinsic a-Si:H layer thickness.

In the results presented in Section 5.3.2 only intrinsic layers were deposited and the thickness dependence is explained in terms of recombination at the external a-Si:H surface. However, in the SHJ devices the doped layers are also deposited, which will strongly influence τ_{eff}. The presence of the doped layers will induce an electric field attracting or repelling minority carrier holes at the interface where the p- and n-type doped layers are deposited, respectively. De Wolf et al. [151] suggested that the presence of the defective p-type doped layer on n-type c-Si introduces an effective channel for the minority carriers to recombine. Additionally, a Fermi energy dependent generation of defects is influencing recombination at the a-Si:H/c-Si interface in the presence of doped layers [135]. Besides the influence of the doped layers, the properties of the intrinsic a-Si:H may also influence the passivation and the final V_{OC}, e.g. a gradient in the band gap as presented in Figure 5.7. The increased standard deviation in some of the samples shows a degree of inhomogeneity. The larger standard deviation is observed in the samples with $5\,nm$ final intrinsic a-Si:H layer thickness and especially, to the ones subjected to many etching cycles. Therefore, this variation in V_{OC} could be related to inhomogeneity in the thickness and not the intrinsic properties of the layer, as it becomes more profound when the layer is thinner (i.e. $5\,nm$ instead of $7\,nm$). From Figure 5.8 it becomes clear that V_{OC} of the device is not being determined by the initial thickness of the a-Si:H layer and is determined by the properties of the stack after the deposition of the doped layers. This is expressed in the measured τ_{eff}.
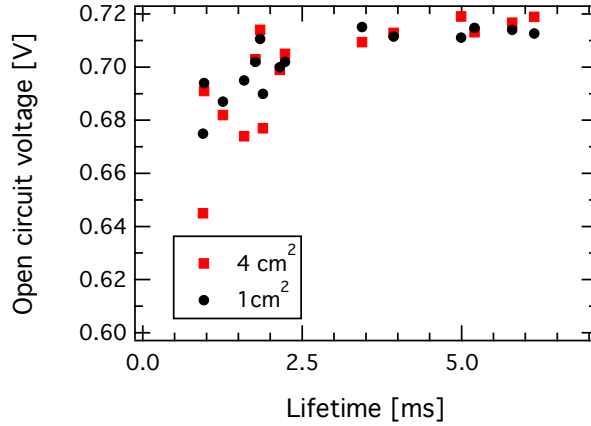
Figure 5.9: Open circuit voltage as a function of the effective life-time (τ_{eff}) of the stack after the doped layer deposition. The open circuit voltage is plotted for the devices with an area of $4\,cm^2$ and $1\,cm^2$. The $1\,cm^2$ device shown is selected at the possition of the wafer, in which τ_{eff} is measured.

In Figure 5.9, V_{OC} is plotted as a function of τ_{eff} of the samples, for the $4\,cm^2$ device and for a $1\,cm^2$ device, selected at the position on the wafer in which τ_{eff} is measured. This τ_{eff} is measured after the doped layer and before the ITO and the metal contact deposition. Figure 5.9 shows an increase in V_{OC} with τ_{eff} that saturates when τ_{eff} is about $2\,ms$. For τ_{eff} below $2\,ms$ a decrease in V_{OC} is observed, limiting the device performance. Besides the V_{OC} a slight difference was observed in the fill factor (*FF*). The samples with $5\,nm$ had the highest *FF*, while the $1\,cm^2$ devices had also higher *FF* than the $4\,cm^2$ devices. The *FF* is a complex quantity that depends on all the layers, interfaces and the metalization. This is already shown in Table 1.1 in Chapter 1. It is likely that the increased *FF* in the devices with $5\,nm$ final a-Si:H thickness is due to a reduction in series resistance, as compared to the devices with $7\,nm$ final a-Si:H thickness. The increase in *FF* for the smaller area devices, can be attributed to a better carrier collection due to metalization, limited by the ITO lateral conductivity. The short circuit current density was similar for all the samples.

In Figure 5.10 the illuminated current-voltage characteristics is given for the best SHJ, with an area of $4\,cm^2$ and $1\,cm^2$ fabricated by reducing the thickness of initially thicker intrinsic a-Si:H passivation layers. The increased series resistance for the $4\,cm^2$ device can be seen from the steep-
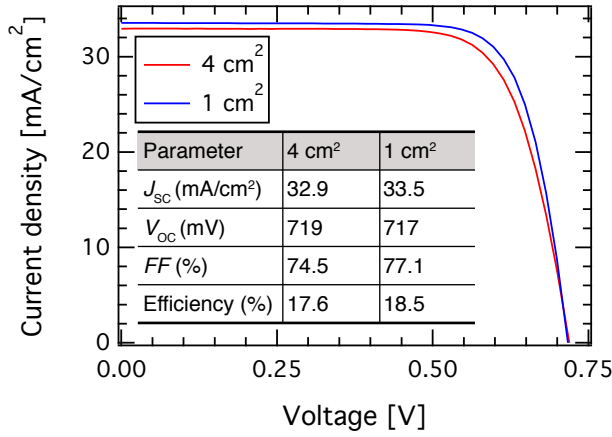
Figure 5.10: Illuminated current density as a function of voltage for the best silicon heterojunction solar cells, with an area of $4\,cm^2$ and $1\,cm^2$, fabricated by depositing thick intrinsic layers and using the etching method. The values for the short circuit current density (J_{SC}), the open circuit voltage (V_{OC}), the fill factor (FF) and the efficiency, are given in the inset table.

ness of the current-voltage characteristics near the V_{OC} region. Further, improvement in efficiency could be obtained by using textured instead of polished wafers as substrates, which would result in an increase in J_{SC}.

5.4 Conclusion

In conclusion, using an accurate wet-etching method the thickness of the a-Si:H layers passivating c-Si substrates is varied and τ_{eff} of the samples is shown to be thickness dependent for device-grade a-Si:H passivation layers. This result shows that the increased τ_{eff} with the thickness of the passivation layer is a direct effect of the increased thickness of the layer rather than an effect of the deposition conditions. For thin a-Si:H passivation layers τ_{eff} is mainly limited by the recombination at the external surfaces. For thicker passivation layers, both the defect density of the substrate and the a-Si:H passivation layer will determine τ_{eff}. When the layer becomes smaller than 10 nm a faster decrease in τ_{eff} is observed. This faster decrease is attributed to a gradient in band gap and ΔE_v during the first stages of the growth. This decrease in band gap and ΔE_v is due to structural differ-

ences in the a-Si:H passivation layer deposited during the initial stages of the growth. A decrease in the band gap and therefore also ΔE_v will have an effect in the complete thickness range investigated in this work. Using our deposition conditions, fabricating devices by depositing initially thicker passivation layers and subsequently reducing thickness does not appear to improve the external parameters of the device. When a SHJ device is fabricated the passivation, as expressed in V_OC, appears to be rather determined by the doped layers.

6

Passivation mechanism in silicon heterojunction solar cells with intrinsic hydrogenated amorphous silicon oxide layers

Abstract

In this chapter we use hydrogenated amorphous silicon oxide (a-SiO$_x$:H) layers with varying oxygen content (c_O) but similar hydrogen content to passivate crystalline silicon wafers. Investigating the passivation properties of a-SiO$_x$:H layers is crucial since these layers can be used in silicon heterojunction solar cells to reduce parasitic absorption. Using our deposition conditions we obtained an effective lifetime (τ_{eff}) of 5 ms for c_O smaller or equal to 6 at. % for passivation layers with thickness of 36 ± 2 nm. By increasing the c_O content the optical band gap of the passivation layers increased from about 1.91 to 2.13 eV, indicating an improvement in transparency of the layer. We subsequently reduced the thickness of the layers using an accurate wet etching method to approximately 7 nm and deposited p- and n-type doped layers fabricating a device structure. After the deposition of the doped layers τ_{eff} appears to be predominantly determined by the doped layers themselves and is less dependent on the c_O of the a-SiO$_x$:H layers. The results suggest that τ_{eff} is determined by field-effect rather than by chemical passivation.

6.1 Introduction

One of today's most efficient technologies for photovoltaic power generation is based on silicon heterojunction (SHJ) solar cells. This technology combines the advantages of crystalline silicon (c-Si) and hydrogenated amorphous silicon (a-Si:H) and has demonstrated a conversion efficiency of 25.1 % [32] and 26.6 % [18, 19] in a standard and interdigitated back contacted configuration (IBC-SHJ), respectively. The high conversion efficiency achieved is partly due to the increased open-circuit voltage (V_{OC}) realized with the use of a thin intrinsic a-Si:H passivation layer between the boron-doped (p-type) a-Si:H and the phosphorus-doped (n-type) c-Si wafer [100]. Although this passivation layer is able to reduce the recombination rate, increasing the V_{OC} of the SHJ device, it also increases parasitic absorption losses decreasing the short-circuit current density (J_{SC}) of the solar cell. Zhang et al. [152] showed that 2.09 % of light is absorbed in the intrinsic a-Si:H passivation layer. Holman et al. [153] showed that for the standard configuration only 30 % of the light absorbed in the intrinsic a-Si:H contributes to J_{SC}, while in the p-type layer all absorption is parasitic. Even in the IBC-SHJ configuration an intrinsic passivation layer is still used at the front surface of the c-Si wafer to decrease the recombination losses, and the implementation of this layer will also result in some parasitic absorption [97]. In order to decrease parasitic absorption in the layers on the illuminated side, different a-Si:H alloys have been investigated such as hydrogenated amorphous silicon oxide (a-SiO$_x$:H) [154–159], hydrogenated amorphous silicon oxynitride (a-SiO$_x$N$_y$:H) [160] or hydrogenated amorphous silicon carbide (a-SiC$_x$:H) [161–165].

The present work focuses on the application of a-SiO$_x$:H as a passivation layer. When a-Si:H is alloyed with oxygen an increase in the optical gap is observed with increasing oxygen content (c_O), which leads to decreased absorption losses [159]. The increase observed in the optical gap is due to structural changes in the layer, and these changes likely depend on the deposition conditions and c_O. The increasing c_O can increase the porosity of the layer and result in the presence of interconnected voids [166]. In turn such structural changes may affect the passivation properties of the layer when a-SiO$_x$:H is used to passivate c-Si. Einsele et al. [158] have attributed the poor passivation they observed for as-deposited and low temperature annealed samples to the presence of such interconnected voids in the layer. Seif et al. [154] observed also a systematically poor passivation when they deposited intrinsic a-SiO$_x$:H of different composition directly on c-Si wafer

surfaces and to improve the passivation they had to use a very thin a-Si:H layer as an interlayer between the a-SiO$_x$:H and the c-Si wafer. Liebhaber et al. [155] and Mews et al. [156] have altered the a-SiO$_x$:H stoichiometry, x, in the a-SiO$_x$:H/c-Si heterojunction and observed a decreasing effective lifetime (τ_{eff}) and therefore also an increasing interface defect density with increasing x. Mews et al. [156] have subsequently deposited p-type a-Si:H layers on the a-SiO$_x$:H with varying x and interestingly in some cases observed an increase in τ_{eff}. They attributed this increase in τ_{eff} to additional hydrogen provided by the plasma during the deposition of the p-type a-Si:H layer. Neitzert et al. [103] measured time-resolved microwave conductivity signals of a c-Si substrate during the growth of a-Si:H as a measure of the surface recombination velocity. They observed changes in the signal even when the a-Si:H layer had a thickness of about 30 nm and they attributed these changes to a structural relaxation at the a-Si:H/c-Si interface due to plasma induced species. Moreover, it has been shown for a-Si:H that when the a-Si:H layer and a-Si:H/c-Si interface defect density is decreased, the recombination at the external a-Si:H surface can strongly influence τ_{eff}, for thicknesses in the order of nanometers [167]. In this case the transport of carriers to the external a-Si:H surface is significant. It is expected that the external surfaces will have a similar influence on τ_{eff} when a-SiO$_x$:H is used as a passivation layer, especially when c_O remains low. Alloying a-Si:H with oxygen will lead to an increase in the band gap of the a-Si:H layer, which alters the valence band offset (ΔE_v) at the a-Si:H/c-Si heterointerface [155]. Increasing ΔE_v disrupts the hole transport across the a-Si:H/c-Si heterointerface [156], and therefore also to the a-Si:H layer and the external a-Si:H surface. This is reflected in SHJ devices with poor fill factors (*FF*) [154, 156]. Therefore, the passivation quality as reflected in τ_{eff}, is a rather complex quantity influenced not only by the intrinsic properties of the layer but also by the characteristics of the stack.

In this work we passivate c-Si wafers with 36 ± 2 nm a-SiO$_x$:H layers of varying c_O and high hydrogen content (c_H). Though these layers are thick for device standards, we use this thickness to achieve a prolonged plasma exposure as compared to layers of 5–10 nm. It has been shown that during this prolonged plasma exposure plasma-induced species can reduce the defect density at the a-Si:H/c-Si interface [103]. We subsequently reduce the thickness of the a-SiO$_x$:H layers to about 7 nm using an accurate wet etching method [167] and deposit p- and n-type layers to obtain a device structure and study the effect of oxygen incorporation in the passivation properties of the layer. Using our deposition conditions, we obtain lay-

ers with similar c_H being able to investigate the impact c_O has on the τ_{eff}. Finally, τ_{eff} of the device structures is compared with τ_{eff} of a structure in which the top intrinsic passivation layer is omitted (p-type structure). The results provide insights on what determines the measured τ_{eff} in these structures.

In Section 6.2.1 and Section 6.2.2 the experimental details for the sample preparation and characterization methods are given, respectively. In Section 6.3.1 the structural properties of the a-SiO$_x$:H layers used for passivation are investigated. Finally, in Section 6.3.2 the a-SiO$_x$:H layers are used as passivation layers and the experimental results are discussed.

6.2 Experimental details

6.2.1 Sample preparation

The composition (c_O and c_H) of the intrinsic a-SiO$_x$:H layers was determined using Fourier-transform infrared (FTIR) spectroscopy. For this purpose the layers were deposited on <100> orientation one side polished n-type c-Si Czochralski wafers with a thickness of $525 \pm 25\,\mu m$ and resistivity of $15 \pm 5\,\Omega\,cm$. For the other experiments intrinsic a-SiO$_x$:H layers were deposited on <111> oriented, double-side polished, n-type c-Si float-zone wafers with a thickness of $280 \pm 20\,\mu m$ and resistivity of $3 \pm 2\,\Omega\,cm$. Prior to the deposition, the wafers were cleaned by dipping them in 99 % nitric acid (HNO$_3$) at room temperature, subsequently dipping them in 69.5 % HNO$_3$ at $105 \pm 5\,°C$ and followed by a hydrofluoric acid (HF) 0.55 % step to remove the surface silicon oxide layer. In between the steps and after the hydrogen termination with HF acid the wafers were rinsed in deionized (DI) water. The a-Si:H and a-SiO$_x$:H layers were deposited using radio-frequency plasma-enhanced chemical vapor deposition (RF-PECVD) in a high pressure and high hydrogen dilution regime, which is able to yield high quality passivation [134]. A mixture of silane (SiH$_4$), carbon dioxide (CO$_2$) and hydrogen (H$_2$) was used and the c_O of the layers was altered by varying the CO$_2$ gas flow ratio

$$f_{CO_2} = \frac{[CO_2]}{[CO_2] + [SiH_4]},\tag{6.1}$$

with [CO$_2$] as the CO$_2$ flow rate and [SiH$_4$] as the SiH$_4$ flow rate.

After the deposition of the intrinsic a-SiO$_x$:H layers, the thickness dependence of τ_{eff} was studied, using an accurate wet-etching method to

etch down the samples [167]. The method consists of 5 min dip in 69.5 % HNO$_3$ at $105 \pm 5\,°C$ and subsequent dip for 2 min in 0.55 % HF at room temperature. The samples were rinsed in between the steps and after the HF dip in DI water. Subsequently, p- and n-type layers were deposited on the samples to fabricate a device structure. The deposition conditions for the intrinsic a-SiO$_x$:H passivation layers and the doped layers are summarized in Table 6.1.

Table 6.1: Process parameters for the RF-PECVD deposition of the intrinsic a-SiO$_x$:H passivation layers, p-type and n-type a-Si:H layers.

Parameter	Value (intrinsic / p-type / n-type)	Unit
Plasma excitation frequency [a]	13.6	MHz
Substrate temperature [a]	180	°C
Power density	50 / 14 / 15	mW cm^{-2}
Pressure	8.00 / 0.70 / 0.60	mbar
H$_2$ flow	200 / 0 / 0	sccm
SiH$_4$ flow	8 / 20 / 40	sccm
CO$_2$ flow	0–32 / 0 / 0	sccm
B$_2$H$_6$ flow	0/ 1 / 0	sccm
PH$_3$ flow	0/ 1 / 0	sccm
Deposition rate	0.17–0.21 / 0.23 / 0.07	nm s^{-1}

[a] The process parameter is the same for all the layers.

6.2.2 Characterization methods

To measure τ_{eff} of the passivated wafers a Sinton Consulting WTC-120 photoconductance decay lifetime tester was used, in transient or quasi-steady state mode at an injection level of $1 \times 10^{15}\,cm^{-3}$ [52].

For the FTIR measurements a Thermo Scientific Nicolet 5700 spectrometer was used in transmittance mode in the spectral range of 400–4000 cm^{-1}. FTIR was used to measure structural information for the a-Si:H and a-SiO$_x$:H layers [57–59, 64, 65, 117, 129, 168–170]. The Si-H wagging mode at 640 cm^{-1} and the Si-O-Si stretching mode at 980 cm^{-1} were used to estimate c_{H} and c_{O}, respectively [57, 65]. For the estimation of c_{H} the infrared absorption integrated absorbance has been related to the hydrogen concentration, [57] using the proportionality constant obtained by Langford et al. [64] (i.e. $2.1 \times 10^{19}\,cm^{-2}$). c_{H} is then specified as the fraction of hydrogen concen-

tration to 5×10^{22} cm^{-3} provided that the total atomic density is independent of the hydrogen content [64, 171]. For the estimation of c_O the proportionality constant by Lucovsky et al. [65] (i.e. 0.156 at. % eV^{-1} cm^{-1}) was used. To estimate this proportionality constant Lucovsky et al. calibrated the infrared absorption data with the chemical composition of the films, as obtained from electron-microprobe analysis and SIMS.

The thickness and the optical constants of the a-SiO$_x$:H layers were determined by means of spectroscopic ellipsometry (SE), assuming the layers to be a mixture of a-Si:H and silicon monoxide (SiO). For the a-Si:H material the Cody-Lorentz model [55] was used, which was found to give better fittings than the commonly used Tauc-Lorentz model [56]. The mixture of a-Si:H and SiO was analyzed using the Bruggeman effective medium theory [172]. From the analysis the c_O of the layers using SE has also been determined. The layers used for the FTIR analysis were found to have a thickness of 109 ± 5 nm and the passivation layers were found to have an initial thickness of 36 ± 2 nm. In between the measurements the samples were stored in ambient conditions.

6.3 Results and discussion

6.3.1 Structural properties of the a-SiO$_x$:H layers

In order to find out how c_H and c_O change with the deposition conditions FTIR spectroscopy and SE was used. In Figure 6.1 the FTIR transmittance spectra for layers deposited with increasing f_{CO_2} can be seen. The transmittance at 640, 980, 2005 and 2090 cm^{-1} is indicated with dashed lines. These bands are related to the Si-H wagging mode [57, 64], the Si-O-Si stretching mode [58, 65], and the Si-H low and high stretching mode, respectively [57, 170]. It can be seen that when CO$_2$ is introduced, the Si-O-Si stretching mode appears and becomes more profound with increasing f_{CO_2}. At the same time, a slight shift to higher wavenumbers is observed. These observations are in line with previous reports and are related to an increase in c_O [65, 173]. Alloying a-Si:H with oxygen results in infrared absorption at about 980 cm^{-1}, [174] which increases in intensity and shifts to higher wavenumbers. The observed shift is associated to the number of oxygen atoms attached to the bonding positions of the two silicon atoms in the Si-O-Si configuration with increasing c_O [65]. Increasing the f_{CO_2} results also in a less profound Si-H low stretching mode and a more profound Si-H high stretching mode. In a-Si:H the Si-H low stretching mode

has been assigned to monohydrides [57, 59] while the Si-H high stretching mode has been assigned to dihydrides [57, 59] and/or monohydrides at the surface of nanosized voids [129, 169]. However, in a-SiO$_x$:H the shift in wavenumber with increasing c_O has been associated to the presence of the strongly electronegative oxygen atoms, backbonded to the silicon atoms [175, 176]. At this point the contribution of nanosized voids in the Si-H high stretching mode, i.e. the material becoming more porous with increasing f_{CO_2}, is not clear. However, it is reasonable to assume that there is some contribution of oxygen backbonded onto silicon in shifting the Si-H low stretching mode to higher wavenumbers, since c_O is increasing.
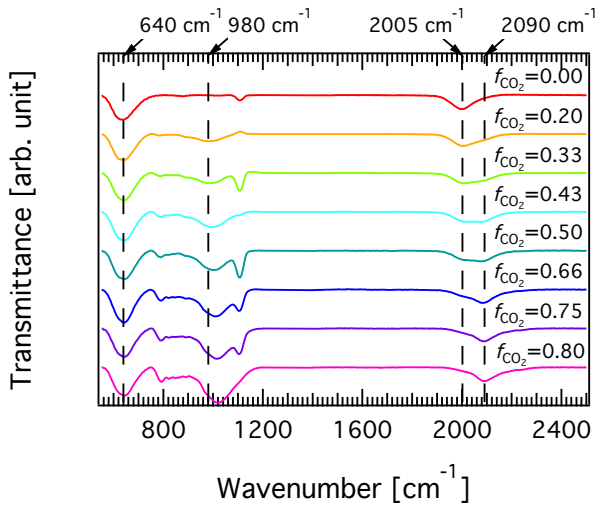
Figure 6.1: The Fourier-transform infrared spectroscopy transmittance spectra for layers deposited with increasing f_{CO_2}. The wavenumber positions for the different absorption modes are indicated with the dashed lines.

The c_O and c_H of the layers can be seen in Figure 6.2 (a). The details for the calculation can be found in Section 6.2.2. c_O has been separately determined for all the deposition conditions used, using FTIR analysis ($c_{o,FTIR}$) on samples with a-Si:H layers of 109 ± 5 nm thickness and using SE ($c_{o,SE}$) on the layers used for passivation with a thickness of 36 ± 2 nm. It can be seen that c_O indeed increases with the f_{CO_2} and that comparable c_O is obtained using the two different methods. c_H has been determined from FTIR analysis and it is very comparable for all the samples, at about 21 at. % with only a slight increase with f_{CO_2}. Schulze et al. [107] has

shown that c_H and hydrogen configuration can be crucial for the reduction of interface defect density at the a-Si:H/c-Si heterojunction. Moreover, c_H will have an influence in the a-Si:H band gap and the a-Si:H/c-Si heterojunction band lineup. The final c_H of the layers, when changing f_{CO_2}, will be determined by the deposition conditions used. Liebhaber et al. [155] found a c_H decrease with increasing c_O, while Seif et al. [154] observed an increase and Einsele et al. [158] only a weak increase in c_H with increasing c_O. Due to similar c_H obtained in this work, it can be assumed that any difference in τ_{eff} between the samples discussed in Section 6.3.2, will be due to differences in microstructure and c_O and not due to an insufficient c_H. The increase in c_O enhances the E_{04} optical band gap of the layer from about 1.91 to 2.13 eV. The E_{04} optical band gap as determined from SE measurements can be seen in Figure 6.2 (b).

6.3.2 Passivation of c-Si wafers with a-SiO$_x$:H layers

In Figure 6.3 the three sample structures on which τ_{eff} has been investigated can be seen. For the first structure c-Si wafers have been symmetrically passivated with intrinsic a-SiO$_x$:H with a thickness of 36 ± 2 nm (i.e. intrinsic stack in Figure 6.3). The etching method described in Section 6.2.1 was used to reduce the thickness of the a-SiO$_x$:H passivation layer gradually and study the thickness dependence of τ_{eff}. Before each lifetime measurement the samples were annealed for 15 min at 240 °C to ensure that there is no influence of the etching process on τ_{eff}. De Wolf et al. [139] have shown that annealing can increase τ_{eff} in c-Si wafers passivated with intrinsic a-Si:H by yielding very low a-Si:H/c-Si interface recombination rate, provided that neither an epitaxial silicon layer is deposited at the interface [92] nor a p-type overlayer is present [135, 151, 177]. The influence of annealing time on τ_{eff} has been investigated (not shown here) and 15 min at 240 °C was found to be sufficient for the samples passivated with a-SiO$_x$:H. Similar annealing time has been used previously to neutralize the effect of the etching method on τ_{eff} in samples passivated with a-Si:H [167]. Subsequently all samples were etched down to a thickness of approximately 7 nm and p- and n-type a-Si:H layers with a thickness of about 5 and 9 nm, respectively, were deposited (i.e. device structure in Figure 6.3). τ_{eff} of the device structure was compared with τ_{eff} of a device in which the top intrinsic a-SiO$_x$:H layer was omitted and the p-type layer was chosen to have a thickness of approximately 13 nm (i.e. p-type structure in Figure 6.3). The purpose of this comparison is to isolate the effect of

(a)

(b)
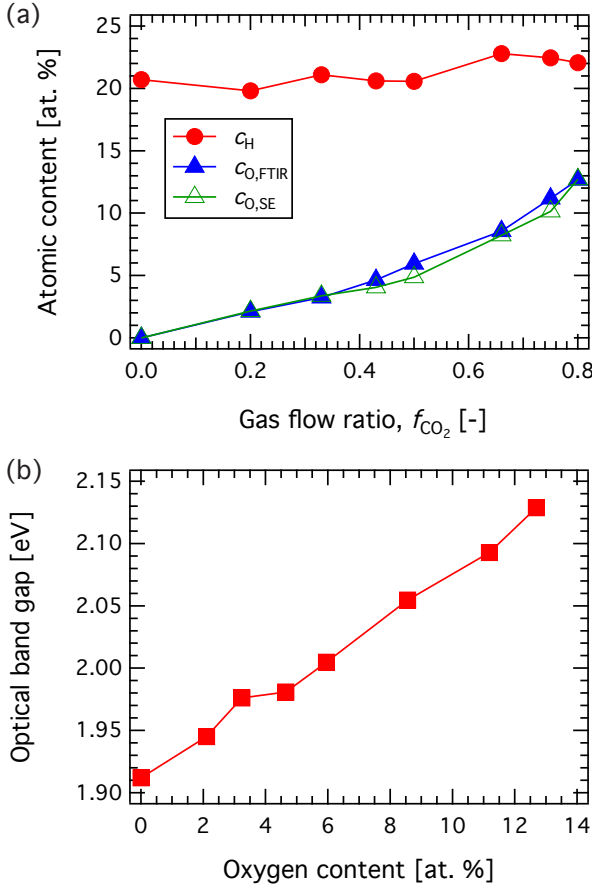
Figure 6.2: (a) Hydrogen and oxygen ($c_{o,FTIR}$) content as determined from Fourier-transform infrared spectroscopy analysis and oxygen ($c_{o,SE}$) content as determined from spectroscopic ellipsometry (SE) analysis. (b) Optical band gap (E_{04}) for increasing oxygen content, as determined from SE analysis.

the doped layer on τ_{eff}. The bottom intrinsic layer in the p-type structure is an a-Si:H layer with a thickness of about 7 nm.

In Figure 6.4 (a) the τ_{eff} as a function of the a-SiO$_x$:H thickness is shown for samples passivated with layers that are deposited using different f_{CO_2}. It can be seen that τ_{eff} well above 10 ms is achieved when $f_{CO_2} < 0.5$ with the deposition conditions used in this work. Moreover, τ_{eff} decreases when the a-SiO$_x$:H layer thickness is reduced. The thickness dependence of τ_{eff}

Intrinsic stack   Device structure   p-type structure

Figure 6.3: Schematic representation of the three structures on which the effective lifetime (τ_{eff}) is investigated, the intrinsic stack and two structures with doped layers. In the p-type structure the top intrinsic layer was omitted and for the bottom intrinsic layer a 7 nm thick hydrogenated amorphous silicon layer was used.
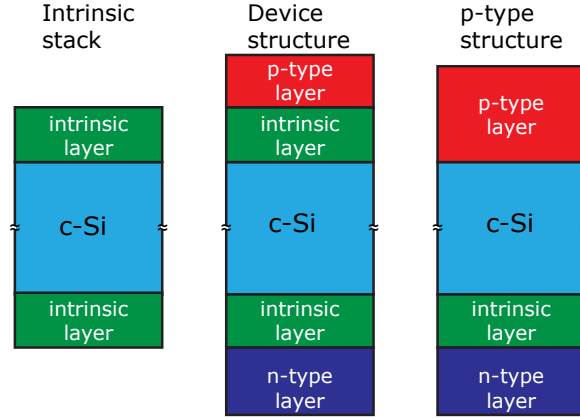
for a-Si:H has been explained elsewhere by taking into account the minority carriers holes recombining at the external (a-Si:H) surface [167]. It is expected that the a-SiO$_x$:H external surface will have a similar effect showing a similar τ_{eff} thickness dependence. When $f_{\text{CO}_2} > 0.66$ a thickness dependence can be still observed but much shorter τ_{eff} are measured. The decrease in passivation quality with increasing oxygen content is in line with what is observed in previous studies [154–156, 158]. This decrease can be explained by an increase in the defect density in the a-SiO$_x$:H/c-Si interface and/or the bulk a-SiO$_x$:H layer with increasing f_{CO_2}, leading to insufficient passivation. Subsequently, all the samples shown in Figure 6.4 (a) were etched down to a thickness of approximately 7 nm and the p- and n-type layers were deposited immediately, making the device structure.

τ_{eff} as a function of c_O for the samples after the p- and n-type layer deposition can be seen in Figure 6.4 (b). τ_{eff} of the device structure is compared with τ_{eff} of the intrinsic stack before the final etch and after the p- and n-type layer deposition. From this comparison, two distinct regions can be identified. In the first region (i.e. for $c_O < 6$ at. %), τ_{eff} decreases after the doped layer deposition. It has been shown that whereas a very thin intrinsic a-Si:H passivation layer can yield very low surface recombination velocities, when the film is subsequently covered with a p-type a-Si:H layer
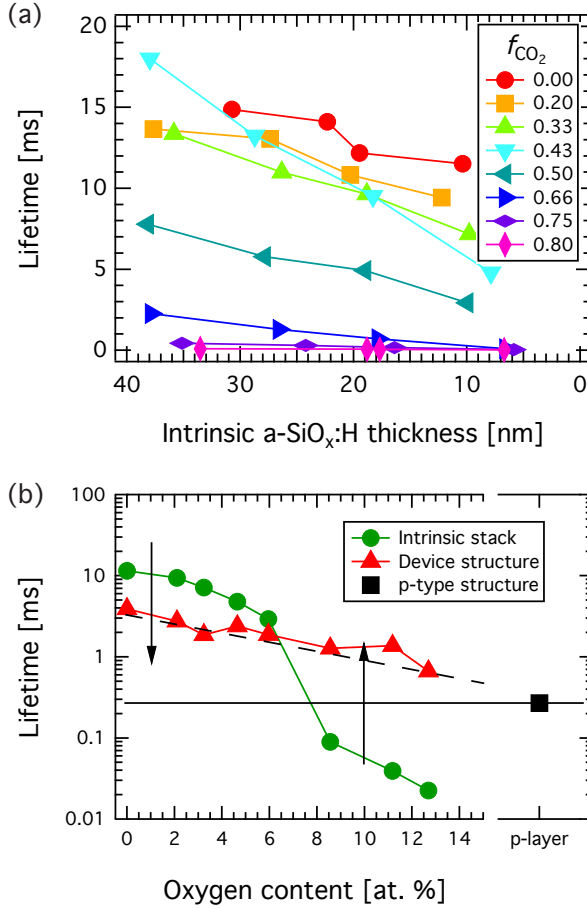
Figure 6.4: (a) Thickness-dependence of the effective lifetime (τ_{eff}) at injection level $1 \times 10^{15}\,\mathrm{cm}^{-3}$ for samples with hydrogenated amorphous silicon oxide (a-SiO$_x$:H) passivation layers deposited with different gas flow ratio $f_{\mathrm{CO_2}}$. $f_{\mathrm{CO_2}}$ is given in Equation (6.1). The x-axis is reversed to indicate the reduction of the thickness due to the etching of the layers. (b) τ_{eff} at injection level $1 \times 10^{15}\,\mathrm{cm}^{-3}$ for samples symmetrically passivated with a-SiO$_x$:H layers of different oxygen content (i.e. the intrinsic stack with green circles), after the doped layer deposition (i.e. the device structure with red triangles) and when the top intrinsic layer is omitted (i.e. the p-type structure with black square). The black lines serve as a guide for the eye, showing the decrease in the device structure τ_{eff} (black dashed line) and τ_{eff} of the p-type structure (black solid line).

the passivation properties are deteriorating, reflected in a decreased τ_{eff} [151]. Deposition of the doped layers is expected to induce an electric field, yielding some field-effect passivation. However, it is often found that this is not the case and the passivation properties of stacks with doped layers are inferior to the passivation properties of stacks with intrinsic layers [135, 178, 179]. The field-effect passivation for the recombination through defects can be understood as follows: The recombination process facilitated by defects in the bulk of the intrinsic a-SiO$_x$:H layer is described by the Shockley-Read-Hall recombination theory [10]. According to this theory the recombination rate is proportional to ($pn - n_i^2$), where p and n are the concentrations for holes and electrons, respectively and n_i is the intrinsic carrier concentration. Therefore, strongly reducing one type of charge carrier in the defect-rich region could provide field-effect passivation by reducing the recombination rate and thus increasing τ_{eff}. Additionally, recombination at the external surfaces [167] or the a-SiO$_x$:H/c-Si interface may also have an influence and it will be described in an almost identical way [180, 181]. Evidently, the field-effect passivation does not play a dominant role in determining τ_{eff} in the region where $c_O < 6$ at. %.

De Wolf et al. [151] suggested that the reason for the decrease observed in τ_{eff} is the recombination occurring at the doped layer instead of the a-Si:H/c-Si interface, with the defect rich p-type layer being an effective recombination channel for the minority carriers. Moreover, it was shown that interface recombination in the presence of the doped layer may result from a Fermi energy dependent generation of defects [135]. This was attributed to amphoteric silicon dangling bonds resulting from Si-H rapture, as was evidenced from hydrogen effusion experiments [135, 177]. Furthermore, since the experiments presented in this work are performed on n-type c-Si wafers an electric field will exist attracting the minority carrier holes towards the interface, once the p-type layer is deposited. This electric field could further contribute in decreasing τ_{eff}.

In the second region (i.e. for $c_O > 6$ at. %), τ_{eff} interestingly increases after the doped layer deposition. In this case the field-effect passivation provided by the doped layers appears to have a prominent role. The induced electric field by the doped layers will repel either holes or electrons from the defective regions, characterized by increased recombination activity. Specifically, the n-type layer will provide field-effect passivation in addition to the chemical passivation, by repelling minority carrier holes. It has been observed that n-type wafers symmetrically passivated with stacked intrinsic and n-type layers can show higher τ_{eff} than wafers pas-

sivated with just intrinsic layers [135]. In this way recombination in the n-type surface region can be reduced or virtually switched off, resulting in an increased τ_{eff}. Sproul [143] presented an approximation for the surface lifetime (τ_{surf}) when the surface recombination velocity of the two surfaces of the wafer is the same and when the surface recombination velocity of one of the two surfaces is zero. In this way τ_{eff} can be calculated if the bulk lifetime (τ_{bulk}) is known through

$$\frac{1}{\tau_{eff}} = \frac{1}{\tau_{bulk}} + \frac{1}{\tau_{surf}}, \qquad (6.2)$$

when the surface recombination velocity is the same at the two surfaces of the wafer, τ_{surf} is given by

$$\tau_{surf} = \frac{W}{2S} + \frac{1}{D}\left(\frac{W}{\pi}\right)^2. \qquad (6.3)$$

In Equation (6.3) W is the wafer thickness, S the surface recombination velocity and D the diffusion constant. Assuming that the surface recombination velocity in the region where the p-type layer is deposited is S_1 and in the region where the n-type layer is deposited is S_2, and assuming the extreme case in which $S_2 = 0$, Equation (6.3) becomes

$$\tau_{surf} = \frac{W}{S_1} + \frac{4}{D}\left(\frac{W}{\pi}\right)^2. \qquad (6.4)$$

The graphical solution for Equation (6.2), using Equation (6.3) and Equation (6.4) is shown in Figure 6.5. To solve for τ_{eff}, it is assumed that τ_{bulk} is equal to 20 ms, while W and D are 280 µm and 11.97 cm^2 s^{-1}, respectively. In Figure 6.5 it can be seen that indeed τ_{eff} increases when S_2 decreases. Using the results presented in Figure 6.5 we can predict the increase in τ_{eff} due to an additional decrease in S_2 after the n-type layer deposition (as shown in Figure 6.4 (b)). τ_{eff} in Figure 6.4 (b) increases when the doped layers are deposited for the samples with $c_O > 6$ at. %. Before the doped layer deposition, these samples show τ_{eff} in the range $0.01 < \tau_{eff} < 0.1$ ms. This range of τ_{eff} for symmetrically passivated wafers with intrinsic a-SiO$_x$:H layers ($S = S_1 = S_2$) corresponds to $100 < S < 10\,000$ cm s^{-1} (grey region in Figure 6.5). It can be clearly seen in Figure 6.5, that even by assuming the extreme case in which S_2 becomes zero after the deposition of the n-type layer, the increase in τ_{eff} observed in Figure 6.4 (b) cannot be explained.

Although an increase in τ_{eff} with the reduction of S_2 can be expected, an additional effect is necessary to explain the increase observed in the results shown in Figure 6.4 (b). We suggest that this additional effect is a decrease in S_1.
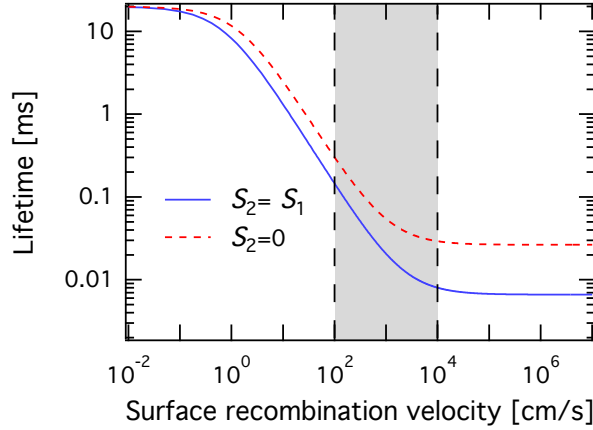

Figure 6.5: Calculated effective lifetime for a wafer having the same surface recombination velocity at the two sides (blue solid line) and for a wafer with the surface recombination velocity at one of the sides set to zero (red dashed line). The range $100 < S < 10\,000 \, \text{cm}\,\text{s}^{-1}$ is indicated with the grey region.

The origin of the decrease in S_1 can be hydrogenation of the passivation layer during the p-type layer deposition and/or the field-effect passivation provided by the p-type layer. A reduction of S_1 could possibly originate from additional hydrogenation and defect reduction of the intrinsic a-SiO$_x$:H layer and a-SiO$_x$:H/c-Si interface [156] or through hydrogen diffusion and redistribution in the intrinsic layer due to the shift in Fermi level after doped layer deposition [182]. However, neither of these effects are likely to be the case for the samples shown in Figure 6.4 (b). In this work, there was a prolonged plasma exposure depositing the initially thicker intrinsic passivation layers with similar and relatively high c_{H} (it can be seen in Figure 6.2 (a) that $c_{\text{H}} \sim 21$ at. %). Moreover, as shown in Table 6.1 no additional hydrogen flow was used for the doped layers. It is therefore not expected that the doped layer deposition further hydrogenates the a-SiO$_x$:H/c-Si interface and/or the a-SiO$_x$:H layer, resulting in defect density reduction and increase in τ_{eff}. In Figure 6.4 (b) τ_{eff} of the structure in which the top intrinsic layer was omitted can be seen. It is

shown that although this structure has shorter τ_{eff} compared to the device structures, τ_{eff} is still higher than for the stacks with only intrinsic a-SiO$_x$:H layer when $c_{\text{O}} > 6$ at. %. This result shows that when the intrinsic layer is characterized by an increased defect density and therefore shorter τ_{eff}, the deposition of the doped layer is able to provide a level of field- effect passivation increasing τ_{eff}. Nevertheless, also for the device structure a decrease in τ_{eff} can be observed with increasing c_{O} of the intrinsic a-SiO$_x$:H layer (shown in Figure 6.4 (b) with black dashed line). This decrease is attributed to an increase in the defect density of the a-SiO$_x$:H layer with c_{O} leading into increased recombination losses and therefore slightly shorter τ_{eff}. As shown in Figure 6.4 (b), τ_{eff} is predominantly determined by the p-type layer and is less dependent on c_{O}. The lowest limit with the doped layers for τ_{eff} (shown in Figure 6.4 (b) with black solid line) appears to be the p-type structure, in which the a-SiO$_x$:H is omitted entirely and essentially replaced by p-type a-Si:H layer. This is not surprising since it is known that doped layers are characterized by an increased defect density [179, 183].

6.4 Conclusion

In conclusion, using our deposition conditions an increase in the optical band gap with c_{O} is observed in the deposited layers, indicating that the layers become more transparent. For the layers with c_{O} less or equal than 6 at. % we are able to obtain τ_{eff} above 5 ms, when only an intrinsic a-SiO$_x$:H is deposited. For c_{O} higher than 6 at. % a rapid decrease in τ_{eff} is observed. This decrease is presumably due to an increase in the defect density of the a-SiO$_x$:H passivation layer and the a-SiO$_x$:H/c-Si interface with c_{O}. When the passivation layer thickness is reduced and the doped layers are deposited τ_{eff} appears to be strongly determined by the doped layers themselves and less dependent on the c_{O} content of the a-SiO$_x$:H passivation layers. Results suggest that τ_{eff} is determined by a field effect induced from the doped layers rather than a chemical effect i.e. defect density increase or reduction due to the deposition of the doped layers.

7

Conclusions and recommendations

In this thesis various aspects regarding the silicon heterojunction (SHJ) solar cell passivation and fabrication have been discussed. In Chapter 3, the texturing and efficient cleaning of the crystalline silicon (c-Si) wafer with a pre-deposition treatment is discussed. Subsequently, in Chapter 4 the passivation of this wafer with intrinsic hydrogenated amorphous silicon (a-Si:H) is investigated. Chapter 5 aims to give a better understanding of the a-Si:H thickness dependent passivation mechanism of c-Si passivated with a-Si:H. Finally, in Chapter 6 the passivation properties of hydrogenated amorphous silicon oxide layers (a-SiO$_x$:H) on c-Si for solar cells are investigated. This chapter summarizes the main conclusions of this thesis and gives suggestions for future work on this topic.

7.1 Conclusions

This thesis focuses on the passivation of crystalline silicon (c-Si) for the fabrication of silicon heterojunction (SHJ) devices. For this purpose, important processing steps as well as fundamental aspects related to passivation have been investigated.

Chapter 3 explores some of the wet-chemical procedures commonly used for cleaning c-Si wafers after texturing, before the passivation and device fabrication. Moreover, it compares these cleaning procedures to an oxidation and oxide removal approach that aims to remove not only contaminants, but also nanometer scaled roughness from the surface of the wafer. For the oxidation and oxide removal nitric acid (HNO_3) and hydrofluoric acid (HF) were used, respectively. The efficiency of the cleaning procedure is evaluated by measuring the excess minority carrier effective lifetime (τ_{eff}) of wafers passivated with intrinsic hydrogenated amorphous silicon (a-Si:H). The oxidation with HNO_3 and subsequent oxide removal shows the best passivation results compared to all the other cleaning methods investigated in this thesis, as reflected in the measured τ_{eff}. It is suggested that the improvement in passivation is not only due to the efficient removal of contaminants but also due to the efficient removal of nanometer scaled roughness from the surface of the c-Si wafer. Moreover, a significant decrease in τ_{eff} is observed when the a-Si:H passivation layer thickness drops below 4 nm. It is expected that the c-Si surface morphology influences the homogeneity of the deposited a-Si:H layer and therefore also τ_{eff}. Therefore sufficient a-Si:H layer thickness must be ensured to avoid low τ_{eff}.

Chapter 4 investigates the passivation of c-Si with a-Si:H by varying the a-Si:H deposition conditions and therefore altering the a-Si:H layer properties. As a result of this investigation, excellent surface passivation is demonstrated when the a-Si:H layers are deposited in a high pressure and high hydrogen dilution regime. It is shown that there is a weak dependence of τ_{eff} on the hydrogen (H_2) dilution, and a strong dependence on the substrate temperature, with τ_{eff} in the order of 10 ms obtained for c-Si wafers passivated with a-Si:H layers with different nanostructures. It is expected that during these hydrogenated plasma conditions additional H increases the hydrogen content at the interface during deposition, while simultaneously etching the layer. The additional H reduces the defect density at the interface, while the etching of the layer prevents void formation during a-Si:H growth thus resulting in a layer with increased density.

For a sample deposited in the high pressure and high hydrogen dilution regime but at lower temperature (i.e. 100 °C), τ_{eff} increases from 20 µs to 10 ms upon annealing at 240 °C. This increase is remarkable and the origin is not completely clear. By investigating the samples using Raman spectroscopy and spectroscopic ellipsometry no significant changes were observed, pointing towards a local redistribution of the a-Si:H network and/or the interface.

Chapter 5 explores the a-Si:H thickness dependency of τ_{eff} on c-Si substrates passivated with a thin layer of intrinsic a-Si:H. To investigate the thickness dependency, an etching method is introduced and used to reduce the thickness of a-Si:H layers that passivates a c-Si substrate. It is shown with these experiments that there is a strong a-Si:H layer thickness dependency of τ_{eff}. Moreover, by reducing the thickness of the passivation layer using a soft wet-etching method it is concluded that the observed thickness dependency is a direct effect of the thickness of the passivation layer. In this way plasma induced changes in the layer during growth that can affect τ_{eff} can be excluded. The results give insight on what determines τ_{eff} when c-Si is passivated with thin a-Si:H layers. It is shown that for thin a-Si:H passivation layers τ_{eff} is mainly influenced by the recombination at the external a-Si:H surface i.e. the air/a-Si:H interface, while for thick a-Si:H passivation layers τ_{eff} is predominantly determined by the bulk a-Si:H defect density and/or the bulk c-Si wafer defect density. These results should be taken into account in relevant passivation studies. Furthermore, it is observed that τ_{eff} decreases faster when the passivation layer thickness drops below 10 nm. This faster decrease is attributed to a gradient in band gap of the a-Si:H layer, and therefore also ΔE_{v}, created during the initial stages of the growth due to structural changes in the a-Si:H layer. By using simulations and altering the band gap of the a-Si:H passivation layer it is found that a decrease in the band gap and therefore also ΔE_{v} will influence τ_{eff} of structures with passivation layers in the complete thickness range investigated in this work. Finally, solar cells were fabricated by depositing initially thicker passivation layers and subsequently reducing the passivation layer thickness. The goal in depositing initially thicker passivation layers was to investigate the effect of the prolonged plasma exposure in the external parameter of the final SHJ solar cell. In this case no improvement was observed in the external parameters of the SHJ solar cell. When the SHJ solar cell is fabricated the passivation, as reflected in V_{OC}, appears to be determined by the doped layer presence. Using the approach of depositing thicker passivation layer and subsequently reduc-

ing the a-Si:H layer thickness, SHJ solar cells with V_{OC}s above $715\,mV$ are obtained for $280 \pm 20\,\mu m$ wafer thickness.

In Chapter 6 hydrogenated amorphous silicon oxide layers (a-SiO$_x$:H) with varying oxygen content (c_O) and similar hydrogen content are used to passivate crystalline silicon wafers. Using our deposition conditions an τ_{eff} of $5\,ms$ is obtained for $c_O \leqslant 6\,at.\,\%$, for passivation layers with thickness of $36 \pm 2\,nm$. The thickness of the layers is subsequently reduced to $7\,nm$ and p- and n-type doped layers are deposited fabricating a solar cell structure. The deposition of the doped layers gives an insight on the passivation mechanism, which appears to be determined by field-effect rather than by chemical passivation. After the deposition of the doped layers, τ_{eff} appears to be predominantly determined by the doped layers themselves and is less dependent on the c_O of the a-SiO$_x$:H layers.

7.2 Recommendations for further research

In Chapter 3, the passivation of textured c-Si wafers is investigated. It is suggested that the influence of the cleaning treatment in the measured τ_{eff} of textured wafers passivated with a-Si:H is not only related to c-Si contamination removal but also to the smoothening of the wafer surface. Ideally, textured wafers with atomically flat facets of the pyramidal structures should be used in the fabrication of SHJ solar cells. It would be beneficial if the roughness on the facets of the pyramids is already controlled during the texturing step. Therefore it would be very useful to explore the texturing step in order to improve the surface morphology and to correlate the surface morphology to the resulting τ_{eff}.

In Chapter 4, excellent surface passivation of c-Si with a-Si:H is demonstrated. However, this passivation is demonstrated only on polished wafers with <111> surface orientation. Typically, for high efficiency SHJ solar cells the use of textured wafers is necessary to ensure an increased short circuit current density. Ideally, the surface of the textured wafer is covered with pyramids that have facets with <111> surface orientation. However, roughness results in surfaces with orientations other than <111> that could influence τ_{eff} under the strong dilution conditions used in Chapter 4 for the deposition of the a-Si:H passivation layer. The deposition conditions used in Chapter 4 should be applied and studied on textured substrates to realize SHJ solar cells with good performance. Moreover, for some of the passivated c-Si wafers shown in Chapter 4 a significant increase in the

τ_{eff} was observed after a post-deposition annealing step, while there were no changes in Raman spectroscopy and SE measurements. Further studying of such observations could give better understanding of the underlying passivation mechanism. For this purpose, a suggested technique that could be sensitive enough is Fourier-transform photocurrent spectroscopy. Additionally, a model [184] can be used to determine the density of states from the data obtained from Fourier-transform photocurrent spectroscopy measurements.

In Chapter 5 a wet-etching method is used to reduce the thickness of the a-Si:H passivation layer with nanometer accuracy. This study is conducted on double-side polished wafers for the sake of simplicity and reproducibility. Conducting a similar study on textured wafers passivated with intrinsic a-Si:H will provide insights on the critical intrinsic layer thickness at which the passivation starts to deteriorate. Moreover, in Chapter 5 an abrupt decrease in τ_{eff} is observed when the layer becomes thinner than 10 nm. This decrease has been attributed to a gradient in band gap and a decrease of ΔE_{v}. This abrupt decrease can be investigated further by altering the deposition conditions of the a-Si:H passivation layer, passivating c-Si with intrinsic a-Si:H with different band gaps. Such investigation can give further insights on the charge transport and passivation mechanism.

In Chapter 6 the passivation properties of intrinsic a-SiO$_x$:H layers with increasing c_{O} are investigated and an increase in the optical gap is observed. The benefit of this increase in the short circuit current density of a SHJ solar cell can be quantified by means of optical simulations. Moreover an increase in τ_{eff} is observed for c-Si wafers passivated with intrinsic a-SiO$_x$:H, after the deposition of the doped layers when the intrinsic a-SiO$_x$:H passivation layers have $c_{\text{O}} > 6$ at. %. This effect should be investigated further by using the etching method described in Chapter 5 to subsequently remove the doped layers. When the τ_{eff} is being determined by the doped layers themselves a decrease in τ_{eff} should be observed, as it is expected from the results shown in Chapter 6.

Bibliography

[1] E. Anders and N. Grevesse, Geochimica et Cosmochimica Acta **53**, 197 (1989).

[2] A. A. Yaroshevsky, Geochemistry International **44**, 48 (2006).

[3] J. Bardeen and W. H. Brattain, Physical Review **74**, 230 (1948).

[4] A. E. Becquerel, Comptes Rendus de l'Académie des Sciences **9**, 561 (1839).

[5] W. G. Adams and R. E. Day, Proceedings of the Royal Society **A 25**, 113 (1877).

[6] C. E. Fritts, American Journal of Science **26**, 465 (1883).

[7] L. Bergmann, Physikalische Zeitschrift **32**, 286 (1931).

[8] L. O. Grondahl, Reviews of Modern Physics **5**, 141 (1933).

[9] F. C. Nix and A. W. Treptow, Journal of the Optical Society of America **29**, 457 (1939).

[10] W. Shockley, Bell Syst. Tech. J. **28**, 435 (1949).

[11] D. M. Chapin, C. S. Fuller, and G. L. Pearson, Journal of Applied Physics **25**, 676 (1954).

[12] R. C. Chittick, J. H. Alexander, and H. F. Sterling, Journal of The Electrochemical Society **116**, 77 (1969).

[13] W. E. Spear and P. G. Le Comber, Solid State Communications **17**, 1193 (1975).

[14] D. E. Carlson and C. R. Wronski, Applied Physics Letters **28**, 671 (1976).

[15] W. Fuhs, K. Niemann, and J. Stuke, AIP Conference Proceedings **20**, 345 (1974).

[16] K. Okuda, H. Okamoto, and Y. Hamakawa, Japanese Journal of Applied Physics **22**, L605 (1983).

[17] M. Tanaka, M. Taguchi, T. Matsuyama, T. Sawada, S. Tsuda, S. Nakano, H. Hanafusa, and Y. Kuwano, Japanese Journal of Applied Physics **31**, 3518 (1992).

[18] M. A. Green, K. Emery, Y. Hishikawa, W. Warta, E. D. Dunlop, D. H. Levi, and A. W. Y. Ho-baillie, Progress in Photovoltaics: Research and Applications **25**, 3 (2017).

[19] M. A. Green, Progress in Photovoltaics: Research and Applications **25**, 3 (2017).

[20] C. Fröhlich and J. Lean, Astronomy and Astrophysics Review **12**, 273 (2004).

[21] J. Jean, P. R. Brown, R. L. Jaffe, T. Buonassisi, and V. Bulovic, Energy and Environmental Science **8**, 1200 (2015).

[22] M. Z. Jacobson and M. A. Delucchi, Energy Policy **39**, 1154 (2011).

[23] *Key world energy statistics*, Tech. Rep. (International Energy Agency, 2016).

[24] *Photovoltaics report*, Tech. Rep. July (Fraunhofer Institute for Solar Energy Systems, ISE, 2017).

[25] *Energy Technology Perspectives*, Tech. Rep. (International Energy Agency, 2008).

[26] *Technology roadmap:Solar photovoltaic energy*, Tech. Rep. (International Energy Agency, 2014).

[27] R. Singh, Journal of Nanophotonics **3**, 032503 (2009).

[28] M. A. Green, K. Emery, Y. Hishikawa, W. Warta, and E. D. Dunlop, Progress in Photovoltaics: Research and Applications **24**, 905 (2016).

[29] P. Würfel, in *Physics of Solar Cells* (WILEY-VCH, Weinheim, 2005) pp. 137–151.

[30] J. Nelson, in *The physics of solar cells* (Imperial College Press, London, 2004) Chap. 6, pp. 145–176.

[31] M. Taguchi, A. Yano, S. Tohoda, K. Matsuyama, Y. Nakamura, T. Nishiwaki, K. Fujita, and E. Maruyama, IEEE Journal of Photovoltaics **4**, 96 (2014).

[32] D. Adachi, J. L. Hernández, and K. Yamamoto, Applied Physics Letters **107**, 233506 (2015).

[33] J. E. Cotter, J. H. Guo, P. J. Cousins, M. D. Abbott, F. W. Chen, and K. C. Fisher, IEEE Transactions on Electron Devices **53**, 1893 (2006).

[34] A. Descoeudres, Z. C. Holman, L. Barraud, S. Morel, S. De Wolf, and C. Ballif, IEEE Journal of Photovoltaics **3**, 83 (2013).

[35] C. Battaglia, A. Cuevas, and S. De Wolf, Energy and Environmental Science **9**, 1552 (2016).

[36] D. Muñoz, T. Desrues, and P.-J. Ribeyron, in *Physics and Technology of Amorphous-Crystalline Heterostructure Silicon Solar Cells*, edited by W. G. van van Sark, L. Korte, and F. Roca (Springer, Berlin, 2012) Chap. 17, pp. 539–572.

[37] S. Sze and K. Kwok, in *Physics of Semiconductor Devices* (Wiley, New York, 2007) 3rd ed., Chap. Photodetec, pp. 663–742.

[38] M. J. Kerr, A. Cuevas, and P. Campbell, Progress in Photovoltaics: Research and Applications **11**, 97 (2003).

[39] A. Richter, M. Hermle, and S. W. Glunz, IEEE Journal of Photovoltaics **3**, 1184 (2013).

[40] D. Diouf, J.-P. Kleider, and C. Longeaud, in *Physics and Technology of Amorphous-Crystalline Heterostructure Silicon Solar Cells*, edited by W. G. van van Sark, L. Korte, and F. Roca (Springer, 2012) Chap. 15, pp. 483–519.

[41] K. A. Reinhardt and W. Kern, eds., *Handbook of Silicon Wafer Cleaning Technology*, 2nd ed. (William Andrew Publishing, Norwich, NY, 2008) pp. 3 – 722.

[42] D. Zhang, *Surface passivation and optical design of silicon heterojunction solar cells*, Ph.D. thesis, Delft University of Technology (2015).

[43] H. Angermann, W. Henrion, M. Rebien, and A. Röseler, Solid State Phenomena **92**, 179 (2003).

[44] D. Gräf, M. Grundner, and R. Schulz, Journal of Vacuum Science & Technology A **7**, 808 (1989).

[45] M. Grundner and R. Schulz, AIP Conference Proceedings **167**, 329 (1988).

[46] G. S. Higashi, Y. J. Chabal, G. W. Trucks, and K. Raghavachari, Applied Physics Letters **56**, 656 (1990).

[47] D. Zhang, A. Tavakoliyaraki, Y. Wu, R. A. C. M. M. van Swaaij, and M. Zeman, Energy Procedia **8**, 207 (2011).

[48] S. K. Saha, R. S. Howell, and M. K. Hatalis, Journal of The Electrochemical Society **146**, 3134 (1999).

[49] H.-N. Lee, J.-C. Park, H.-J. Kim, and W.-G. Lee, Japanese Journal of Applied Physics **41**, 791 (2002).

[50] G. Papakonstantinou, *Investigation and optimization of the front metal contact of silicon heterojunction solar cells*, Ph.D. thesis, Delft University of Technology (2014).

[51] S. Rein, *Lifetime Spectroscopy - A Method of Defect Characterization in Silicon for Photovoltaic Applications* (Springer, Heidelberg, 2005) pp. 5–58.

[52] R. A. Sinton and A. Cuevas, Applied Physics Letters **69**, 2510 (1996).

[53] H. Nagel, C. Berge, and A. G. Aberle, Journal of Applied Physics **86**, 6218 (1999).

[54] S. Marsillac, M. N. Sestak, J. Li, and R. W. Collins, in *Advanced Characterization Techniques for Thin Film Solar Cells*, edited by D. Abou-Ras, T. Kirchartz, and U. Rau (WILEY, Weinheim, 2011) Chap. 6, p. 125149.

[55] A. S. Ferlauto, G. M. Ferreira, J. M. Pearce, C. R. Wronski, R. W. Collins, X. Deng, and G. Ganguly, Journal of Applied Physics **92**, 2424 (2002).

[56] J. Price, P. Y. Hung, T. Rhoad, B. Foran, and A. C. Diebold, Applied Physics Letters **85**, 1701 (2004).

[57] M. H. Brodsky, M. Cardona, and J. J. Cuomo, Physical Review B **16**, 3556 (1977).

[58] G. Lucovsky and W. B. Pollard, Journal of Vacuum Science & Technology A **1**, 313 (1983).

[59] G. Lucovsky, R. J. Nemanich, and J. C. Knights, Physical Review B **19**, 2064 (1979).

[60] M. Pesola, J. von Boehm, T. Mattila, and R. M. Nieminen, Physical Review B **60**, 11449 (1999).

[61] M. Pesola, J. von Boehm, and R. M. Nieminen, Physical Review Letters **82**, 4022 (1999).

[62] D. V. Tsu, G. Lucovsky, and B. N. Davidson, Physical Review B **40**, 1795 (1989).

[63] G. Lucovsky and D. V. Tsu, Journal of Vacuum Science & Technology A **5**, 2231 (1987).

[64] A. A. Langford, M. L. Fleet, B. P. Nelson, W. A. Lanford, and N. Maley, Physical Review B **45**, 13367 (1992).

[65] G. Lucovsky, J. Yang, S. S. Chao, J. E. Tyler, and W. Czubatyj, Physical Review B **28**, 3225 (1983).

[66] J. Alvarez-Garcia, V. Izquierdo-Roca, and A. Perez-Rodriguez, in *Advanced Characterization Techniques for Thin Film Solar Cells*, edited by D. Abou-Ras, T. Kirchartz, and U. Rau (WILEY-VCH, Weinheim, 2011) Chap. 14, pp. 365–386.

[67] J. E. Smith, M. H. Brodsky, B. L. Crowder, M. I. Nathan, and A. Pinczuk, Physical Review Letters **26**, 642 (1971).

[68] Z. Iqbal and S. Veprek, J. Phys. C: Solid State Physics **15**, 377 (1982).

[69] V. A. Volodin and D. I. Koshelev, Journal of Raman Spectroscopy **44**, 1760 (2013).

[70] T. Kirchartz, K. Ding, and U. Rau, in *Advanced Characterization Techniques for Thin Film Solar Cells*, edited by D. Abou-Ras, T. Kirchartz, and U. Rau (WILEY-VCH, Weinheim, 2011) Chap. 2, pp. 35–60.

[71] W. G. J. H. M. van Sark, L. Korte, and F. Roca, eds., *Springer* (Springer, 2012) pp. XXII, 582.

[72] H. Angermann, W. Henrion, A. Röseler, and M. Rebien, Materials Science and Engineering B **73**, 178 (2000).

[73] H. Angermann, W. Henrion, M. Rebien, and A. Röseler, Applied Surface Science **235**, 322 (2004).

[74] H. Angermann, Applied Surface Science **254**, 8067 (2008).

[75] H. Angermann, J. Rappich, L. Korte, I. Sieber, E. Conrad, M. Schmidt, K. Hübener, J. Polte, and J. Hauschild, Applied Surface Science **254**, 3615 (2008).

[76] H. Angermann, F. Wünsch, M. Kunst, A. Laades, U. Stürzebecher, E. Conrad, L. Korte, and M. Schmidt, Physica Status Solidi C **8**, 879 (2011).

[77] H. Kobayashi, Asuha, O. Maida, M. Takahashi, and H. Iwasa, Journal of Applied Physics **94**, 7328 (2003).

[78] H. Seidel, L. Csepregi, A. Heuberger, and H. Baumgärtel, Journal of The Electrochemical Society **137**, 3612 (1990).

[79] D. L. King and M. E. Buck, in *Proceeding of 22nd IEEE Photovoltaic Specialist's Conference* (Las Vegas, 1991) pp. 303–308.

[80] O. Tabata, R. Asahi, H. Funabashi, K. Shimaoka, and S. Sugiyama, Sensors and Actuators A **34**, 51 (1992).

[81] I. Zubel and M. Kramkowska, Sensors and Actuators A **93**, 138 (2001).

[82] U. Gangopadhyay, S. K. Dhungel, A. K. Mondal, H. Saha, and J. Yi, Solar Energy Materials and Solar Cells **91**, 1147 (2007).

[83] O. Weiying, Z. Yao, L. Hailing, Z. Lei, Z. Chunlan, D. Hongwei, L. Min, L. Weiming, Z. Jun, and W. Wenjing, Journal of Semiconductors **31**, 106002 (2010).

[84] M. Shikida, K. Sato, K. Tokoro, and D. Uchikawa, Sensors and Actuators A **80**, 179 (2000).

[85] D. Iencinella, E. Centurioni, R. Rizzoli, and F. Zignani, Solar Energy Materials and Solar Cells **87**, 725 (2005).

[86] M. Rosa, M. Allegrezza, M. Canino, C. Summonte, and A. Desalvo, Solar Energy Materials and Solar Cells **95**, 2987 (2011).

[87] A. Merlos, M. Acero, M. H. Bao, J. Bausells, and J. Esteve, Sensors and Actuators A **37-38**, 737 (1993).

[88] E. D. Palik, V. M. Bermudez, and O. J. Glembocki, Journal of The Electrochemical Society **132**, 871 (1985).

[89] D. B. Lee, Journal of Applied Physics **40**, 4569 (1969).

[90] M. Declercq, L. Gerzberg, and J. D. Meindl, Journal of The Electrochemical Society **122**, 545 (1975).

[91] H. F. Schmidt, M. Meuris, P. W. Mertens, A. L. P. Rotondaro, M. M. Heyns, T. Q. Hurd, and Z. Hatcher, Japanese Journal of Applied Physics **34**, 727 (1995).

[92] S. De Wolf and M. Kondo, Applied Physics Letters **90**, 042111 (2007).

[93] K. R. McIntosh and L. P. Johnson, Journal of Applied Physics **105**, 124520 (2009).

[94] D. Zhang, R. A. C. M. M. van Swaaij, and M. Zeman, in *27th European Photovoltaic Solar Energy Conference and Exhibition* (2012) pp. 1482–1485.

[95] T. Mishima, M. Taguchi, H. Sakata, and E. Maruyama, Solar Energy Materials and Solar Cells **95**, 18 (2011).

[96] S. De Wolf, A. Descoeudres, Z. C. Holman, and C. Ballif, Green **2**, 7 (2012).

[97] K. Yoshikawa, H. Kawasaki, W. Yoshida, T. Irie, K. Konishi, K. Nakano, T. Uto, D. Adachi, M. Kanematsu, H. Uzu, and K. Yamamoto, Nature Energy **2**, 17032 (2017).

[98] H. Fujiwara and M. Kondo, Journal of Applied Physics **101**, 054516 (2007).

[99] R. Rizzoli, E. Centurioni, J. Plá, C. Summonte, A. Migliori, A. Desalvo, and F. Zignani, Journal of Non-Crystalline Solids **299-302**, 1203 (2002).

[100] M. Taguchi, K. Kawamoto, S. Tsuge, T. Baba, H. Sakata, M. Morizane, K. Uchihashi, N. Nakamura, S. Kiyama, and O. Oota, Progress in Photovoltaics: Research and Applications **8**, 503 (2000).

[101] J.-W. A. Schuttauf, K. H. M. van der Werf, I. M. Kielen, W. G. J. H. M. van Sark, J. K. Rath, and R. E. I. Schropp, Applied Physics Letters **98**, 153514 (2011).

[102] A. Descoeudres, L. Barraud, R. Bartlome, G. Choong, S. De Wolf, F. Zicarelli, and C. Ballif, Applied Physics Letters **97**, 183505 (2010).

[103] H. C. Neitzert, W. Hirsch, and M. Kunst, Physical Review B **47**, 4080 (1993).

[104] H. Fujiwara, T. Kaneko, and M. Kondo, Solar Energy Materials and Solar Cells **93**, 725 (2009).

[105] C. C. Tsai, G. B. Anderson, and R. Thompson, Journal of Non-Crystalline Solids **137-138**, 673 (1991).

[106] A. Fontcuberta i Morral and P. Roca i Cabarrocas, Journal of Non-Crystalline Solids **299-302**, 196 (2002).

[107] T. F. Schulze, H. N. Beushausen, C. Leendertz, A. Dobrich, B. Rech, and L. Korte, Applied Physics Letters **96**, 252102 (2010).

[108] H. Fujiwara, T. Kaneko, and M. Kondo, Applied Physics Letters **91**, 133508 (2007).

[109] A. Descoeudres, L. Barraud, S. De Wolf, B. Strahm, D. Lachenal, C. Guérin, Z. C. Holman, F. Zicarelli, B. Demaurex, J. Seif, J. Holovsky, and C. Ballif, Applied Physics Letters **99**, 123506 (2011).

[110] M. Mews, T. F. Schulze, N. Mingirulli, and L. Korte, Applied Physics Letters **102**, 122106 (2013).

[111] H. Meddeb, T. Bearda, W. Dimassi, Y. Abdulraheem, H. Ezzaouia, I. Gordon, J. Szlufcik, and J. Poortmans, Physica Status Solidi - Rapid Research Letters **9**, 53 (2015).

[112] J.-W. A. Schuttauf, C. van der Werf, W. van Sark, J. Rath, and R. Schropp, Thin Solid Films **519**, 4476 (2011).

[113] J. Geissbuhler, S. De Wolf, B. Demaurex, J. P. Seif, D. T. L. Alexander, L. Barraud, and C. Ballif, Applied Physics Letters **102**, 231604 (2013).

[114] M. Stuckelberger, M. Despeisse, G. Bugnon, J.-W. Schuttauf, F.-J. Haug, and C. Ballif, Journal of Applied Physics **114**, 154509 (2013).

[115] B. Kalache, A. I. Kosarev, R. Vanderhaghen, and P. Roca i Cabarrocas, Journal of Applied Physics **93**, 1262 (2003).

[116] X. Wu, J. Yu, T. Ren, and L. Liu, Microelectronics Journal **38**, 87 (2007).

[117] A. H. M. Smets and M. C. M. van de Sanden, Physical Review B **76**, 073202 (2007).

[118] R. V. Kruzelecky, D. Racansky, S. Zukotynski, and J. M. Perz, Journal of Non-Crystalline Solids **99**, 89 (1988).

[119] M. Fischer, H. Tan, J. Melskens, R. Vasudevan, M. Zeman, and A. H. M. Smets, Applied Physics Letters **106**, 043905 (2015).

[120] A. H. M. Smets, M. A. Wank, B. Vet, M. Fischer, R. A. C. M. M. van Swaaij, M. Zeman, D. C. Bobela, C. R. Wronski, and R. M. C. M. van de Sanden, IEEE Journal of Photovoltaics **2**, 94 (2012).

[121] S. De Wolf, C. Ballif, and M. Kondo, Physical Review B **85**, 113302 (2012).

[122] J. Melskens, A. H. M. Smets, M. Schouten, S. W. H. Eijt, H. Schut, and M. Zeman, IEEE Journal of Photovoltaics **3**, 65 (2013).

[123] J. C. Knights and G. Lucovsky, Critical Reviews in Solid State and Materials Sciences **9**, 211 (1980).

[124] P. Roca i Cabarrocas, Journal of Non-Crystalline Solids **164-166**, 37 (1993).

[125] F. Wang, X. Zhang, L. Wang, Y. Jiang, C. Wei, S. Xu, and Y. Zhao, Physical Chemistry Chemical Physics **16**, 20202 (2014).

[126] A. Matsuda and K. Tanaka, Journal of Applied Physics **60**, 2351 (1986).

[127] A. Matsuda, M. Takai, T. Nishimoto, and M. Kondo, Solar Energy Materials and Solar Cells **78**, 3 (2003).

[128] F. Kaïl, A. Fontcuberta i Morral, A. Hadjadj, P. Roca i Cabarrocas, and A. Beorchia, Philosophical Magazine **84**, 595 (2004).

[129] A. H. M. Smets, W. M. M. Kessels, and M. C. M. van de Sanden, Applied Physics Letters **82**, 1547 (2003).

[130] K. S. Jones, S. Prussin, and E. R. Weber, Applied Physics A Solids and Surfaces **45**, 1 (1988).

[131] U. K. Das, M. Z. Burrows, M. Lu, S. Bowden, and R. W. Birkmire, Applied Physics Letters **92**, 063504 (2008).

[132] Y. Jiang, X.-d. Zhang, F. Wang, C. Wei, and Y. Zhao, Rsc Advances **4**, 29794 (2014).

[133] C. C. Tsai, G. B. Anderson, R. Thompson, and B. Wacker, Journal of Non-Crystalline Solids **114**, 151 (1989).

[134] D. Deligiannis, R. Vasudevan, A. H. M. Smets, R. A. C. M. M. van Swaaij, and M. Zeman, AIP Advances **5**, 097165 (2015).

[135] S. De Wolf and M. Kondo, Journal of Applied Physics **105**, 103707 (2009).

[136] A. Richter, S. W. Glunz, F. Werner, J. Schmidt, and A. Cuevas, Physical Review B **86**, 165202 (2012).

[137] R. Varache, C. Leendertz, M. E. Gueunier-Farret, J. Haschke, D. Muñoz, and L. Korte, Solar Energy Materials and Solar Cells **141**, 14 (2015).

[138] H. Robbins and B. Schwartz, Journal of The Electrochemical Society **106**, 505 (1959).

[139] S. De Wolf, S. Olibet, and C. Ballif, Applied Physics Letters **93**, 032101 (2008).

[140] K. Jones, *The Chemistry of Nitrogen* (Pergamon Press, Oxford, 1973) pp. 375–388.

[141] J. Weber, S. Knack, O. V. Feklisova, N. A. Yarykin, and E. B. Yakimov, Microelectronic Engineering **66**, 320 (2003).

[142] A. J. Tavendale, A. A. Williams, and S. J. Pearton, in *Materials Research Society symposia proceedings* (1988) p. 285.

[143] A. B. Sproul, Journal of Applied Physics **76**, 2851 (1994).

[144] H. Fujiwara, Y. Toyoshima, M. Kondo, and A. Matsuda, Physical Review B **60**, 13598 (1999).

[145] M. Wank, A. Illiberi, F. D. Tichelaar, R. A. C. M. M. van Swaaij, M. van de Sanden, and M. Zeman, Physica Status Solidi C **7**, 571 (2010).

[146] K. Fukutani, M. Kanbe, W. Futako, B. Kaplan, T. Kamiya, C. M. Fortmann, and I. Shimizu, Journal of Non-Crystalline Solids **227-230**, 63 (1998).

[147] C. G. V. D. Walle and L. H. Yang, Journal of Vacuum Science and Technology B **13**, 1635 (1995).

[148] L. Korte and M. Schmidt, Journal of Applied Physics **109**, 063714 (2011).

[149] T. F. Schulze, L. Korte, F. Ruske, and B. Rech, Physical Review B **83**, 165314 (2011).

[150] I.-S. Chen, T. Jamali-Beh, Y. Lee, C.-Y. Li, and C. R. Wronski, in *First world conference on photovoltaic energy conversion*, Vol. 1 (IEEE, Waikoloa, HI, 1994) pp. 468–471.

[151] S. De Wolf and G. Beaucarne, Applied Physics Letters **88**, 022104 (2006).

[152] D. Zhang, I. A. Digdaya, R. Santbergen, R. A. van Swaaij, P. Bronsveld, M. Zeman, J. A. van Roosmalen, and A. W. Weeber, Solar Energy Materials and Solar Cells **117**, 132 (2013).

[153] Z. C. Holman, A. Descoeudres, L. Barraud, F. Z. Fernandez, J. P. Seif, S. De Wolf, and C. Ballif, IEEE Journal of Photovoltaics **2**, 7 (2012).

[154] J. P. Seif, A. Descoeudres, M. Filipi, F. Smole, M. Topi, Z. C. Holman, S. De Wolf, and C. Ballif, Journal of Applied Physics **115**, 024502 (2014).

[155] M. Liebhaber, M. Mews, T. F. Schulze, L. Korte, B. Rech, and K. Lips, Applied Physics Letters **106**, 031601 (2015).

[156] M. Mews, M. Liebhaber, B. Rech, and L. Korte, Applied Physics Letters **107**, 013902 (2015).

[157] J. Sritharathikhun, H. Yamamoto, S. Miyajima, A. Yamada, and M. Konagai, Japanese Journal of Applied Physics **47**, 8452 (2008).

[158] F. Einsele, W. Beyer, and U. Rau, Journal of Applied Physics **112**, 054905 (2012).

[159] K. Ding, U. Aeberhard, F. Finger, and U. Rau, Journal of Applied Physics **113**, 134501 (2013).

[160] N. Brinkmann, D. Sommer, G. Micard, G. Hahn, and B. Terheiden, Solar Energy Materials and Solar Cells **108**, 180 (2013).

[161] M. W. M. van Cleef, F. A. Rubinelli, R. Rizzoli, R. Pinghini, R. E. I. Schropp, and W. F. van der Weg, Japanese Journal of Applied Physics **37**, 3926 (1998).

[162] M. W. M. van Cleef, R. E. I. Schropp, and F. A. Rubinelli, Applied Physics Letters **73**, 2609 (1998).

[163] D. Pysch, M. Bivour, M. Hermle, and S. W. Glunz, Thin Solid Films **519**, 2550 (2011).

[164] D. Zhang, D. Deligiannis, G. Papakonstantinou, R. A. C. M. M. van Swaaij, and M. Zeman, IEEE Journal of Photovoltaics **4**, 1326 (2014).

[165] M. Boccard and Z. C. Holman, Journal of Applied Physics **118**, 065704 (2015).

[166] W. Beyer, Journal of Non-Crystalline Solids **266-269**, 845 (2000).

[167] D. Deligiannis, V. Marioleas, R. Vasudevan, C. C. G. Visser, R. A. C. M. M. van Swaaij, and M. Zeman, Journal of Applied Physics **119**, 235307 (2016).

[168] J. C. Knights, G. Lucovsky, and R. J. Nemanich, Philosophical Magazine Part B **37**, 467 (1978).

[169] H. Wagner and W. Beyer, Solid State Communications **48**, 585 (1983).

[170] M. Cardona, Physica Status Solidi B **118**, 463 (1983).

[171] W. M. M. Kessels, M. C. M. van de Sanden, R. J. Severens, L. J. van Ijzendoorn, and D. C. Schram, Materials Research Society symposia proceedings **507**, 529 (1998).

[172] D. A. G. Bruggeman, Annalen der Physik Leipzig **24**, 636 (1935).

[173] D. Y. Kim, E. Guijt, R. A. C. M. M. van Swaaij, and M. Zeman, Progress in Photovoltaics: Research and Applications **23**, 671 (2015).

[174] M. A. Paesler, D. A. Anderson, E. C. Freeman, G. Moddel, and W. Paul, Physical Review Letters **41**, 1492 (1978).

[175] G. Lucovsky, Solid State Communications **29**, 571 (1979).

[176] P. John, I. M. Odeh, M. J. K. Thomas, M. J. Tricker, and J. I. B. Wilson, Physica Status Solidi B **105**, 499 (1981).

[177] S. De Wolf and M. Kondo, Applied Physics Letters **91**, 112109 (2007).

[178] M. Taguchi, A. Terakawa, E. Maruyama, and M. Tanaka, Progress in Photovoltaics: Research and Applications **13**, 481 (2005).

[179] L. Korte and M. Schmidt, Journal of Non-Crystalline Solids **354**, 2138 (2008).

[180] A. G. Aberle, Progress in Photovoltaics: Research and Applications **8**, 473 (2000).

[181] S. Olibet, E. Vallat-Sauvain, and C. Ballif, Physical Review B **76**, 035326 (2007).

[182] W. Beyer, J. Herion, and H. Wagner, Journal of Non-Crystalline Solids **114**, 217 (1989).

[183] R. A. Street, Journal of Non-Crystalline Solids **77-78**, 1 (1985).

[184] M. van Sebille, R. A. Vasudevan, R. J. Lancee, R. A. C. M. M. van Swaaij, and M. Zeman, Journal of Physics D: Applied Physics **48**, 325302 (2015).
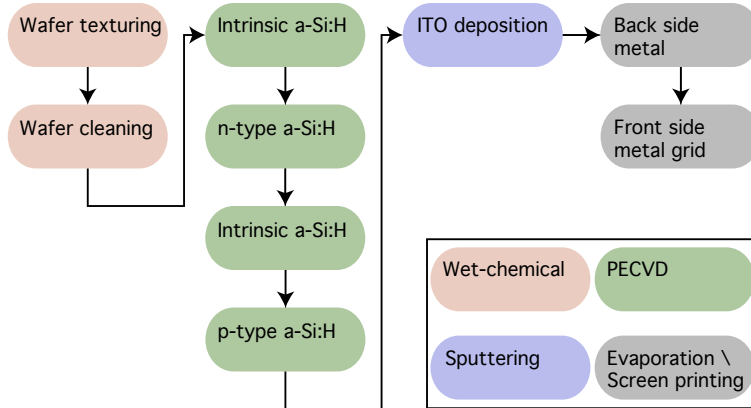
Appendix A

Figure 1: Silicon heterojunction solar cell fabrication flowchart.

Summary

Silicon heterojunction solar cells (SHJ) are currently one of the most promising solar cell technologies in the world. The SHJ solar cell is based on a crystalline silicon (c-Si) wafer, passivated on both sides with a thin intrinsic hydrogenated amorphous silicon (a-Si:H) layer. Subsequently, p-type and n-type doped layers are deposited on the passivated wafer as the emitter and the back surface field of the solar cell. The first study of the a-Si:H/c-Si heterojunction for photovoltaic application was more than 40 years ago. During these years the SHJ solar cell technology has been investigated extensively, approaching the theoretical efficiency limit of single junction silicon solar cells. Although SHJ solar cell technology has been extensively studied and has demonstrated such a good performance, there are still aspects of the device operation not well understood.

This thesis discusses certain aspects of SHJ solar cells and has a main focus on the surface passivation of the c-Si wafer. In this way it aims to contribute to the understanding of SHJ solar cell fabrication and operation, helping to improve the SHJ solar cell performance. This thesis is organized as follows.

In Chapter 1 the historical context for photovoltaic energy conversion is discussed and the SHJ solar cell concept is introduced. This chapter also discusses the motivation for this work. This is followed by Chapter 2 where the general processes used for SHJ sample fabrication and characterization in this work are discussed. Firstly, the processes used for the fabrication of the samples and devices are described. These processes include wafer texturing and cleaning, deposition of the a-Si:H layers, deposition of the TCO, and finally deposition of the metal contacts. Secondly, the various techniques used to characterize the samples and solar cells fabricated in this work are explained.

In Chapter 3 some of the cleaning procedures commonly used to clean the c-Si wafer before the SHJ solar cell fabrication are investigated. The c-Si wafer serves as the absorber layer and can be considered the core of the SHJ solar cell. In order to achieve increased absorption of light in the c-Si wafer and ensure maximum possible J_{SC}, random texturing of the wafer is applied. The process of texturing will have a great impact on the surface of the wafer, on which the a-Si:H layers will be deposited and form the a-Si:H/c-Si interfaces. In this way a damaged surface with increased roughness will result in poor passivation of the c-Si wafer i.e. an a-Si:H/c-

Si interface characterized by increased recombination rate. This increased recombination rate results in a solar cell with a decreased V_{OC}. By applying an appropriate cleaning procedure the roughness on the facets of the pyramidal surface of the c-Si wafer can be reduced, yielding interfaces that do not limit the V_{OC}, after the solar cell fabrication. In Chapter 3, besides investigating commonly used cleaning treatments such as cleaning with nitric acid (HNO_3), RCA, and Piranha, an approach that consists of multiple steps of wet-chemical oxidation using HNO_3 and subsequent oxide removal is applied. Using this approach it is shown that similar passivation on textured and polished substrates can be obtained. The best η achieved on a SHJ solar cell fabricated using a textured substrate is 20.8 %. It is suggested that the effect of the cleaning on the passivation is directly related to the efficient removal of nano-scale roughness from the surface of the c-Si wafer. Besides the surface of the wafer, the deposition conditions and the properties of the resulting a-Si:H layers can significantly impact the passivation of the c-Si wafer and therefore also the SHJ solar cell V_{OC}.

In Chapter 4 the effect of the deposition conditions and the a-Si:H properties on the c-Si passivation are investigated by means of minority carrier effective lifetime (τ_{eff}) measurements. As a result of this investigation, excellent surface passivation is demonstrated by depositing the a-Si:H passivation layers in a high-pressure and high hydrogen dilution deposition regime. The results show a weak dependence of τ_{eff} on hydrogen dilution of the a-Si:H layer, and a strong dependence on the substrate temperature, with τ_{eff} in the order of 10 ms obtained for different a-Si:H nanostructures. The increase in τ_{eff} when using these hydrogen-diluted plasma conditions is explained by extra hydrogenation of the interface during deposition, while simultaneously etching the layer. The etching of the layer prevents void formation during a-Si:H growth thus resulting in a layer with increased density.

The passivation of c-Si is often studied using wafers passivated with thicker intrinsic a-Si:H layers than what is commonly used in SHJ devices. It has been observed that thicker passivation layers can result in higher τ_{eff}, yet the dependence of τ_{eff} on the thickness of the a-Si:H layer has not been investigated in detail so far. In Chapter 5 the a-Si:H thickness dependency of τ_{eff} on c-Si substrates passivated with intrinsic a-Si:H is studied. For this purpose c-Si wafers are passivated with a-Si:H layers thicker than the layers used in SHJ solar cells and a wet-etching method is used to accurately reduce the thickness of the passivation layers and study τ_{eff}. Results show that there is indeed a strong thickness dependency of

the τ_{eff}. During the growth of the layer the deposition conditions can alter the properties of the passivation layer, affecting τ_{eff}. By using the wet-etching method to reduce the thickness of an initially thicker a-Si:H layer it is shown that the increased τ_{eff} with the thickness of the passivation layer is a direct effect of the increased thickness of the layer rather than an effect of the deposition conditions. For thin a-Si:H passivation layers τ_{eff} appears to be mainly influenced by the recombination at the external a-Si:H surface, i.e. the air/a-Si:H interface, while for thick a-Si:H layers τ_{eff} is predominantly determined by the bulk a-Si:H defect density and/or the bulk c-Si wafer defect density. Furthermore, the etching method is used to reduce the thickness of initially thicker passivation layers to about 7 nm and fabricate SHJ solar cells. Using this approach solar cells with V_{OC} above 715 mV are obtained for $280 \pm 20\,\mu\text{m}$ wafer thickness.

Furthermore, the wet-etching approach demonstrated in Chapter 5 is used to study the passivation properties of hydrogenated amorphous silicon oxide layers (a-SiO$_x$:H), passivating c-Si wafers. In Chapter 6 a-SiO$_x$:H with varying oxygen content (c_O) and similar hydrogen content are used to passivate c-Si wafers. Using our deposition conditions an τ_{eff} above 5 ms is obtained for $c_O \leqslant 6\,\text{at.\%}$, for passivation layers with thickness of 36 ± 2 nm. The thickness of the layers is subsequently reduced to $\sim$7 nm and p- and n-type doped layers are deposited fabricating a device structure. The deposition of the doped layers gives an insight on the passivation mechanism, which appears to be determined by the field-effect rather than by chemical passivation. After the deposition of the doped layers, τ_{eff} appears to be predominantly determined by the doped layers themselves and is less dependent on the c_O of the a-SiO$_x$:H layers.

Finally, in Chapter 7 the main conclusions of this work are outlined. In addition, in Chapter 7 some recommendations are given that can help understand better or expand further the work discussed in this thesis.

Samenvatting

De silicium heterojunctie (SHJ) zonneceltechnologie is momenteel één van de meest veelbelovende zonneceltechnologieën ter wereld. De SHJ zonnecel is gebaseerd op een kristallijn silicium (c-Si) wafer die aan beide kanten is gepassiveerd met een dunne laag van intrinsiek gehydrogeneerd amorf silicium (a-Si:H). Hierop worden p-type en n-type gedoteerde lagen gedeponeerd die respectievelijk dienen als emitter en back surface field van de zonnecel. De eerste studie van zulke a-Si:H/c-Si heterojuncties voor fotovoltaïsche toepassing dateert van meer dan 40 jaren geleden. Inmiddels is deze SHJ zonneceltechnologie uitgebreid bestudeerd en benadert het rendement de theoretische limiet. Desalniettemin zijn er nog altijd aspecten van dit type zonnecel die niet goed begrepen zijn.

Dit proefschrift richt zich vooral op de passivering van het oppervlak van de c-Si wafer. Het doel is het verder verbeteren van de SHJ zonnecel door middel van beter begrip van zowel de fabricage als de werking van de SHJ zonnecel. Dit proefschrift is als volgt ingedeeld:

In hoofdstuk 1 wordt de historische context van fotovoltaïsche energie-omzetting beschreven en wordt de SHJ zonnecel geïntroduceerd. Dit hoofdstuk bespreekt ook de motivatie voor dit werk. In hoofdstuk 2 worden vervolgens de gebruikte fabricage- en karakteriseringstechnieken beschreven. Dit omvat de technieken voor textureren en reinigen van wafers en voor het deponeren van a-Si:H, TCO en metaalcontacten. Ook worden de technieken uitgelegd die gebruikt worden voor het karakteriseren van de gemaakte samples en zonnecellen.

In hoofdstuk 3 zijn procedures voor het reinigen van de c-Si wafer onderzocht. Het oppervlak van deze wafer heeft meestal een piramidetextuur om de absorptie van licht, en daarmee de kortsluitstroom J_{SC} van de zonnecel, te vergroten. Deze textuur heeft een grote invloed op het oppervlak waarop de a-Si:H lagen worden gedeponeerd, en daarmee op het gevormde a-Si:H/c-Si interface. Een ruw en beschadigd piramideoppervlak zal resulteren in slechte passivering van de c-Si wafer. Dit resulteert in een verhoogde recombinatiesnelheid aan het a-Si:H/c Si interface en daardoor een lagere open-klemspanning V_{OC} van de zonnecel. Echter, door een speciale reinigingsprocedure te gebruiken kan de ruwheid op de zijdes van de piramides verminderd worden zodat interfaces worden verkregen die de V_{OC} niet beperken. Naast de standaard reinigingsprocedures, zoals met salpeterzuur (HNO_3), RCA en Piranha, is ook een proce-

dure toegepast bestaande uit een herhaling van natte-chemische oxidatie met behulp van HNO_3 en daaropvolgende verwijdering van het gevormde oxide. Met behulp van deze procedure is een passivering van getextureerde oppervlakken verkregen die van even hoge kwaliteit is als de passivering van gepolijste substraten, resulterend in een zonnecel met efficiëntie van 20.8 %. Het lijkt er op dat het effect van de reiniging op de passivering direct verband houdt met de verwijdering van nano-schaal ruwheid aan het oppervlak van de c-Si wafer.

In hoofdstuk 4 is het effect van de depositiecondities en de eigenschappen van het gedeponeerde a-Si:H op de passivering van het c-Si onderzocht. Dit is gedaan door middel van metingen van de effectieve levensduur τ_{eff} van de minderheidsladingsdragers. Met a-Si:H gedeponeerd bij hoge druk en onder hoge waterstofverdunning is een uitstekende oppervlaktepassivering gedemonstreerd. Hiermee is een τ_{eff} in de orde van 10 ms verkregen. De resultaten tonen aan dat τ_{eff} maar weinig afhangt van de waterstofverdunning maar sterk afhangt van de temperatuur van het substraat tijdens de depositie. De toename in τ_{eff} bij het gebruik van deze met waterstof verdunde plasmas wordt verklaard door extra hydrogenering van het interface tijdens de depositie en het gelijktijdig etsen van de laag. Dit etsen voorkomt de vorming van holtes tijdens de groei van a-Si:H, waardoor de dichtheid van deze laag hoger wordt.

De passivering van c-Si met intrinsiek a-Si:H wordt vaak bestudeerd aan de hand van samples met a-Si:H lagen die dikker zijn dan wat in zonnecellen wordt gebruikt. Het is bekend dat dikkere passiveringslagen kunnen resulteren in een hogere τ_{eff}, maar de exacte dikteafhankelijkheid is tot nu toe nog niet in detail onderzocht. Ook kunnen de depositiecondities de groei van de passiveringslaag en daarmee τ_{eff} beïnvloeden. In hoofdstuk 5 worden c-Si wafers gepassiveerd met dikke a-Si:H lagen en wordt een natte-etsmethode gebruikt om de dikte hiervan op gecontroleerde wijze, stap voor stap te verminderen. Deze resultaten laten het effect van puur de laagdikte op τ_{eff} zien, zonder invloed van veranderende depositiecondities. Voor dunne a-Si:H passiveringslagen blijkt τ_{eff} vooral te worden beïnvloed door de recombinatie op het externe a-Si:H oppervlak, d.w.z. de lucht/a-Si:H interface. Voor dikke a-Si:H lagen hangt τ_{eff} overwegend af van de defect dichtheid in de bulk van de a-Si:H laag of de c-Si wafer. De etsmethode is gebruikt om de dikte van aanvankelijk dikkere passiveringslagen terug te brengen tot ongeveer 7 nm en hiermee SHJ zonnecellen te fabriceren. Deze zonnecellen, met een c-Si wafer van 280 ± 20 µm dik, hadden een hoge V_{OC} van 715 mV.

In hoofdstuk 6 wordt de hierboven beschreven aanpak ook gebruikt om de passiveringseigenschappen van gehydrogeneerde amorf siliciumoxide (a-SiO$_x$:H) te bestuderen. Het zuurstofgehalte (c_O) wordt gevarieerd bij constant waterstofgehalte. Met een a-SiO$_x$:H laag met $c_O \leqslant 6$ at. % en een dikte van 36 ± 2 nm is een τ_{eff} verkregen van meer dan 5 ms. Vervolgens is de dikte van de lagen weer gereduceerd tot 7 nm en zijn p- en n-type gedoteerde lagen gedeponeerd om een complete zonnecel te fabriceren. Het blijkt dat τ_{eff} overwegend wordt bepaald door de gedoteerde lagen en minder afhankelijk is van het zuurstofgehalte van de a-SiO$_x$:H lagen. Hieruit blijkt dat het passiveringsmechanisme meer lijkt op veldeffect-passivering dan chemische passivering.

Ten slotte worden in hoofdstuk 7 de belangrijkste conclusies van dit werk samengevat en worden enkele aanbevelingen gedaan voor aanvullingen op en uitbreiding van het hier beschreven werk.

List of publications

This thesis

D. Deligiannis, S. Alivizatos, A. Ingenito, D. Zhang, M. van Sebille, R. A. C. M. M. van Swaaij, and M. Zeman, *Wet-chemical treatment for improved surface passivation of textured silicon heterojunction solar cells*, Energy Procedia 55, 197-202 (2014); DOI: 10.1016/j.egypro.2014.08.117

D. Deligiannis, R. Vasudevan, A. H. M. Smets, R. A. C. M. M. van Swaaij, M. Zeman, *Surface passivation of c-Si for silicon heterojunction solar cells using high-pressure hydrogen diluted plasmas*, AIP Advances 5, 097165 (2015); DOI: 10.1063/1.4931821

D. Deligiannis, V. Marioleas, R. Vasudevan, C. C. G. Visser R. A. C. M. M. van Swaaij and M. Zeman, *Understanding the thickness-dependent effective lifetime of crystalline silicon passivated with a thin layer of intrinsic hydrogenated amorphous silicon using a nanometer-accurate wet-etching method*, Journal of Applied Physics 119, 235307 (2016); DOI: 10.1063/1.4954069

D. Deligiannis, J. van Vliet, R. Vasudevan, C. C. G. Visser R. A. C. M. M. van Swaaij and M. Zeman, *Passivation mechanism in silicon heterojunction solar cells with intrinsic hydrogenated amorphous silicon oxide layers*, Journal of Applied Physics 121, 085306 (2017); DOI: 10.1063/1.4977242

Other publications

D. Zhang, **D. Deligiannis**, G. Papakonstantinou, R. A. C. M. M. van Swaaij, and M. Zeman, *Optical enhancement of silicon heterojunction solar cells with hydrogenated amorphous silicon carbide emitter*, IEEE Journal of Photovoltaics 4, 1326-1330 (2014); DOI: 10.1109/JPHOTOV.2014.2344768

B. Macco, **D. Deligiannis**, S. Smit, R. A. C. M. M. van Swaaij, M. Zeman, and W. M. M. Kessels, *Influence of transparent conductive oxides on passivation of a-Si:H/c-Si heterojunctions as studied by atomic layer deposited Al-doped ZnO*, Semicond. Sci. Technol. 29, 122001 (2014); DOI: 10.1088/0268-

1242/29/12/122001

R. Vasudevan, Z. Thanawala, L. Han, T. Buijs, H. Tan, **D. Deligiannis**, P. Perez-Rodriguez, I. A. Digdaya, W. A. Smith, M. Zeman, A. H. M. Smets, *A thin-film silicon/silicon hetero-junction hybrid solar cell for photoelectrochemical water-reduction applications*, Solar Energy Materials and Solar Cells 150, 82-87 (2016); DOI: 10.1016/j.solmat.2016.02.006

R. Vasudevan, I. Poli, **D. Deligiannis**, M. Zeman, A. H. M. Smets, *Temperature dependency of the silicon heterojunction lifetime model based on the amphoteric nature of dangling bonds*, AIP Advances 6, 115118 (2016); DOI: 10.1063/1.4968604

R. Vasudevan, I. Poli, **D. Deligiannis**, M. Zeman, A. H. M. Smets, *Light-Induced effects on the a-Si:H/c-Si heterointerface*, IEEE Journal of Photovoltaics 7, 656-664 (2016); DOI: 10.1109/JPHOTOV.2016.2633800

Conference and workshop contributions

D. Deligiannis, K. Buisman, D. Zhang, R. A. C. M. M. van Swaaij, and M. Zeman, *Light-induced degradation of heterojunction silicon solar cells with thin intrinsic a-Si:H layers*, poster presentation at EUPVSEC-28, 30 September 2013 - 4 October 2013, Paris, France

K. Sharma, **D. Deligiannis**, J. W. Weber, S. Smit, A. A. Bol, M. C. M. van de Sanden, M. Creatore, R. A. C. M. M. van Swaaij, and W. M. M. Kessels, *Graphene as a transparent front contact for heterojunction silicon solar cells*, oral presentation at AVS, 27 October 2013 1 November 2013, Long Beach, California, USA

D. Deligiannis, S. Alivizatos, A. Ingenito, D. Zhang, M. van Sebille, R. A. C. M. M. van Swaaij, and M. Zeman, *Wet-chemical treatment for improved surface passivation of textured silicon heterojunction solar cells*, poster presentation at SiliconPV, 25-27 March 2014, s-Hertogenbosch, the Netherlands

B. Macco, S. Smit, W. M. M. Kessels, **D. Deligiannis**, R. A. C. M. M. van Swaaij, M. Zeman, *Investigation of TCO-induced band bending in c-Si/a-Si:H/*

ZnO:Al heterostructures and its effect on surface recombination, oral presentation at SiliconPV, 25-27 March 2014, s-Hertogenbosch, the Netherlands

A. Ingenito, **D. Deligiannis**, R. A. C. M. M. van Swaaij, O. Isabella, and M. Zeman, *Opto-electrical approaches to make high efficiency ultra-thin crystalline silicon solar cells*, oral presentation at EUPVSEC-29, 22-26 September 2014, Amsterdam, the Netherlands

B. Macco, **D. Deligiannis**, S. Smit, M. Zeman, R. A. C. M. M. van Swaaij, W. M. M. Kessels, *Improved passivation of SHJ solar cells by atomic layer deposited Al-doped ZnO as transparent conductive oxide*, poster presentation at EUPVSEC-29, 22-26 September 2014, Amsterdam, the Netherlands

D. Deligiannis, R. Vasudevan, M. Fischer, A. H. M. Smets, R. A. C. M. M. van Swaaij, M. Zeman, *On the surface passivation of c-Si using high pressure hydrogen diluted plasmas*, oral presentation at MRS 2015 Spring meeting and Exhibit, 6-10 April 2015, San Francisco, California, USA

R. Vasudevan, Z. Thanawala, T. Buijs, **D. Deligiannis**, B. Dam, M. Zeman, I. A. Digdaya, L. Han, P. Perez-Rodriguez, W. A. Smith, A. H. M. Smets, *Hybrid PEC-PV photocathode for water splitting based on silicon wafer heterojunctions and TF Si junctions*, oral presentation at MRS 2015 Spring meeting and Exhibit, 6-10 April 2015, San Francisco, California, USA

P. Calta, G. Yang, **D. Deligiannis**, O. Isabella, P. Šutta, M. Zeman, *Thermally evaporated MoO$_3$ thin films: Structural and optical properties and application in solar cells*, oral presentation at ICANS26, 13-18 September 2015, Aachen, Germany

R. Vasudevan, I. Poli, **D. Deligiannis**, M. Zeman, A. H. M. Smets, *Overview of the metastable properties of the a-Si:H/c-Si interface*, oral presentation at IEEE 43rd PVSC, 5-10 June, Portland, Oregon, USA

Acknowledgments

Completing this work would not have been possible without the support and contribution of many people. I would like to start by thanking my promotor Prof. dr. Miro Zeman for giving me the opportunity to work in the Photovoltaic Materials and Devices (PVMD) research group and for always providing the means necessary to conduct this research. I am also grateful to my co-promotor, Dr. René van Swaaij for his daily support and guidance throughout this project. Thank your for your patience, your scientific approach and for always paying attention to the details when reading, discussing and correcting my work.

Additionally, I would like to thank Prof. dr. Arthur Weeber, Prof. dr. I. M. Richardson, Prof. dr. ir. M. C. M. van de Sanden, Dr. M. Creatore and Dr. K. Ding for participating in my doctoral committee and for reading and giving comments on my thesis, improving this work.

Moreover, I would like to thank Spyridon Alivizatos, Georgios Papakonstantinou, Vasileios Marioleas and Jeroen van Vliet for their efforts and significant contribution in this work through their MSc projects. It was truly a pleasure working with you all. I would also like to express my appreciation to Angeliki Vlassi, although we worked together for a smaller project, the results obtained were an important input for this thesis.

None of the reported experiments would have been possible without the technical assistance of Stefaan Heirman, Jan Chris Staalenburg, Martijn Tijssen and Remko Koornneef. Thank you all for keeping everything running.

I would like to express my deep gratitude to Dr. Rudi Santbergen. Special thanks for the Dutch translation of the Propositions and Summary. Thank you for always finding not just the correct answer to my questions but also the answer that I needed to hear at that moment. It is always a great pleasure to discuss with you, especially over dinner.

During these dinners the company of Dr. Dong Zhang is greatly missed. Dong, thank you for the knowledge you have inherited to the group before moving on with your career. Your work was truly valuable for this thesis.

My oldest and longest officemates, Dr. Ravi Vasudevan and Dr. Hairen Tan. Ravi, your scientific contribution was immensely important to this work. Moreover, I want to thank you for your friendship, for going though all our frustrations together and for always being a good listener. Hairen, your dedication to science and your work attitude has always been inspi-

rational. Thank you for all the enjoyable moments.

Special thanks go to Prof. dr. Arno Smets. After these years I cannot imagine the group without you. Thank you for all the discussions, scientific or not and for bringing so much positivity. I would also like to thank Dr. Olindo Isabella for all the conversations we had throughout these years and for being a relentless tennis opponent.

Furthermore, I would like to thank my PVMD colleagues for the fun and the discussions we had, including Dr. Pavel Babal, Klaas Bakker, Johan Blanker, Marinus Fischer, Yuan Gao, Dr. Lihao Han, Dr. Andrea Ingenito, Dr. Karol Jarolimek, Dr. Do Yun Kim, Gianluca Limodio, Juan Camilo Ortiz Lizcano, Dr. Paul Procel Moya, Dr. Engin Özkol, Nasim Rezaei, Paula Perez Rodriguez, Dr. Martijn van Sebille, Fai Tong Si, Dr. Serge Solntsev, Dr. Mirjam Theelen, Yilei Tian, Robin Vismara, Thierry de Vrijer, Dr. Guangtao Yang, Joke Westra, Mark Workum and Dr. Hesan Ziar. Additionally, special thanks to Dr. Klaus Jäger for sharing his LateX template and to Dr. Jimmy Melskens and Marc Schouten for their help with Fourier-transform infrared spectroscopy measurements.

I would also like to thank Laura Bruns, Claudia de Kooter, Sharmila Rattansingh, Ellen Schwenke-Karlas, Diane Vedder and Ilona van der Wenden for their support in the administrative aspects of this PhD project.

Moreover, I would like to thank everyone involved in the FLASH perspective program, especially Dr. Bart Macco for all the fun discussions we had and the enjoyable collaboration.

Outside the PVMD group I would like to thank Dr. Koen Buisman for our collaboration during the first year of my project and Peter Swart for the technical support during that time. An extended part of the experimental work presented in this thesis took place in the Else Kooi Laboratory and in the Kavli nanolab, the help of all the people working there, including Johan van der Cingel, Silvana Milosavljevic, Hozanna Miro, Dr. Bruno Morana, Dr. Gregory Pandraud and Cassan Visser, is appreciated. Moreover, I am thankful to Ruben Abellón for the help he provided with measurements that took place in the Opto-electronic Materials laboratory.

Additionally, I would like to thank those who did contribute, but I forgot to mention. Thank you and please forgive me.

I would like to thank my parents, Sotiris and Alexandra for their unconditional and never ending love and support.

Finally, I would like to thank Marilena for her support, for reading and giving feedback on this work and for having me talking for hours about things I do not understand myself. Thank you for your patience and love.

Curriculum Vitae

Dimitrios Deligiannis was born in Athens, Greece in 1983. He obtained his BSc in Physics from the University of Crete in 2008. Following a year of employment, he started his MSc degree in Sustainable Energy Technologies at the Delft University of Technology. He graduated in 2011 following the completion of his MSc thesis in the Optoelectronics Materials research group. His MSc research project focused on the analysis of the frequency and time-dependent complex photoconductivity using the Time-Resolved Microwave Conductivity Technique to investigate titanium dioxide films.

In 2012, Dimitrios joined the Photovoltaic Materials and Devices research group at the Delft University of Technology and shifted his research focus to silicon heterojunction solar cells. He presented his work at several international conferences including SiliconPV, EUPVSEC and MRS Spring Meeting and Exhibit. In 2013 his work presented at EUPVSEC received the best poster award in the area of Wafer-Based Silicon Solar Cells and Materials Technology. His work has been published in Energy Procedia, AIP Advances and Journal of Applied Physics.